Recovery of Terrestrial Water Storage Change from Low-Low Satellite-to-Satellite Tracking

by

Yiqun Chen

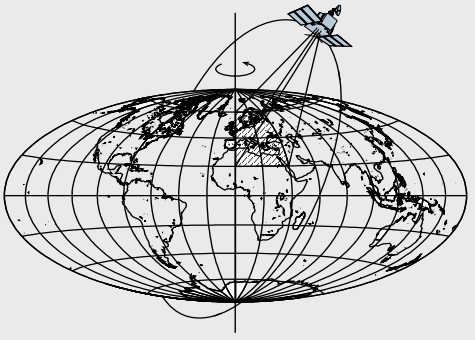

Report No. 485

Geodetic Science and Surveying

The Ohio State University
Columbus, Ohio 43210

December 2007

Recovery of Terrestrial Water Storage Change from Low-Low Satellite-to-Satellite Tracking

by

Yiqun Chen

Report No.485

Geodetic Science and Surveying

The Ohio State University

December 2007

ABSTRACT

Gravity Recovery and Climate Experiment (GRACE) spaceborne gravimetry provides a unique opportunity for quantifying geophysical signals including terrestrial water storage change for a wide variety of climate change and geophysical studies. The contemporary methodology to process GRACE data for temporal gravity field solutions is based on monthly estimates of the mean geopotential field with a spatial resolution longer than 600 km (the Level-2 or L2 data products), after appropriate Gaussian smoothing to remove high-frequency and geographically-correlated errors. Alternative methods include the direct processing of the GRACE low-low satellite-to-satellite tracking data over a region of interest, leading to improved or finer spatial and temporal resolutions of the resulting local gravity signals. The GRACE Level 1B data have been analyzed and processed to recover continental water storage in a regional solution, by first estimating *in situ* Line-Of-Sight (LOS) gravity differences simultaneously with the relative position and velocity vectors of the twin GRACE satellites. This new approach has been validated using a simulation study over the Amazon basin (with three different regularization methods to stabilize the downward continuation solutions), and it is demonstrated that the method achieves an improved spatial resolution as compared to some of the other GRACE processing techniques, including global spherical harmonic solutions, and regional solutions using *in situ* geopotential differences.

PREFACE

This report was prepared for and submitted to the Graduate School of the Ohio State University as a dissertation in partial fulfillment of the requirements of the Ph.D. degree.

The research is supported by grants from NSF's Collaboration in Mathematical Geociences Program (EAR0327633), NASA Earth Science programs (NNG04GN19G, NNG05GL26G, JPL 1265252), and a Shell Fellowship (July-Sept., 2007), School of Earth Sciences, The Ohio State University. Additional computing resources are provided by the Ohio Supercomputer Center.

ACKNOWLEDGMENTS

I wish to thank my advisor, Dr. Burkhard Schaffrin, for his professional supervision, encouragement, beneficial discussions and constructive suggestions which made this dissertation possible, and for his patience in editing the draft. I thank my co-advisor, Dr. C.K. Shum, for introducing me to satellite gravimetry, for his constructive comments throughout my study at OSU, and his continuous support for me as a graduate research associate for over five years. My sincere thanks go to Dr. Doug Alsdorf, who helped me to learn hydrology towards interpreting my results and supported me during the final year of my study. I would like to thank Dr. S.-C. Han for his generous help, particularly for providing me with some of his GRACE data processing software system. I also wish to thank all the other professors and staff in the Geodetic Science and Surveying program, from whom I have learned a lot through their courses and their help. Last but not least, I particularly enjoyed my many fruitful discussions with C.Y. Kuo, Shengjie Ge, Kai-chien Cheng, and all the other fellow students in our program.

TABLE OF CONTENTS

Appendices:

CHAPTER 1

INTRODUCTION

1.1. Time-variable gravity field and mass transport in the Earth system

The total gravity field of the Earth can be separated into two components, one is the static component and the other one is the time-varying component. The static component still changes, but at such a long time interval (from thousands to millions of years or longer) that we can assume it to be steady. Tides on Earth generated by gravitational force from the Sun and the Moon are amongst the temporal gravity signals. The non-tide time-varying component of the terrestrial gravity field is largely affected by contributions of hydrological, oceanic, cryospheric and atmospheric origin, and it is well known that these effects generate measurable signals associated with temporal scales from minutes to secular time scales. The temporal component of the gravity field can be used to study a wide variety of disciplinary and interdisciplinary problems, from monitoring changes in water and snow storage on continents, to determining pressure change at the seafloor, to measuring the redistribution of ice and snow on the polar ice sheets, to constraining postglacial rebound deformation within the solid Earth [Wahr et al., 1998]. In essence the knowledge of temporal component of the global gravity field can help one answer the fundamental question how much mass is being transported and redistributed within the Earth system.

In the past, mass distribution and transport in the Earth system were difficult to be observed directly, which led to an incorrect or incomplete interpretation for some processes and their dynamics in the Earth system. This situation has changed dramatically through the dedicated satellite gravity missions, such as CHAllenging Minisatellite Payload (CHAMP), Gravity Recovery And Climate Experiment (GRACE) and future Gravity field and steady-state Ocean Circulation Explorer (GOCE), with a resolution from global down to a few hundred kilometers.

Advances in the measurement of the gravity have with modern free-fall methods reached accuracies of 10^{-9} *g* (~1 μ*Gal* or 10 *nm/s*^{2}), allowing the measurement of the effect of mass changes within the Earth interior or the geophysical fluids to the commensurate accuracy, and surface height change measurements to ~3 mm relative to the Earth center of mass [Forsberg et al., 2005]. During the decade of the Geopotential, satellite missions

already in operation (CHAMP [Reigber et al., 1996] and GRACE [Tapley et al., 2004a] gravimetry), or to be launched (GOCE gradiometry [ESA, 1999]), will provide an opportunity towards quantifying geophysical signals for a wide variety of climate change and geophysical studies.

The German satellite CHAMP, launched in July 2000 by the GFZ, provides the first data set with high-low satellite-to-satellite tracking and accelerometer measurements for gravity field studies. Its payload includes geodetic-quality GPS receivers (Blackjack-class, 16-channel, dual-frequency) with multiple antennas for precise orbit determination and atmospheric limb-sounding, and a 3-axis Space Triaxial Accelerometer for Research (STAR) accelerometer ($\pm 3\times10^{-9} m/s^2$ and $\pm 3\times10^{-8} m/s^2$ precision in the along track or cross track, and radial directions, respectively), intended to measure non-conservative forces including atmospheric drag. These characteristics led to a break-through in the determination of the long-wavelength gravitational field shortly after CHAMP launch [Reigber et al., 2002].

GRACE was launched in March 2002 for a mission span of 5 years or longer [Tapley et al., 2004a] and is currently operational. The satellite mission consists of two identical co-orbiting spacecrafts with a separation of 220±50 km at a mean initial orbital altitude of 500 km with a near-circular orbit and a mean inclination of 89° for near-global coverage [Bettadpur et al., 2000]. The dual one-way K- (24.5 GHz) and Ka- (32.7 GHz) band microwave inter-satellite ranging system with a precision of ± 0.1 μm/sec in range-rate, the Ultra-Stable Oscillator (USO) accurate to within 70 picosecs of time-tagging, the 3-axis super-STAR accelerometers with a precision of $\pm 4\text{x}10^{-12}$ m/s^2 and the dual-frequency 24-channel Blackjack GPS receivers comprise the instrument suite for GRACE's mapping of the global mean and temporal gravity field [Davis et al., 1999; Kim et al., 2001].

The GOCE space gravity gradiometer (SGG) mission, scheduled to launch in spring 2008, is anticipated to determine the mean Earth gravity field with an unprecedented geoid accuracy of several cm rms error with a wavelength of 130 km or longer [ESA, 1999]. GOCE will operate for about 2 years in a sun-synchronous (98.5° inclination) near-polar orbit and at an altitude of 250 km. The GOCE onboard SGG will measure primarily 4 components (3 diagonals and 1 off-diagonal) of the gradient tensor, and will use the onboard GPS high-low tracking to determine the long-wavelength gravity field as well as register the gravity tensor observables within a few cm of accuracy [Schrama, 2003].

The three satellite gravity missions, CHAMP, GRACE and GOCE, complement each other. CHAMP, is the first low Earth orbiter contributing to a new generation of gravity field model; GRACE is achieving high accuracy for the long and medium wavelength and, for the first time, is able to provide temporal gravity field estimates every 30 days; GOCE will provide higher spatial resolution for the static gravity field.

1.2. Contemporary Results from GRACE

1.2.1. Science Results

Studies have demonstrated that GRACE, so far, provided a factor of 100 improvement in the Earth's mean gravity field [Tapley et al., 2004a], which enabled on improved confirmation of the Lens-Thirring effect using SLR to the Lageos-1/-2 satellites [Ciufolini & Pavlis, 2004], and allowed the first discovery of an asteroid-induced Permian-Triassic crater under the Antarctica ice sheets. A concise and incomplete list of various scientific results using GRACE includes the estimation of recent rapid Greenland ice melt, contributing significantly to sea level rise [Ramillien et al., 2006; Chen et al., 2006b; Luthcke et al., 2006; Velicogna & Wahr, 2006b], Antarctic mass balance [Velicogna & Wahr, 2006a; Ramillien et al., 2006; Chen et al., 2006e], Alaskan glacier melt [Chen et al., 2006d]; major river basin hydrologic fluxes [Wahr et al., 2004; Davis et al., 2004; Han et al., 2005b; Rodell et al., 2007; Seo et al., 2006; Schmidt et al., 2006]; observed ocean tides underneath Antarctic ice shelve [Shum et al., 2005a; Han et al., 2005c] and improved tidal modeling [Ray et al., 2006]; ocean bottom pressure variabilities in the tropical Pacific [Song & Zlotnicki, 2004], Antarctic Circumpolar Current transport variability [Zlotnicki et al., 2006], and global ocean mass variability [Chambers et al., 2004; Chambers 2006a, 2006b]; global mass variations [Wu et al., 2006; Kusche & Schrama, 2005; Shum et al., 2005b]; Global Isostatic Adjustment (GIA) studies [Peltier, 2004; Ivins et al., 2005, Ivins & James, 2005; Schotman et al., 2005, 2006; Paulson, 2006]; and the first observed crustal dilatation (expansion/compression of the crust and mantle) caused by the Sumatra-Andaman undersea earthquake [Han et al., 2006c, 2006d; Shum et al., 2006a].

It anticipates that the GRACE observations, with continuous improvement in data processing, will provide a long (>5 years) time series that makes it possible to produce unprecedented geophysical data set to improve our understanding in global mass fluxes related to terrestrial water storage change.

1.2.2. Improved GRACE modeling and analysis

Numerous processing methods of the GRACE data have led to substantial improvement of the Level -0, Level -1A/B, and the Level-2 (monthly spherical harmonics geopotential solutions to degree 120, to be extended to degree 160) data products by the GRACE Project scientists at CSR, JPL, GFZ, GRGS, APL and by members of the GRACE Science Team. A partial list of notable improvements include sensor (KBR, USO, accelerometer) calibration/filtering [Kim, 2005; Biancale et al., 2005], Level-1 processing and orbit determination including GPS clock/antenna pattern accuracy improvements [Kruizinga et al., 2005; Kang et al., 2005; Yuan and Watkins, 2005], processing and evaluation of new releases of gravity field products [Bettadpur et al., 2005; Schmidt et al., 2005abc; Yuan et al., 2004; Watkins et al., 2005; Luthcke et al., 2005; Schrama & Visser, 2006], direct processing of KBR rate data as *in situ* disturbance potential measurements and using the energy approach [Jekeli, 1999; Han, 2003b; Han et al., 2006b], processing of KBR rate-rate data as *in situ* line-of-sight acceleration measurements [Jekeli, 1999; Chen et al., 2004, 2006], or using Fredholm's integral for

gravity measurements [Mayer-Gürr et al., 2006], treatment of geocenter variations [Chambers et al., 2004], improved ocean tide modeling [Bettadpur et al., 2005; Desai & Yuan, 2006], pole tides [Desai et al., 2006], long period tides and S_1 tides [Egbert & Ray, 2002; Ray & Egbert, 2004], and improved atmosphere and tide de-aliasing products with analysis [Swenson & Wahr, 2002; Ali & Zlotnicki, 2003; Thompson et al., 2004; Han et al., 2004; Flechtner et al., 2005ab].

1.2.3. GRACE regional solutions

Alternate solution techniques [Rowlands et al., 2005; Han et al., 2006b] have demonstrated their initial promise to enhance temporal resolution as fine as 5 days [Han et al., 2005b; Schmidt et al., 2006], spatial resolution up to 220 km or longer (half-wavelength, or $4^\circ \times 4^\circ$ equal area blocks) for the mascon solutions [Rowlands et al., 2005; Lemoine et al., 2005;Yuan & Watkins, 2006], as well as for the energy method [Jekeli, 1999; Han, 2003b; Han et al., 2006b] by employing stochastic regional inversion using 2-D FFT [Han et al., 2003a]. These techniques have demonstrated their capability to enhance temporal and spatial resolutions of geophysical signals as compared to spherical harmonic solutions which, at present, exhibit monthly resolutions and longer than 800 km (half-wavelength) resolutions. These studies reported the observation of enhanced hydrologic signals [Rowlands et al., 2005; Yuan & Watkins, 2006; Han et al., 2005a], tides [Ray et al., 2006; Han et al., 2005b], coseismic deformation signals from large undersea subduction earthquake [Han et al., 2006c, 2006d; Shum et al., 2006a, 2006b], and melting of the Greenland ice sheet [Luthcke et al, 2006].

1.3. Problem statement and research methodology

In this study, the time-variable hydrological effect on the gravity field of the Earth is of particular interest; so the main aim is to recover the terrestrial water storage (soil moisture, ground water, snow and ice, lake and river water, as well as vegetative water) from the temporal component of the gravity field of the Earth. Though only data from low-low Satellite-to-Satellite Tracking (SST) such as GRACE data will be used, methods for both the high-low and the low-low SST will be described for completeness.
In this study we first conduct a simulation for the use of *in situ* Line-Of-Sight (LOS) gravity differences based on the GRACE KBR range acceleration, accelerometer, and other data for the potentially improved recovery of terrestrial water storage change in the Amazon basin region. Various regularization methods, which are necessary to stabilize the downward continuation solutions, have been investigated to identify the optimal estimate for the water storage change from the LOS gravity difference estimates over the study region. Results from various regularization methods will be compared, and the time-variable effects of ocean tides and atmosphere on the temporal gravity field recovery will be analyzed. The next step is to precisely estimate *in situ* LOS gravity differences from the real GRACE L1B data simultaneously with the inter-satellite state vectors, and the estimated *in situ* LOS gravity differences will then be used to extract terrestrial water storage change information on the surface of the Earth. The results will be compared to the results from other GRACE processing techniques, including global spherical harmonic solutions and regional solution using *in situ* geopotential differences, in both the space domain and the spatial frequency domain.

Chapter 2 describes the methods to recover the global gravity field of the Earth, using either geopotential differences or LOS gravity difference estimates from the GRACE measurements. A procedure to estimate continental water storage change globally from the spherical harmonic coefficients of a time-variable global gravity field model will be described.

Chapter 3 describes the alternative methods to estimate continental water storage change regionally, using either *in situ* geopotential differences or *in situ* LOS gravity differences. Three regularization techniques will be introduced and tested to solve the ill-posed problem inherent with the downward continuation.

Chapter 4 describes the closed-loop simulations using geopotential differences or LOS gravity differences to recover continental water storage change globally and regionally. Residual errors from different time-variable ocean tides and atmosphere models will be analyzed.

Chapter.5 shows the global and regional solutions of terrestrial water storage change from the real GRACE data processing. Different regional solutions are compared to each other in both the space domain and the spatial frequency domain, and compared to the global solutions from the monthly GRACE gravity models.

Chapter 6 concludes and proposes some future work.

CHAPTER 2

GLOBAL TERRESTRIAL WATER STORAGE CHANGE AND ITS RECOVERY

2.1. Terrestrial water storage change

The exchange of water among the oceans, atmosphere, and ground surface of the Earth constitutes the hydrological cycle. The amount of water involved in the hydrological cycle is only about 0.1% of the total volume of the water storage in the world; but, if we are considering mass redistribution within the Earth and on and above its surface, it is non-negligible. The terrestrial water constitutes only about 6% of the global hydrologic storage as shown in Table 2.1, but the exchange of water including precipitation and evaporation on or under the surface of the continents constitutes almost 36% of the total water cycle as shown in Table 2.2. In other words, although the continents store a far smaller volume of water than the oceans, it is undergoing the same order of mass changes, caused by the water cycle, as that of the oceans.

The gravitational variations observed by GRACE are primarily attributable to the movement of water throughout the hydrological cycle. It is believed that over spatial areas of several hundred thousand square kilometers, measurements of seasonal changes in water mass with a resolution of 10-30 mm in thickness change should be useful for weather forecasting, climate modeling, and soil moisture and aquifer assessments. Measurement of mass changes at this resolution should be possible with GRACE [Dickey et al., 1997]. It has already been shown by simulation that GRACE may be able to recover changes in continental water storage and in seafloor bottom pressure, at resolutions of a few hundred kilometers and larger in space, and a few weeks and longer in time, with accuracies approaching ± 2 mm in water thickness over land, and ± 0.1 mbar or better in seafloor bottom pressure [Wahr et al., 1998]. Rodell and Famiglietti [1999] state that GRACE will likely detect changes in water storage in most of the basins on monthly or longer time steps and that instrument errors, atmospheric modeling errors, and the magnitude of the variations themselves will be the primary controls on the relative accuracy of the GRACE-derived estimates. Rodell and Famiglietti [2001] went on to build upon their results by relying on observations in Illinois (where measurements of all the water storage components are systematically collected and centrally archived) rather than on modeled results, by analyzing groundwater and surface water variations as well as snow and soil water variations, and by using a longer time series. Then, it was concluded that detection is possible if given a 200,000 km^2 or larger area, and changes in

soil moisture typically represent the largest component of terrestrial water storage variations, followed by changes in groundwater plus intermediate zone storage.

	Unit: 10^6 km^3	Percentage
Oceans	268,450	94.2%
Ice&snow	12000	5.7%
Ground water	4500	
Surface&soil water	100	
Atmosphere	3	≈0.001%
Biosphere	0.1	<0.001%
Total	285053.1	

Table 2.1: The global hydrologic storage [Dickey et al., 1997]

	Unit: 10^6 km^3	Percentage
Ocean precipitation	113.7	58.1%
Ocean evaporation	124.0	
Land precipitation	73.5	35.9%
Land evaporation	48.5	
Runoff	25.0	
Runout	<0.2	
Net inland advection	24.0	6%

Table 2.2**:** The global hydrologic cycle [Dickey et al., 1997]

Two years after the GRACE satellites have been launched, Tapley et al. [2004b] stated that the GRACE mission can provide a geoid height accuracy of ± 2 to ± 3 millimeters at a spatial resolution as small as 400 kilometers. They explained that geoid variations observed over South America, which can be largely attributed to surface water and groundwater changes, show a clear separation between the large Amazon watershed and the smaller watershed to the north. Such observations will help hydrologists to connect processes at traditional spatial resolutions (tens of kilometers or less) with those of regional and global resolutions. Han et al. [2005a,b] adopted an alternative method using GRACE satellite-to-satellite tracking and accelerometer data to obtain the along-track geopotential differences and directly estimate the terrestrial water storage at monthly and sub-monthly resolution. This method was tested on the estimation of a hydrological mass

anomaly over the Amazon and Orinoco river basins; and, by comparing it to conventional spherical harmonic methods, the spatial extent of the estimated GRACE water thickness change achieved finer resolution and is shown to follow more closely the boundaries of the river basins so that significant systematic variation could be discerned at 15-days temporal resolutions.

All the above achievements mean that, by combining measurements from GRACE with measurements taken on the ground, scientists will be able to improve their models of water exchange between the ocean and land surfaces - through rainfall, deep soil moisture, and runoff. This can be done from continental size down to a regional extension of a few hundred kilometers. Because GRACE is sensitive to the integral mass of the Earth, so it is difficult to separate the terrestrial water storage from all the other static masses. However, we can estimate the terrestrial water storage change by simply taking differences of the GRACE measurements in the time domain, since it is easier to model and correct all the other temporal geophysical effects. Also, the estimates are integral of all the water, which means that it cannot distinguish soil moisture from snow, ice, or ground water.

Here, I have developed a new approach to recover the terrestrial water storage change over any part of the world, using Line-Of-Sight (LOS) gravity differences from GRACE data, and I also include in this chapter the derivation of global recovery of the terrestrial water storage change using geopotential differences, for comparison and completeness. Whatever approaches to recover terrestrial water storage change can be applied to recovery of any other mass change such as caused by earthquake or postglacial rebound, as long as all the corresponding effects have been modeled and corrected.

2.2. Recovery of the global gravity field using the energy balance approach

The energy balance approach is based on the law of energy conservation. In physics, the conservation of energy states that the total amount of energy in an isolated system remains constant, although it may change forms, e.g. friction turns kinetic energy into thermal energy. In case of a satellite system, kinetic energy is related to the motion of the satellite (velocity), and the potential energy is related to the mass distribution of the Earth and the distance between the satellite and the Earth. The approach has been considered for gravity field recovery for a long time, certainly since the beginning of the satellite era [O'Keefe, 1957]. Its main advantage is its simplicity; i.e., the potential energy can be linearly related to the unknowns if the gravity field of the Earth is represented by a global spherical harmonics expansion; whereas, in the classical procedure, the recovery of the global gravity field of the Earth is coupled with orbit determination, and iterations are necessary. However, its main disadvantage is that it is more susceptive to orbit error; and in case of the reference gravity field is far from the truth, the results could be off.

According to Newton's Second Law of Motion, in the inertial frame, the kinematic acceleration, $\ddot{\mathbf{r}}^i$, of an object with the mass m is a consequence of a combination of the

conservative force $\mathbf{F}_{conservative}$ and the non-conservative force $\mathbf{F}_{non-conservative}$ acting on the object

$$\ddot{\mathbf{r}}^i = \frac{\mathbf{F}_{conservative} + \mathbf{F}_{non-conservative}}{m} = \mathbf{g}^i + \mathbf{f}^i, \tag{2.1}$$

where $\mathbf{g}^i$ is the gravitational acceleration vector due to $\mathbf{F}_{conservative}$ (mainly from the Earth), $\mathbf{f}^i$ is the non-conservative acceleration vector due to $\mathbf{F}_{non-conservative}$ acting on the satellite, such as atmospheric drag, solar radiation pressure and thermal forces, and the superscript i indicates that the quantity refers to the inertial frame. Both the energy integral and the acceleration approaches for the recovery of the global gravity field start from the same formula, i.e., equation (2.1).

2.2.1. Energy integral for a high-low SST mission (CHAMP)

The gravitational potential, V, in terms of satellite velocity, $\dot{\mathbf{r}}^i = (\dot{x} \quad \dot{y} \quad \dot{z})$, and non-conservative acceleration $\mathbf{f}^i$, can be derived directly [Han, 2003b],

$$V(\mathbf{r}^i(t),t) = \frac{1}{2}\left|\dot{\mathbf{r}}^i\right|^2 - \int_{t_0}^{t} \dot{\mathbf{r}}^i \cdot \mathbf{f}^i dt + \int_{t_0}^{t} \frac{\partial V(\mathbf{r}^i(t),t)}{\partial t} dt - C, \tag{2.2}$$

where V is a function of the position vector $\mathbf{r}^i = (x \quad y \quad z)$ and time t. The first term on the right hand side is the kinetic energy and the second term represents energy dissipation. The third term is due to the explicit time variation of the gravitational potential in inertial space, and C is the energy constant of the system.

Equation (2.2) is derived by first multiplying equation (2.1) with the velocity $\dot{\mathbf{r}}^i$,

$$\dot{\mathbf{r}}^i \cdot \ddot{\mathbf{r}}^i = \dot{\mathbf{r}}^i \cdot \mathbf{g}^i + \dot{\mathbf{r}}^i \cdot \mathbf{f}^i. \tag{2.3}$$

Then substitute the gravitational acceleration by the gradient of the corresponding potential,

$$\mathbf{g}^i(\mathbf{r}^i(t),t) = \nabla_{\mathbf{r}^i} V(\mathbf{r}^i(t),t) = \frac{\partial V(\mathbf{r}^i(t),t)}{\partial \mathbf{r}^i}. \tag{2.4}$$

Since V is a function of the position vector $\mathbf{r}^i$ and time t, so

$$\frac{dV(\mathbf{r}^i(t),t)}{dt} = \frac{\partial V(\mathbf{r}^i(t),t)}{\partial \mathbf{r}^i}\frac{d\mathbf{r}^i(t)}{dt} + \frac{\partial V(\mathbf{r}^i(t),t)}{\partial t}. \tag{2.5}$$

After substituting (2.4) and (2.5) into (2.3), and considering $\dot{\mathbf{r}}^i \cdot \ddot{\mathbf{r}}^i = \frac{d}{dt}\left(\frac{1}{2}\left|\dot{\mathbf{r}}^i\right|^2\right)$, we get

$$\frac{d}{dt}\left(\frac{1}{2}\left|\dot{\mathbf{r}}^i\right|^2\right) = \frac{dV(\mathbf{r}^i(t),t)}{dt} - \frac{\partial V(\mathbf{r}^i(t),t)}{\partial t} + \dot{\mathbf{r}}^i \cdot \mathbf{f}^i. \tag{2.6}$$

The last step is to integrate (2.6) with respect to the time, t, and (2.2) will be obtained. One further step is to assume that the rotation rate of the Earth is a constant and after several simplifications [Jekeli, 1999], we arrive at

$$V = \frac{1}{2}|\dot{\mathbf{r}}|^2 - \int_{t_0}^{t} \dot{\mathbf{r}} \cdot \mathbf{f} dt - \omega_e (x\dot{y} - y\dot{x}) - C, \tag{2.7}$$

where the superscript i has been dropped; ω_e is the mean rotation rate of the Earth.

Jekeli [1999] derived the same formula using an alternative approach which is essentially based on Newton's second law of motion, too. The integral equation (2.2) can also be re-formulated in a rotating frame, such as the Earth-Centered Earth-Fixed frame (ECEF). In this case, because an earth-orbiting satellite is moving in the ECEF frame which itself is also rotating, two additional terms, i.e., centrifugal and Coriolis accelerations, are necessary to be considered. Visser et. al. [2003] and Han [2003b] have both given the derivation in detail. The integral equation in the ECEF frame is,

$$V(\mathbf{r}^e(t), t) = \frac{1}{2}|\dot{\mathbf{r}}^e|^2 - \int_{t_0}^{t} \dot{\mathbf{r}}^e \cdot \mathbf{f}^e dt - \frac{1}{2}(\omega_{ie}^e \times \mathbf{r}^e)^2 - C, \tag{2.8}$$

where $\mathbf{r}^e$ and $\dot{\mathbf{r}}^e$ are the position vector and velocity vector in the ECEF frame, $\mathbf{f}^e$ is the non-conservative acceleration but expressed in the rotating ECEF frame, ω_{ie}^e is the angular velocity of the rotating ECEF frame with respect to the inertial frame and coordinated in the ECEF frame. If we neglect the change of the rotation of the Earth, then,

$$V(\mathbf{r}^e(t), t) = \frac{1}{2}|\dot{\mathbf{r}}^e|^2 - \int_{t_0}^{t} \dot{\mathbf{r}}^e \cdot \mathbf{f}^e dt - \frac{1}{2}\omega_e^2 \left((x^e)^2 + (y^e)^2 \right) - C. \tag{2.9}$$

For the recovery of the global gravity field, the integral equations in both the inertial frame and the ECEF frame have been investigated, and they all achieved comparable results in the case of CHAMP.

2.2.2. Energy integral for a low-low SST mission (GRACE)

Low-low SST constitutes the precise measurement of the range between the twin satellites following each other in approximately the same orbit. The measured ranges, which are biased because microwave is used, are numerically differentiated to obtain range rate and range acceleration. To exploit these highly precise new observations such as range rate, we shall develop an equation to connect the range rate to the potential difference between the positions of the two satellites along the orbit. The computed potential differences will thus be used as boundary values on their corresponding boundaries, the orbits, to estimate the global spherical harmonic coefficients of the gravity field.

It appears that for the satellite 1 and satellite 2, we have, respectively,

$$V_1 = \frac{1}{2}|\dot{\mathbf{r}}_1|^2 - \int_{t_0}^{t} \dot{\mathbf{r}}_1 \cdot \mathbf{f}_1 dt - \omega_e (x_1\dot{y}_1 - y_1\dot{x}_1) - C_1, \tag{2.10}$$

$$V_2 = \frac{1}{2}|\dot{\mathbf{r}}_2|^2 - \int_{t_0}^{t} \dot{\mathbf{r}}_2 \cdot \mathbf{f}_2 dt - \omega_e (x_2\dot{y}_2 - y_2\dot{x}_2) - C_2, \tag{2.11}$$

where the subscripts 1 and 2 stand for the satellite number. After taking the difference between (2.10) and (2.11), we have,

$$V_2 - V_1 = \dot{\mathbf{r}}_1^T \dot{\mathbf{r}}_{12} + \frac{1}{2}\left|\dot{\mathbf{r}}_{12}\right|^2 - \int_{t_0}^{t} (\dot{\mathbf{r}}_2 \cdot \mathbf{f}_2 - \dot{\mathbf{r}}_1 \cdot \mathbf{f}_1)dt - \omega_e (x_{12}\dot{y}_2 - \dot{y}_2 \dot{x}_{12} + x_1 \dot{y}_{12} - y_{12}\dot{x}_1) - C_{12} . \tag{2.12}$$

(2.12) relates the *in situ* inter-satellite range rate measurements to the gravitational potential differences between two satellites. If we divide the total gravitational potential into a normal gravitational potential and a disturbing gravitational potential, T_{12}, (2.12) can be modified to

$$T_{12} = \left|\dot{\mathbf{r}}_1^0\right| \delta\dot{\rho}_{12} + v_1 + v_2 + v_3 + v_4 + \delta VR_{12} - \int (\dot{\mathbf{r}}_2 \cdot \mathbf{f}_2 - \dot{\mathbf{r}}_1 \cdot \mathbf{f}_1)dt - \delta C_{12} , \tag{2.13}$$

where

$v_1 = \left(\dot{\mathbf{r}}_2^0 - \left|\dot{\mathbf{r}}_1^0\right| \mathbf{e}_{12}^0\right) \cdot \delta\dot{\mathbf{r}}_{12}$,

$v_2 = \delta\dot{\mathbf{r}}_1 \cdot \dot{\mathbf{r}}_{12}^0 - \left|\dot{\mathbf{r}}_1^0\right| \delta\mathbf{e}_{12} \cdot \dot{\mathbf{r}}_{12}$,

$v_3 = \delta\dot{\mathbf{r}}_1 \cdot \delta\dot{\mathbf{r}}_{12}$,

$v_4 = \frac{1}{2}\left|\delta\dot{\mathbf{r}}_{12}\right|^2$,

$\delta VR_{12} = \omega_e \left\{ \left(\mathbf{r}_1 \dot{\mathbf{r}}_2 - \mathbf{r}_2 \dot{\mathbf{r}}_1\right)\right|_2 - \left(\mathbf{r}_1 \dot{\mathbf{r}}_2 - \mathbf{r}_2 \dot{\mathbf{r}}_1\right)\Big|_1 - \left(\mathbf{r}_1^0 \dot{\mathbf{r}}_2^0 - \mathbf{r}_2^0 \dot{\mathbf{r}}_1^0\right)\Big|_2 + \left(\mathbf{r}_1^0 \dot{\mathbf{r}}_2^0 - \mathbf{r}_2^0 \dot{\mathbf{r}}_1^0\right)\Big|_1 \right\}$;

the superscript 0 denotes a quantity based on a known reference field, the symbol, δ, indicates an incremental quantity between the true field and the reference field. Equation (2.13) has corrected errors in equation (4.5) of Han [2003b].

2.2.3. Global recovery of the gravity field of the Earth by least-squares adjustment

The geopotential can be represented in terms of spherical harmonic coefficients (solution of Laplace's equation) is:

$$V(r,\theta,\lambda) = \frac{GM}{R} \sum_{n=0}^{\infty} \sum_{m=0}^{n} \left(\frac{R}{r}\right)^{n+1} \overline{P}_{nm}(\cos\theta)\left(\overline{C}_{nm} \cos m\lambda + \overline{S}_{nm} \sin m\lambda\right), \tag{2.14}$$

where GM is the gravitational constant times the mass of the Earth, R is the mean radius of the Earth, (r,θ,λ) are the spherical coordinates of the calculation point, $\overline{P}_{nm}$ are the normalized Legendre functions, and $\overline{C}_{nm}$ and $\overline{S}_{nm}$ are the normalized dimensionless spherical harmonic coefficients of degree n and order m.

In geodesy it is common to split a quantity into a normal part and a disturbing part. By introducing a (known) reference model U, like Geodetic Reference System (GRS) 80, for instance; the disturbing potential T is

$$T(r,\theta,\lambda) = V(r,\theta,\lambda) - U(r,\theta,\lambda) . \tag{2.15}$$

GRS80 is defined using four defining constants; the equatorial mean radius of the Earth, the geocentric gravitational constant of the Earth, the Earth's flattening and the angular

velocity of the Earth. Based on the four parameters, the normal potential U is computed as follows:

$$U(r,\theta,\lambda)=\frac{GM}{R}\sum_{n=0}^{\infty}\left(\frac{R}{r}\right)^{n+1}\overline{P}_{n0}(\cos\theta)\overline{C}_{n0}^{GRS80}\,, \tag{2.16}$$

where $\overline{P}_{n0}$ is the Legendre polynomial of degree n. The normal potential is defined to have rotational symmetry and equatorial symmetry, so that the even zonal coefficients suffice to calculate the normal potential; usually five coefficients (n = 2, 4, 6, 8, 10) are enough to calculate U accurately.

The coefficients for the first degree spherical harmonics, $\overline{C}_{1,0}$, $\overline{C}_{1,1}$ and $\overline{S}_{1,1}$, vanish after setting the origin of the coordinate system at the center of mass of the Earth, which is not changing. After truncation at the maximum degree $N_{\max}$, we yield a spherical harmonics expression for the disturbing potential T,

$$T(r,\theta,\lambda)=\frac{GM}{R}\sum_{n=2}^{N_{\max}}\sum_{m=0}^{n}\left(\frac{R}{r}\right)^{n+1}\overline{P}_{nm}(\cos\theta)\left(\Delta\overline{C}_{nm}\cos m\lambda+\Delta\overline{S}_{nm}\sin m\lambda\right), \tag{2.17}$$

where

$$\Delta\overline{C}_{nm}=\begin{cases}\overline{C}_{nm}-\overline{C}_{n0}^{GRS80}, & m=0,\quad n=2,\ 4,\ 6,\ 8,\ 10\\ \overline{C}_{nm} & \textit{otherwise}\end{cases}$$

and

$\Delta\overline{S}_{nm}=\overline{S}_{nm}$. $\Delta\overline{C}_{nm}$ and $\Delta\overline{S}_{nm}$ are the unknown parameters, to be estimated by a least-squares adjustment.

In the case of high-low SST, the disturbing potential $T(r,\theta,\lambda)$ can be calculated from velocities and positions of the satellite, as well as the measurements of accelerometer and star sensor (provides attitudes of the satellite); so, (2.17) can be used directly. In case of the low-low SST, (2.17) needs to be modified as follows:

$$\begin{aligned}T_{12}(r_1,\theta_1,\lambda_1,r_2,\theta_2,\lambda_2)&=T(r_2,\theta_2,\lambda_2)-T(r_1,\theta_1,\lambda_1)\\&=\frac{GM}{R}\sum_{n=2}^{N_{\max}}\sum_{m=0}^{n}\begin{Bmatrix}\left\{\left(\frac{R}{r_2}\right)^{n+1}\overline{P}_{nm}(\cos\theta_2)\cos m\lambda_2-\left(\frac{R}{r_1}\right)^{n+1}\overline{P}_{nm}(\cos\theta_1)\cos m\lambda_1\right\}\Delta\overline{C}_{nm}+\\ \left\{\left(\frac{R}{r_2}\right)^{n+1}\overline{P}_{nm}(\cos\theta_2)\sin m\lambda_2-\left(\frac{R}{r_1}\right)^{n+1}\overline{P}_{nm}(\cos\theta_1)\sin m\lambda_1\right\}\Delta\overline{S}_{nm}\end{Bmatrix},\end{aligned} \tag{2.18}$$

where, (r_1,θ_1,λ_1) and (r_2,θ_2,λ_2) are the coordinates of the first satellite and the second satellite.

2.3. Recovery of the global gravity field using the gravity acceleration approach

One alternative approach to recover the global gravity field is also based, but more directly, on Newton's equation of motion; it allows to compute the gravity accelerations

along the orbit of the satellite which is the first gradient of the gravity potential. This has been investigated by many researchers, and has led to a number of publications [Reubelt et al., 2003; Ditmar et al., 2004; Mayer-Gürr et al., 2005a]. One issue of the gravity acceleration approach is that the acceleration has to be based on the numerical differential of the GPS-derived orbit. It is well known that numerical differentiation of noisy data is an improperly posed problem, and a proper averaging filter has been investigated to be incorporated into the processing procedure by Ditmar et al., [2004]. In this dissertation, my goal is to use GRACE data for the recovery of a geophysical signal such as continental water storage change, hence, low-low SST (GRACE) will be our focus. The gravity acceleration approach for high-low SST (CHAMP) will just be included for completeness.

2.3.1. Gravity acceleration approach for a high-low SST mission (CHAMP)

In reality a certain number of additional forces act on the near–earth satellite. They can be divided into two groups, conservative and non-conservative forces. The conservative ones are responsible for the accelerations due to other celestial bodies (Sun, Moon, etc.) besides the Earth, and accelerations due to solid Earth and oceanic tides. The conservative forces cannot be sensed by the accelerometer.

The non-conservative forces, on the other hand, cause accelerations due to atmospheric drag, direct solar radiation pressure and Earth-reflected solar radiation pressure [Seeber, 2003]. These forces can be sensed by an accelerometer, so a comprehensive model is as follows,

$$\ddot{\mathbf{r}} = \mathbf{g}^{mean\ \ Earth} + \mathbf{g}^{N\ \ body} + \mathbf{g}^{tides} + \mathbf{g}^{others} + \mathbf{a}\,, \tag{2.19}$$

where $\mathbf{g}^{N\ \ body}$ is the gravitational acceleration due to the Sun, the Moon and other celestial bodies, $\mathbf{g}^{tides}$ is the gravitational acceleration due to various tides including ocean tides, solid Earth tide and pole tides, $\mathbf{g}^{others}$ is due to other time-variable effects such as atmospheric effects and barotropic ocean response to atmoshpere. $\mathbf{a}$ is due to the non-conservative forces and can be measured by the onboard accelerometer. (2.19) can be rearranged as,

$$\mathbf{g}^{mean\ \ Earth} = \ddot{\mathbf{r}} - \mathbf{g}^{N\ \ body} - \mathbf{g}^{tides} - \mathbf{g}^{others} - \mathbf{a}\,. \tag{2.20}$$

Taking the gradient for (2.14), we find

$$\begin{cases} \dfrac{\partial V}{\partial \theta} = -\dfrac{GM}{R}\displaystyle\sum_{n=2}^{N_{\max}}\left(\frac{R}{r}\right)^{n+1}\sum_{m=0}^{n}\left(\overline{C}_{nm}\cos m\lambda + \overline{S}_{nm}\sin m\lambda\right)\overline{P}'_{nm}(\cos\theta)\sin\theta \\ \dfrac{\partial V}{\partial \lambda} = \dfrac{GM}{R}\displaystyle\sum_{n=2}^{N_{\max}}\left(\frac{R}{r}\right)^{n+1}\sum_{m=0}^{n} m\left(-\overline{C}_{nm}\sin m\lambda + \overline{S}_{nm}\cos m\lambda\right)\overline{P}_{nm}(\cos\theta) \\ \dfrac{\partial V}{\partial r} = -\dfrac{GM}{R^2}\displaystyle\sum_{n=2}^{N_{\max}}(n+1)\left(\frac{R}{r}\right)^{n+2}\sum_{m=0}^{n}\left(\overline{C}_{nm}\cos m\lambda + \overline{S}_{nm}\sin m\lambda\right)\overline{P}_{nm}(\cos\theta) \end{cases}, \tag{2.21}$$

To calculate the acceleration at the direction of north-east-down (n-frame), we obtain

$$\mathbf{g}^n = \begin{bmatrix} g_N \\ g_E \\ g_D \end{bmatrix} = \begin{bmatrix} -\frac{1}{r}\frac{\partial V}{\partial \theta} \\ \frac{1}{r\sin\theta}\frac{\partial V}{\partial \lambda} \\ -\frac{\partial V}{\partial r} \end{bmatrix}. \tag{2.22}$$

Then, by transforming the gravity vector from the n-frame to the inertial frame (i-frame, the ideal i-frame is approximated by J2000 frame in the real GRACE data processing),

$$\mathbf{g}^i = \mathbf{C}_n^i \mathbf{g}^n = \mathbf{C}_e^i \mathbf{C}_n^e \mathbf{g}^n, \tag{2.23}$$

$$\mathbf{C}_e^i = \mathbf{PNRW}, \tag{2.24}$$

$$\mathbf{C}_n^e = \mathbf{R}_3(-\lambda)\mathbf{R}_2(\frac{\pi}{2}+\theta) = \begin{pmatrix} -\sin\theta\cos\lambda & -\sin\lambda & -\cos\theta\cos\lambda \\ -\sin\theta\sin\lambda & \cos\lambda & -\cos\theta\sin\lambda \\ \cos\theta & 0 & -\sin\theta \end{pmatrix}, \tag{2.25}$$

where $\mathbf{g}^i$ is the gravity acceleration in the i-frame, and $\mathbf{g}^n$ is the gravity acceleration in the n-frame. $\mathbf{P}$, $\mathbf{N}$, $\mathbf{R}$ and $\mathbf{W}$ are the rotation matrices caused by precession, nutation, earth rotation and polar motion, respectively. $\mathbf{R}_3(-\lambda)$ represents the rotation about the 3rd axis by the angle λ in the clockwise sense as viewed along the axis toward the origin (right-hand rule), $\mathbf{R}_2(\frac{\pi}{2}+\theta)$ represents the rotation about the 2nd axis by the angle $\frac{\pi}{2}+\theta$ in the counterclockwise sense as viewed along the axis toward the origin (right-hand rule). In the real GRACE data processing, the ideal inertial frame is approximated by the J2000 frame.

Equations (2.21) through (2.25) will be used to set up the observation model for the gravity acceleration approach in the case of a high-low SST mission such as CHAMP. Compared to the energy balance approach, we see that the acceleration approach is more "natural" because it comes directly from the Newton equation of motion. An alternative approach for the acceleration approach, which avoids numerical differentiation, was proposed by Mayer-Gürr et al. [2005a]. In the alternative approach, the Newton equation of motion is formulated as a boundary value problem, and its solution comes in the form of a Fredholm type integral equation which then avoids any numerical differentiation. It is claimed that this approach is both useful for regional and global recovery of the gravity field [Mayer-Gürr et al., 2005a].

2.3.2. Gravity acceleration approach for a low-low SST mission (GRACE)

In a low-low SST mission such as GRACE, the inter-satellite signal (K-Band Ranging (KBR) measurements) between a pair of satellites orbiting the Earth in the same orbital plane carries significant information on the medium to shorter wavelength components of the Earth's gravitational field and, if this relative motion can be measured with sufficient

accuracy, this approach will provide significant improvement in the gravity field modeling. KBR range is a biased range; range, range rate and range acceleration all come from the same KBR measurement by the differentials. In this section, I will show how to recover the gravity field from the KBR range acceleration.

Let $\mathbf{r}_1$ and $\mathbf{r}_2$ represent the position vectors of the two satellites in the inertial frame (J2000 frame in practice), and ρ_{12} represent the range between the two satellites. We then have,

$$\rho_{12}^2 = \mathbf{r}_{12} \cdot \mathbf{r}_{12}, \tag{2.26}$$

where $\mathbf{r}_{12} = \mathbf{r}_2 - \mathbf{r}_1$.

After taking the 2nd derivative with respect to time in the inertial frame (cf. Appendix A), we have,

$$\ddot{\rho}_{12} = (\mathbf{g}_2 - \mathbf{g}_1) \cdot \mathbf{e}_{12} + (\mathbf{a}_2 - \mathbf{a}_1) \cdot \mathbf{e}_{12} + \frac{\left|\dot{\mathbf{r}}_{12}\right|^2 - \dot{\rho}_{12}^2}{\rho_{12}}. \tag{2.27}$$

Then, by rearranging items and adding superscript i to indicate the inertial frame, we obtain

$$\mathbf{g}_{12}^i \cdot \mathbf{e}_{12}^i = \ddot{\rho}_{12} - \frac{\left|\dot{\mathbf{r}}_{12}^i\right|^2 - \dot{\rho}_{12}^2}{\rho_{12}} - \mathbf{a}_{12}^i \cdot \mathbf{e}_{12}^i \ . \tag{2.28}$$

and,

$$\begin{aligned} \mathbf{g}_{12}^i &= \mathbf{g}_2^i - \mathbf{g}_1^i \\ &= \mathbf{C}_{n,2}^i \mathbf{g}_2^n - \mathbf{C}_{n,1}^i \mathbf{g}_1^n \\ &= \mathbf{C}_{n,2}^i \cdot \mathbf{g}_2^n - \mathbf{C}_{n,1}^i \cdot \mathbf{g}_1^n, \end{aligned} \tag{2.29}$$

where $\mathbf{C}_{n,2}^i$ is the transformation matrix from the n-frame to the i-frame for the satellite 2, and $\mathbf{C}_{n,1}^i$ is the transformation matrix from the n-frame to the i-frame for the satellite 1. $\mathbf{g}_2^n$ is the gravity vector in the n-frame at the position of satellite 2, and $\mathbf{g}_1^n$ is the gravity vector in the n-frame at the position of satellite 1.
Thus,

$$\begin{aligned} \mathbf{g}_{12}^i \cdot \mathbf{e}_{12}^i &= \mathbf{C}_{n,2}^i \cdot \mathbf{g}_2^n \cdot \mathbf{e}_{12}^i - \mathbf{C}_{n,1}^i \cdot \mathbf{g}_1^n \cdot \mathbf{e}_{12}^i \\ &= (\mathbf{C}_{n,2}^i)^T \cdot \mathbf{e}_{12}^i \cdot \mathbf{g}_2^n - (\mathbf{C}_{n,1}^i)^T \cdot \mathbf{e}_{12}^i \cdot \mathbf{g}_1^n \\ &= (\mathbf{C}_{i,2}^n \cdot \mathbf{e}_{12}^i) \cdot \mathbf{g}_2^n - (\mathbf{C}_{i,1}^n \cdot \mathbf{e}_{12}^i) \cdot \mathbf{g}_1^n. \end{aligned} \tag{2.30}$$

Let us define $\mathbf{b}_{i,2}^n := (\mathbf{C}_{i,2}^n \cdot \mathbf{e}_{12})$ and $\mathbf{b}_{i,1}^n := (\mathbf{C}_{i,1}^n \cdot \mathbf{e}_{12})$; then:

$$\mathbf{g}_{12}^i \cdot \mathbf{e}_{12}^i == \mathbf{b}_{i,2}^n \cdot \mathbf{g}_2^n - \mathbf{b}_{i,1}^n \cdot \mathbf{g}_1^n. \tag{2.31}$$

After expressing the three components of $\mathbf{g}^n$ in terms of the spherical coordinates (r, θ, λ), we obtain

$$\mathbf{g}^n = \begin{bmatrix} g_N \\ g_E \\ g_D \end{bmatrix} = \begin{bmatrix} -\frac{1}{r}\frac{\partial V}{\partial \theta} \\ \frac{1}{r\sin\theta}\frac{\partial V}{\partial \lambda} \\ -\frac{\partial V}{\partial r} \end{bmatrix}$$

$$= \begin{bmatrix} \frac{GM}{R^2}\sum_{n=0}^{N_{\max}}\sum_{m=0}^{n}(\frac{R}{r})^{n+2}(\cos(m\lambda)\overline{C}_{nm} + \sin(m\lambda)\overline{S}_{nm})\overline{P}'_{nm}(\cos\theta)\sin\theta \\ \frac{GM}{R^2}\sum_{n=0}^{N_{\max}}\sum_{m=0}^{n}(\frac{R}{r})^{n+2}m(-\sin(m\lambda)\overline{C}_{nm} + \cos(m\lambda)\overline{S}_{nm})\overline{P}_{nm}(\cos\theta)\frac{1}{\sin\theta} \\ \frac{GM}{R^2}\sum_{n=0}^{N_{\max}}\sum_{m=0}^{n}(n+1)(\frac{R}{r})^{n+2}(\cos(m\lambda)\overline{C}_{nm} + \sin(m\lambda)\overline{S}_{nm})\overline{P}_{nm}(\cos\theta) \end{bmatrix}. \quad (2.32)$$

Defining

$$\mathbf{b}_{i,2}^n = \begin{pmatrix} b_{2,x} \\ b_{2,y} \\ b_{2,z} \end{pmatrix}, \quad (2.33)$$

$$\mathbf{b}_{i,1}^n = \begin{pmatrix} b_{1,x} \\ b_{1,y} \\ b_{1,z} \end{pmatrix}, \quad (2.34)$$

leads us to

$$\mathbf{b}_{i,2}^n \cdot \mathbf{g}_2^n = b_{2,x}(-\frac{1}{r_2}\frac{\partial V}{\partial \theta_2}) + b_{2,y}(\frac{1}{r_2\sin\theta_2}\frac{\partial V}{\partial \lambda_2}) + b_{2,z}(-\frac{\partial V}{\partial r_2}), \quad (2.35)$$

$$\mathbf{b}_{i,1}^n \cdot \mathbf{g}_1^n = b_{1,x}(-\frac{1}{r_1}\frac{\partial V}{\partial \theta_1}) + b_{1,y}(\frac{1}{r_1\sin\theta_1}\frac{\partial V}{\partial \lambda_1}) + b_{1,z}(-\frac{\partial V}{\partial r_1}), \quad (2.36)$$

$$\begin{aligned} \mathbf{b}_{i,2}^n \cdot \mathbf{g}_2^n - \mathbf{b}_{i,1}^n \cdot \mathbf{g}_1^n = {} & b_{2,x}(-\frac{1}{r_2}\frac{\partial V}{\partial \theta_2}) + b_{2,y}(\frac{1}{r_2\sin\theta_2}\frac{\partial V}{\partial \lambda_2}) + b_{2,z}(-\frac{\partial V}{\partial r_2}) - \\ & - b_{1,x}(-\frac{1}{r_1}\frac{\partial V}{\partial \theta_1}) - b_{1,y}(\frac{1}{r_1\sin\theta_1}\frac{\partial V}{\partial \lambda_1}) - b_{1,z}(-\frac{\partial V}{\partial r_1}) \end{aligned}, \quad (2.37)$$

$$\begin{aligned} \mathbf{b}_{i,2}^n \cdot \mathbf{g}_2^n - \mathbf{b}_{i,1}^n \cdot \mathbf{g}_1^n = {} & b_{2,x}(-\frac{1}{r_2}\frac{\partial V}{\partial \theta_2}) - b_{1,x}(-\frac{1}{r_1}\frac{\partial V}{\partial \theta_1}) \\ & + b_{2,y}(\frac{1}{r_2\sin\theta_2}\frac{\partial V}{\partial \lambda_2}) - b_{1,y}(\frac{1}{r_1\sin\theta_1}\frac{\partial V}{\partial \lambda_1}) \\ & + b_{2,z}(-\frac{\partial V}{\partial r_2}) - b_{1,z}(-\frac{\partial V}{\partial r_1}). \end{aligned} \quad (2.38)$$

If we let $g(\theta)=\overline{P}_{nm}(\cos\theta)$, then $g'(\theta)=-\overline{P}'_{nm}(\cos\theta)\sin\theta$. Introducing a reference potential field $U(r,\theta,\lambda)$ for $V(r,\theta,\lambda)$ to calculate $\mathbf{g}_1^{n,0}$ and $\mathbf{g}_2^{n,0}$; so finally (cf. Appendix B for details of the derivation):

$$(\mathbf{b}_{i,2}^n\cdot\mathbf{g}_2^n-\mathbf{b}_{i,1}^n\cdot\mathbf{g}_1^n)-(\mathbf{b}_{i,2}^n\cdot\mathbf{g}_2^{n,0}-\mathbf{b}_{i,1}^n\cdot\mathbf{g}_1^{n,0})=\frac{GM}{R^2}\times$$

$$\sum_{n=0}^{N_{\max}}\sum_{m=0}^{n}\left\{\begin{array}{l}(\frac{R}{r_2})^{n+2}\left[\begin{array}{l}-b_{2,x}\cos(m\lambda_2)g'(\theta_2)-mb_{2,y}\sin(m\lambda_2)g(\theta_2)\frac{1}{\sin\theta_2}+\\ b_{2,z}(n+1)\cos(m\lambda_2)g(\theta_2)\end{array}\right]-\\ (\frac{R}{r_1})^{n+2}\left[\begin{array}{l}-b_{1,x}\cos(m\lambda_1)g'(\theta_1)-mb_{1,y}\sin(m\lambda_1)g(\theta_1)\frac{1}{\sin\theta_1}+\\ b_{1,z}(n+1)\cos(m\lambda_1)g(\theta_1)\end{array}\right]\end{array}\right\}\Delta\overline{C}_{nm}+$$

$$+\left\{\begin{array}{l}(\frac{R}{r_2})^{n+2}\left[\begin{array}{l}-b_{2,x}\sin(m\lambda_2)g'(\theta_2)+mb_{2,y}\cos(m\lambda_2)g(\theta_2)\frac{1}{\sin\theta_2}+\\ b_{2,z}(n+1)\sin(m\lambda_2)g(\theta_2)\end{array}\right]-\\ (\frac{R}{r_1})^{n+2}\left[\begin{array}{l}-b_{1,x}\sin(m\lambda_1)g'(\theta_1)+mb_{1,y}\cos(m\lambda_1)g(\theta_1)\frac{1}{\sin\theta_1}+\\ b_{1,z}(n+1)\sin(m\lambda_1)g(\theta_1)\end{array}\right]\end{array}\right\}\Delta\overline{S}_{nm}.$$

. (2.39)

Formulas (2.31) and (2.39) together give us the observation equations to estimate the spherical harmonics coefficients.

2.4. Recovery of terrestrial water storage change globally

It is well known that the external gravity field, even if completely and exactly known, cannot uniquely determine the density distribution of the body that produces the gravity field. But in the case of a 2-D spherical shell without the radial dependence, the gravitational inversion for the surface density function proves to be unique [Chao, 2005]. This conclusion encourages us to recover surface mass variability from GRACE data, which was first shown to be successful in a simulation scenario by Wahr et al. [1998].

Equation (2.40) below relates the change in surface mass density ($\Delta\sigma(\theta,\phi)$) to changes ΔC_{lm} and ΔS_{lm} in the geopotential coefficients when expressed in spherical surface functions [Wahr et al., 1998]. There it is shown that

$$\Delta\sigma(\theta,\phi)=\frac{R\rho_{ave}}{3}\sum_{l=0}^{\infty}\sum_{m=0}^{l}\overline{P}_{lm}(\cos\theta)\frac{2l+1}{1+k_l}(\Delta C_{lm}\cos(m\phi)+\Delta S_{lm}\sin(m\phi)), \quad (2.40)$$

where R is the mean radius of the Earth, θ and ϕ are colatitude and longitude. ρ_{ave} is the average density of the Earth (=5517 kg/m^3), ρ_w is the density of water which can be

assumed to be 1000 kg/m^3. ΔC_{lm} and ΔS_{lm} are the changes in the geopotential coefficients when expressed in spherical surface functions. k_l is the Love number.

The following equation is used to compute for the change in geoid undulation:

$$\Delta N(\theta,\phi) = \frac{3R\rho_w}{\rho_{ave}} \sum_{l=0}^{\infty} \sum_{m=0}^{l} \overline{P}_{lm}(\cos\theta) \frac{1+k_l}{2l+1} (\Delta \overline{C}_{lm} \cos(m\phi) + \Delta \overline{S}_{lm} \sin(m\phi)), \quad (2.41)$$

where

$$\begin{Bmatrix} \Delta \overline{C}_{lm} \\ \Delta \overline{S}_{lm} \end{Bmatrix} = \frac{1}{4\pi R\rho_w} \int_0^{2\pi} d\phi \int_0^{\pi} \sin\theta d\theta \cdot \Delta\sigma(\theta,\phi) \overline{P}_{lm}(\cos\theta) \begin{Bmatrix} \cos(m\phi) \\ \sin(m\phi) \end{Bmatrix}. \quad (2.42)$$

So, from the knowledge of surface mass change, we can calculate the change in the geoid.

Furthermore, let $\Delta\rho(r,\theta,\phi)$ be the density redistribution causing the geoid to change, and suppose that $\Delta\rho(r,\theta,\phi)$ is concentrated in a thin layer of thickness at the Earth's surface. But this thin layer should be thick enough to include those portions of the atmosphere, oceans, ice caps, below-ground water storage, and solid Earth deformation with significant mass fluctuations. Then $\Delta\sigma(\theta,\phi)$ denotes the radial integral of $\Delta\rho(r,\theta,\phi)$,

$$\Delta\sigma(\theta,\phi) = \int_{thin\ layer} \Delta\rho(r,\theta,\phi) dr. \quad (2.43)$$

Note that $\Delta\sigma/\rho_w$ is the change in surface mass expressed in equivalent water thickness,

$$\Delta h(\theta,\phi) = \frac{\Delta\sigma(\theta,\phi)}{\rho_w} = \frac{R\rho_{ave}}{3\rho_w} \sum_{l=0}^{\infty} \sum_{m=0}^{l} \overline{P}_{lm}(\cos\theta) \frac{2l+1}{1+k_l} (\Delta C_{lm} \cos(m\phi) + \Delta S_{lm} \sin(m\phi)). \quad (2.44)$$

From the above formula, we can calculate terrestrial water storage change from a time series of the global gravity field of the Earth. It should be pointed out that smoothing is needed to mitigate high-frequency errors [Wahr et al., 2004], including geographically-correlated errors (stripes) [Swenson & Wahr, 2006].

CHAPTER 3

RECOVERY OF TERRESTRIAL WATER STORAGE CHANGE REGIONALLY

3.1. Estimating terrestrial water storage change regionally from *in situ* geopotential differences

In Chapter 2 it has been shown how to recover the terrestrial water storage change globally by estimating the time-variable global gravity field. There is an alternative method using GRACE satellite-to-satellite tracking and accelerometer data to get the along-track potential differences and to directly estimate the temporal gravity variations regionally [Han et al., 2005a,b]. The method has been tested on the estimation of a hydrological mass anomaly over the Amazon and Orinoco river basins; it is claimed that finer resolution can be achieved compared to the conventional spherical harmonic methods.

In this alternative method it is necessary to derive the *in situ* (on-orbit) geopotential difference anomalies at first. The formula is given as follows:

$$\dot{\rho}_{12} = \frac{1}{|\dot{\mathbf{r}}_1|}(V_{12} + E_{12}^F) - \frac{1}{|\dot{\mathbf{r}}_1|}\dot{\mathbf{r}}_1 \cdot \dot{\mathbf{r}}_{12} - \frac{1}{2|\dot{\mathbf{r}}_1|}\dot{\mathbf{r}}_{12} \cdot \dot{\mathbf{r}}_{12} + \mathbf{e}_{12} \cdot \dot{\mathbf{r}}_{12} + \frac{1}{|\dot{\mathbf{r}}_1|}E_{12}^R + const. + e\,, \quad (3.1)$$

where $\dot{\rho}_{12}$ is the range-rate measurement between satellites 1 and 2 with the random error e. $\dot{\mathbf{r}}_1$ and $\dot{\mathbf{r}}_{12}$ are the absolute velocity vector of satellite 1 and the inter-satellite velocity vector, respectively, using coordinates in the inertial frame. $\mathbf{e}_{12}$ is the normalized Line-Of-Sight (LOS) position vector. V_{12} is the *in situ* geopotential difference, E_{12}^F is the dissipative energy difference, and E_{12}^R is the energy due to the Earth rotation. After the *in situ* geopotential difference V_{12} is estimated simultaneously with the inter-satellite orbit vectors, and after the relatively well-known effects of N-Body perturbations, solid earth tides, pole tides, ocean tides, atmosphere and barotropic ocean response to atmosphere are forward-modeled based on the best current models, the gravitational potential difference due to hydrology can be calculated by the following equation,

$$V_{12}^{hydrology} = V_{12} - V_{12}^{Earth} - V_{12}^{N-body} - V_{12}^{tides} - V_{12}^{ocean} - V_{12}^{atmosphere} - V_{12}^{others}, \quad (3.2)$$

where V_{12}^{others} denotes the gravitational potential due to other possible mass redistributions including postglacial rebound, earthquake, etc. The next step is to infer the water mass

change from the *in situ* geopotential difference using the regional inversion method based on prior information.

The potential theory states that alternative various sources can reproduce the same potential field. Hereby we can replace the point mass source with the regular prism mass as follows:

$$m(\theta_i, \lambda_i, t) = \rho_w (R\Delta\theta)(R\Delta\lambda \sin\theta_i) h_i(t) . \tag{3.3}$$

Then, let $\Delta h_i(t)$ be the continental water mass change with respect to the estimated continental water mass of the first month. Here we assume that the water storage doesn't change within one month so that we use Δh_i instead of $\Delta h_i(t)$.
Based on Newton's law of gravitation, the relationship between the gravitational point mass source and the potential difference at altitude can be expressed as follows:

$$V_{12}^{hydrology}(r_1, \theta_1, \lambda_1, r_2, \theta_2, \lambda_2; t) = G \sum_{i=1}^{N \times M} m(\theta_i, \lambda_i, t)(\frac{1}{l_1^i} - \frac{1}{l_2^i}), \tag{3.4}$$

where

$l_1^i = \sqrt{R^2 + r_1^2 - 2Rr_1 \cos\psi_1^i}$,

$l_2^i = \sqrt{R^2 + r_2^2 - 2Rr_2 \cos\psi_2^i}$,

$\cos\psi_1^i = \cos\theta_i \cos\theta_1 + \sin\theta_i \sin\theta_1 \cos(\lambda_i - \lambda_1)$,

$\cos\psi_2^i = \cos\theta_i \cos\theta_2 + \sin\theta_i \sin\theta_2 \cos(\lambda_i - \lambda_2)$.

Here, r_1, θ_1 and λ_1 are radius, co-latitude and longitude of satellite 1, and r_2, θ_2 and λ_2 are radius, co-latitude and longitude of satellite 2, respectively. G is the gravitational constant, ρ_w is the density of fresh water ($1000\, kg/m^3$). R is the mean Earth radius, and $(R\Delta\theta)(R\Delta\lambda)\sin\theta_i$ represents a horizontal area of a rectangular prism at the location (θ_i, λ_i). h_i is the mean water thickness per unit area at the location (θ_i, λ_i) and time t. N and M are the numbers of grid intervals in the latitude and longitude direction, respectively; ∇ is the gradient operator.

The final step is to correct the estimated water storage h_i considering the loading effect [Han et al., 2005b]:

$$H_{pq} = \frac{1}{L_\theta L_\lambda} \sum_{k=0}^{N-1} \sum_{l=0}^{M-1} h(\theta_k, \lambda_l) \cdot \exp(-\sqrt{-1}(\frac{2\pi p}{L_\theta}\theta_k + \frac{2\pi q}{L_\lambda}\lambda_l)) , \tag{3.5}$$

$$h(\theta_k, \lambda_l) = \frac{1}{L_\theta L_\lambda} \sum_{p=0}^{N-1} \sum_{q=0}^{M-1} \frac{1}{(1+k_f)} H_{pq} \cdot \exp(\sqrt{-1}(\frac{2\pi p}{L_\theta}\theta_k + \frac{2\pi q}{L_\lambda}\lambda_l)) , \tag{3.6}$$

where $L_\theta = N\Delta\theta$ and $L_\lambda = M\Delta\lambda$. H_{pq} is a 2-D Fourier coefficient at N-S (latitude) frequency, p/L_θ, and E-W (longitude) frequency, q/L_λ. Furthermore, k_f is the load Love number at the mean (isotropic) frequency $f = \sqrt{(p/L_\theta)^2 + (q/L_\lambda)^2}$. I used the relationship of $n = 2\pi Rf$ for the conversion between the spherical harmonics degree, n,

and the planar frequency, f . Note that $h(\theta_k, \lambda_l)$ in (3.5) and (3.6) corresponds to h_i for a particular combination of k and l.

When we are recovering terrestrial water change, it is necessary to remove the effect of the atmosphere. It was concluded that analyzed pressure fields (atmosphere) will be adequate to remove the atmospheric contribution from GRACE hydrological estimates to subcentimeter level, [Velicogna and Wahr, 2001]. It should be noted, however, that any redistribution of ocean mass will contribute to the terrestrial water change in the coastal regions.

In the global spherical harmonics method, equivalent water heights are computed based on monthly mean geopotential coefficients, whereas the regional approach is based on the *in situ* GRACE satellite-to-satellite tracking data and statistical inversion. Both of the global and regional approach has limited spatial resolution because of the altitude of the satellite orbits. The global approach is further limited in spatial resolution due to a necessary and possibly arbitrary truncation at a certain degree and order. Furthermore, both of the approaches need to consider the signal leakage from outside the interested region.

3.2. Estimating terrestrial water storage change regionally from *in situ* LOS gravity differences

3.2.1. Observation equation

Low-low SST allows to measure differences in satellite orbit perturbations over a distance of a few hundred kilometers. For example, GRACE provides the inter-satellite range, inter-satellite range rate, and inter-satellite range acceleration. Both range and range rate are the observations from which to estimate the monthly gravity model and to infer the terrestrial water change globally. Only range rates are used to calculate *in situ* geopotential differences and to estimate the terrestrial water change regionally, and only range accelerations will be used to calculate *in situ* LOS gravity differences and to estimate the terrestrial water change regionally. It is thus interesting to compare the regional solutions from *in situ* geopotential differences (using range rate) to the regional solutions from *in situ* LOS gravity differences (using range acceleration), in both the spatial and spectral domain, which will be one of the focuses in chapters 4 and 5.

Let $\mathbf{r}_1$ and $\mathbf{r}_2$ represent the position vectors of the two GRACE satellites, so $\mathbf{r}_{12}$ is the relative position vector between the two satellites. We can establish the following relationship:

$$\ddot{\rho}_{12} = (\mathbf{g}_2 - \mathbf{g}_1)\cdot\mathbf{e}_{12} + (\mathbf{a}_2 - \mathbf{a}_1)\cdot\mathbf{e}_{12} + \frac{\left|\dot{\mathbf{r}}_{12}\right|^2 - \dot{\rho}_{12}^2}{\rho_{12}}, \tag{3.7}$$

where ρ_{12}, $\dot{\rho}_{12}$, and $\ddot{\rho}_{12}$ are inter-satellite range, range rate, and range acceleration measurements (neglecting the random errors for now) respectively. $\mathbf{g}_1$ and $\mathbf{g}_2$ are the sum of the gravitational forces on satellite 1 and satellite 2, respectively. $\mathbf{a}_1$ and $\mathbf{a}_2$ are

the sum of the non-gravitational forces on the satellite 1 and satellite 2, respectively. $\dot{\mathbf{r}}_{12}$ is the relative velocity vector between the two satellites. $\mathbf{e}_{12}$ is the normalized LOS vector with $\mathbf{e}_{12} = \frac{\mathbf{r}_{12}}{|\mathbf{r}_{12}|}$. The quantity $(\mathbf{g}_2 - \mathbf{g}_1) \cdot \mathbf{e}_{12}$ is defined as the LOS gravity difference and will be denoted as $\mathbf{g}_{LOS}$.

With a-priori inter-satellite orbits and KBR range-acceleration measurements, one can use equation (3.7) as a condition equation to estimate $\mathbf{g}_{LOS}$ as well as the inter-satellite orbit vectors. Figure 3.1 is the flow chart of the procedure to calculate the LOS gravity difference measurements. Precise orbit, including position and velocity vectors, are assumed known and the KBR range-acceleration measurements are used as condition equations to adjust the orbit vectors at each epoch. Using the refined orbit vectors, we then estimate or model bias parameters associated with the accelerometer, and estimate the KBR empirical parameters, such as the bias, one cycle per revolution (1-cpr) parameters and 2-cpr parameters. The next step is to calculate the LOS gravity difference.

The relatively well-known effects of N-Body perturbations, solid earth tides, ocean tides, pole tides, atmospheric perturbations and ocean barotropic response to atmosphere are forward-modeled, based on the best available models. After removing all other effects we can calculate $\mathbf{g}_{LOS}^{hydrology}$ (for this study) from the following equation:

$$\mathbf{g}_{LOS}^{hydrology} = \mathbf{g}_{LOS} - \mathbf{g}_{LOS}^{mean\ \ earth} - \mathbf{g}_{LOS}^{N-Body} - \mathbf{g}_{LOS}^{tides} - \mathbf{g}_{LOS}^{ocean} - \mathbf{g}_{LOS}^{atmosphere} - \mathbf{g}_{LOS}^{others} . \qquad (3.8)$$

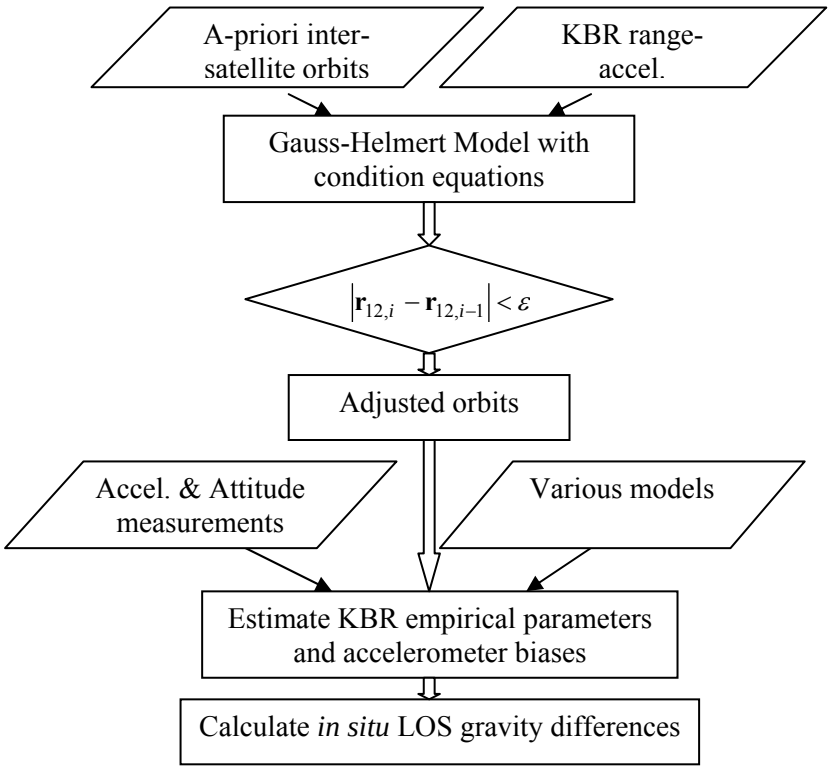

Figure 3.1: Procedure to calculate *in situ* LOS gravity differences

Taking the gradient of both sides of (3.4), we get

$$\nabla(V_{12}^{hydrology}(r_1,\theta_1,\lambda_1,r_2,\theta_2,\lambda_2;t)) = \nabla(G\rho_w(R\Delta\theta)(R\Delta\lambda)\sum_{i=1}^{N\times M}\left\{(\frac{\sin\theta_i}{l_1^i}-\frac{\sin\theta_i}{l_2^i})\Delta h_i\right\}) \quad (3.9)$$

We now describe the right hand side of equation (3.9) in more detail now:

$$\nabla(G\rho_w(R\Delta\theta)(R\Delta\lambda)\sum_{i=1}^{N\times M}\left\{(\frac{\sin\theta_i}{l_1^i}-\frac{\sin\theta_i}{l_2^i})\Delta h_i\right\}) = G\rho_w(R\Delta\theta)(R\Delta\lambda)\cdot \sum_{i=1}^{N\times M}\left\{(\nabla(\frac{\sin\theta_i}{l_1^i})-\nabla(\frac{\sin\theta_i}{l_2^i}))\Delta h_i\right\}. \quad (3.10)$$

The gradient operator is defined with respect to the spherical coordinates of satellite 1 (r_1,θ_1,λ_1) and satellite 2 (r_2,θ_2,λ_2). Also:

$$\frac{\partial}{\partial r}(\frac{1}{l_1^i}) = (-\frac{1}{l_1^{i\,2}})\frac{2r_1-2R\cos\psi_1^i}{2l_1^i} = -\frac{r_1-R\cos\psi_1^i}{l_1^{i\,3}}, \quad (3.11)$$

$$\frac{1}{r_1}\frac{\partial}{\partial\theta}(\frac{1}{l_1^i}) = \frac{1}{r_1}(-\frac{1}{l_1^{i\,2}})\frac{-2Rr_1}{2l_1^i}(-\cos\theta_i\sin\theta_1+\sin\theta_i\cos\theta_1\cos(\lambda_i-\lambda_1))$$

$$=\frac{1}{r_1}(\frac{Rr_1}{l_1^{i\,3}})(-\cos\theta_i\sin\theta_1+\sin\theta_i\cos\theta_1\cos(\lambda_i-\lambda_1)) \tag{3.12}$$

$$=\frac{R}{l_1^{i\,3}}(-\cos\theta_i\sin\theta_1+\sin\theta_i\cos\theta_1\cos(\lambda_i-\lambda_1)),$$

$$\frac{1}{r_1\sin\theta_1}\frac{\partial}{\partial\lambda}(\frac{1}{l_1^i}) = \frac{1}{r_1\sin\theta_1}(-\frac{1}{l_1^{i\,2}})\frac{-2Rr_1}{2l_1^i}\sin\theta_i\sin\theta_1\sin(\lambda_i-\lambda_1)$$

$$=\frac{1}{r_1\sin\theta_1}(\frac{Rr_1}{l_1^{i\,3}})\sin\theta_i\sin\theta_1\sin(\lambda_i-\lambda_1) \tag{3.13}$$

$$=\frac{R}{l_1^{i\,3}}\sin\theta_i\sin(\lambda_i-\lambda_1),$$

$$\frac{\partial}{\partial r}(\frac{1}{l_2^i}) = (-\frac{1}{l_2^{i\,2}})\frac{2r_2-2R\cos\psi_2^i}{2l_2^i} = -\frac{r_2-R\cos\psi_2^i}{l_2^{i\,3}}, \tag{3.14}$$

$$\frac{1}{r_2}\frac{\partial}{\partial\theta}(\frac{1}{l_2^i}) = \frac{1}{r_2}(-\frac{1}{l_2^{i\,2}})\frac{-2Rr_2}{2l_2^i}(-\cos\theta_i\sin\theta_2+\sin\theta_i\cos\theta_2\cos(\lambda_i-\lambda_2))$$

$$=\frac{1}{r_2}(\frac{Rr_2}{l_2^{i\,3}})(-\cos\theta_i\sin\theta_2+\sin\theta_i\cos\theta_2\cos(\lambda_i-\lambda_2)) \tag{3.15}$$

$$=\frac{R}{l_2^{i\,3}}(-\cos\theta_i\sin\theta_2+\sin\theta_i\cos\theta_2\cos(\lambda_i-\lambda_2)),$$

$$\frac{1}{r_2\sin\theta_2}\frac{\partial}{\partial\lambda}(\frac{1}{l_2^i}) = \frac{1}{r_2\sin\theta_2}(-\frac{1}{l_2^{i\,2}})\frac{-2Rr_2}{2l_2^i}\sin\theta_i\sin\theta_2\sin(\lambda_i-\lambda_2)$$

$$=\frac{1}{r_2\sin\theta_2}(\frac{Rr_2}{l_2^{i\,3}})\sin\theta_i\sin\theta_2\sin(\lambda_i-\lambda_2) \tag{3.16}$$

$$=\frac{R}{l_2^{i\,3}}\sin\theta_i\sin(\lambda_i-\lambda_2).$$

After taking the gradient, all the quantities are defined in the south-east-down frame. Since the quantity, $\mathbf{g}_{12}^{hydrology}\cdot\mathbf{e}_{12}$, is given in the inertial frame, we need to transform the gradient vector from the south-east-down direction to the n-frame and then to the i-frame. We thus obtain

$$\mathbf{g}_{12}^{hydrology}\cdot\mathbf{e}_{12} = G\rho_w(R\Delta\theta)(R\Delta\lambda)\sum_{i=1}^{N\times M}\left\{(C_{n,1}^i\nabla(\frac{\sin\theta_i}{l_1^i})-C_{n,2}^i\nabla(\frac{\sin\theta_i}{l_2^i}))\Delta h_i\right\}\cdot\mathbf{e}_{12}, \tag{3.17}$$

where R is the mean Earth radius, and other common variables inherit the same definitions from equation (3.4). $\mathbf{C}_{n,2}^{i}$ is the transformation matrix from the n-frame to the i-frame for the satellite 2, and $\mathbf{C}_{n,1}^{i}$ is the transformation matrix from the n-frame to the i-frame for the satellite 1. Note that $C_{n,1}^{i}$ is different from $C_{n,2}^{i}$. Equation (3.17) is used to estimate Δh_i from the observation $\mathbf{g}_{12}^{hydrology} \cdot \mathbf{e}_{12}$.

By replacing $\mathbf{g}_{12}^{hydrology} \cdot \mathbf{e}_{12}$ by $\mathbf{g}_{LOS}^{hydrology}$, the continental water storage is found from

$$\mathbf{g}_{LOS}^{hydrology}(r_1,\theta_1,\lambda_1;r_2,\theta_2,\lambda_2;t) = G\rho_w(R\Delta\theta)(R\Delta\lambda)\cdot \sum_{i=1}^{N\times M}\left\{(C_{n,1}^{i}\nabla(\frac{1}{l_1^i}) - C_{n,2}^{i}\nabla(\frac{1}{l_2^i}))\sin\theta_i h_i\right\}\cdot \mathbf{e}_{12}. \quad (3.18)$$

In the final step the estimated water storage h_i is corrected by considering the loading effect which was described in section 3.1.1.

3.2.2. Modified observation equation

The real GRACE data products have three levels: Level-0, Level-1A, Level-1B and Level-2. The detail of each level will be described in Chapter 5, and here it is just necessary to emphasize that Level-1B data products are the results of a possibly destructive or irreversible processing applied to both the Level-1A and Level-0 data [Bettadpur, 2004]. The proposed method largely depends on the quality of the range acceleration which is obtained by using a digital filter on the raw phase data of KBR [Wu et al, 2004]. If in some situations the quality of the derived range-acceleration measurements is worse than the minimum requirement, it is an alternative to switch to the use of range or range-rate data. To use range or range-rate data does not mean that the acceleration method is totally abandoned, because the proposed acceleration method can be modified accordingly by applying a Fredholm type integral equation.
Let us start again from Newton's equation of motion:

$$\ddot{\mathbf{r}} = \mathbf{g} + \mathbf{a}, \quad (3.19)$$

where $\ddot{\mathbf{r}}$ is the kinematic acceleration, $\mathbf{g}$ and $\mathbf{a}$ are the gravitational and non-gravitational accelerations, respectively. Since the acceleration can be obtained from the derivative of the potential with respect to position, it is easy to link the kinematic acceleration $\ddot{\mathbf{r}}$ to the spherical harmonics coefficients of the gravity field of the Earth. But, due to the low quality of $\ddot{\mathbf{r}}$ which is usually obtained from double-differencing of the position vector $\mathbf{r}$ which itself cannot guarantee sufficient accuracy either, equation (3.19) is not so useful despite its simplicity. Mayer-Gürr et al. [2005a] introduced a Fredholm type integral equation to avoid double-differencing of the position vector $\mathbf{r}$ for the case of CHAMP. The Fredholm integral equation is actually the solution of (3.19), and it reads:

$$\mathbf{r}(\tau) = (1-\tau)\mathbf{r}_A + \tau\mathbf{r}_B - T^2\int_{\tau'=0}^{1} K(\tau,\tau')(\mathbf{g}+\mathbf{a})(\tau';r,\dot{r},x,y)d\tau', \quad (3.20)$$

where $K(\tau,\tau') = \begin{cases}(1-\tau)(\tau'), & 0 \le \tau' \le \tau \\ (\tau)(1-\tau'), & \tau \le \tau' \le 1\end{cases}$, $\tau = \dfrac{(t-t_A)}{t_B - t_A}$, $t \in [t_A, t_B]$.

By using the above equation (3.20) and a numerical quadrature method, the spherical harmonics coefficients can be computed. The advantage of (3.20) is that it can be adjusted to different lengths of arc, and a double-difference method which usually increases high frequency noise could be avoided. (3.20) is suitable for the case of High-Low SST, like CHAMP.

It is easy to get the following models for the low-low SST case of GRACE (again neglecting random errors):

$$\ddot{\rho}_{12} = (\mathbf{g}_2 - \mathbf{g}_1)\cdot\mathbf{e}_{12} + (\mathbf{a}_2 - \mathbf{a}_1)\cdot\mathbf{e}_{12} + \frac{\left|\dot{\mathbf{r}}_{12}\right|^2 - \dot{\rho}_{12}^2}{\rho_{12}}, \tag{3.21}$$

$$\rho_{12}(\tau) = (1-\tau)\rho_{12}(t_A) + \tau\rho_{12}(t_B) - T^2\int_0^1 K(\tau,\tau')\ddot{\rho}_{12}(\tau')d\tau'. \tag{3.22}$$

Thus, we can also estimate the terrestrial water storage change from equation (3.21) with the use of (3.22); i.e., $\ddot{\rho}_{12}$ needs first to be solved from (3.22) by choosing a numerical quadrature method.

3.3 Solving the ill-posed problem

Improperly posed problems have appeared in the solution of integral equations of the first kind, or in downward continuation problems in potential theory, and so is the recovery of surface water change from the *in situ* geopotential differences or LOS gravity differences. One way to solve this problem is based on a Tikhonov-type regularization. The classical Tikhonov-regularization is defined as the minimization of the sum of the squared residual norm and the squared R-norm of the unknown parameters. Consequently, it has become common to add a positive-definite matrix multiplied by a regularization parameter to the matrix of the normal equations to stabilize the solution. For example, in the global recovery of the gravity field of the Earth, the inverse of the covariance matrix of the estimated parameters from a previous adjustment is usually chosen as this positive-definite matrix.

However, the difficulty of applying Tikhonov-regularization includes properly determining the value of the regularization parameter. If it is too big, then the solution will be smoothed too much; if it is too small, the instability will still exist. By using the regularization method, we are actually trying to pick a solution which satisfies some prior standards from a set of solutions. Many approaches to determine the regularization parameter have been tested. In our investigation, we shall compare three of them which were originally proposed by Koch and Kusche [2002], Schaffrin [2007], and Han [2005a]. In Koch and Kusche [2002], determining the regularization parameter is equivalent to estimating different variance components in a Bayesian setting, based on the a-priori information on the parameters; in contrast, the optimal choice of the regularization parameter is done through variance-ratio estimation in a model without prior information by Schaffrin [2007]. Han [2005a] introduces a stochastic model for the unknown quantities, their a-priori expectation and the associated covariance matrix, ending up with

a Random Effects Model, to solve the ill-conditioning problem. All the three approaches will be tested in our simulations, and the following three sections will give simple introductions to them, such as the background information, the observation equations and some necessary prior information. For each approach, a flowchart will be used to explain the procedure step by step.

3.3.1. Bayesian inference with variance components

Usually in Tikhonov-regularization, a positive-definite matrix times the regularization (or scaling) parameter is added to the matrix of normal equations to stabilize the solution. The matrix to be added to the matrix of normal equations can be the inverse of the covariance matrix of the unknown parameters if given by prior knowledge. This approach can be interpreted as Bayesian estimation with prior information rather than regularization in the Tikhonov sense. The scaling parameter can be obtained as the ratio of two variance components, as proposed by Arsenin and Krianev [1992]. Therefore, regularization may be replaced by Bayesian inference with unknown variance components [Koch and Kusche, 2002].

Let us start with the linear model in the formulation of Bayesian statistics

$$\mathbf{A}\mathbf{x} = E(\mathbf{y} \mid \mathbf{x}, \mathbf{e}) \text{, with } E\{\mathbf{e}\} = \mathbf{0},\ D\{\mathbf{e} \mid \sigma^2\} = \sigma^2 \mathbf{P}^{-1}, \tag{3.23}$$

where $\mathbf{A}$ denotes the $n \times m$ design matrix which will be assumed of full column rank, although ill-conditioned but not singular normal equations are expected. $\mathbf{x}$ is the $m \times 1$ vector of unknown random parameters for which prior information is available, σ^2 is the unknown variance factors, and $\mathbf{P}$ is the known $n \times n$ positive-definite weight matrix of the observation errors in the $n \times 1$ vector $\mathbf{y}$, $\mathbf{e}$ denotes the vector of random errors of the observations.

The prior information of the random parameters is given by

$$E\{\mathbf{x}\} = \boldsymbol{\mu}\ ,\ D\{\mathbf{x} \mid \sigma_\mu^2\} = \sigma_\mu^2 \mathbf{P}_\mu^{-1}, \tag{3.24}$$

with the $m \times 1$ vector $\boldsymbol{\mu}$, the variance factor σ_μ^2 and the $m \times m$ weight matrix $\mathbf{P}_\mu^{-1}$ of the parameters, thereby we can obtain

$$E\{\mathbf{y} = \mathbf{A}\mathbf{x} + \mathbf{e} \mid \mathbf{x}, \mathbf{e}\} = \mathbf{A}\mathbf{x}\ ,\ D(\mathbf{y} \mid \mathbf{x}, \mathbf{e}, \sigma^2) = \sigma^2 \mathbf{P}^{-1} + \sigma_\mu^2 \mathbf{A}\mathbf{P}_\mu^{-1}\mathbf{A}^T\ . \tag{3.25}$$

According to the linear model (3.23) with (3.24) and (3.25), the observation equations are given as

$$\mathbf{A}\mathbf{x} = \mathbf{y} - \mathbf{e} \text{, with } E\{\mathbf{y} = \mathbf{A}\mathbf{x} + \mathbf{e} \mid \mathbf{x}, \mathbf{e}\} = \mathbf{A}\mathbf{x}\ ,\ D(\mathbf{y} \mid \mathbf{x}, \mathbf{e}, \sigma^2) = \sigma^2 \mathbf{P}^{-1} + \sigma_\mu^2 \mathbf{A}\mathbf{P}_\mu^2 \mathbf{A}^T\ . \tag{3.26}$$

Suppose that there is only one type of observations $\mathbf{y}_1 = \mathbf{y}$, together with the prior information $\boldsymbol{\mu}$; we obtain the normal equations

$$\left(\frac{1}{\sigma_1^2} \mathbf{A}_1^{'} \mathbf{P} \mathbf{A}_1 + \frac{1}{\sigma_\mu^2} \mathbf{P}_\mu \right) \tilde{\mathbf{x}} = \frac{1}{\sigma_1^2} \mathbf{A}_1^{'} \mathbf{P} \mathbf{y}_1 + \frac{1}{\sigma_\mu^2} \mathbf{P}_\mu \boldsymbol{\mu}\ . \tag{3.27}$$

By introducing the scaling parameter λ with

$$\lambda = \frac{\sigma_1^2}{\sigma_{\boldsymbol{\mu}}^2}, \tag{3.28}$$

we obtain

$$\left(\mathbf{A}_1^{'}\mathbf{P}\mathbf{A}_1 + \lambda\mathbf{P}_{\mu}\right)\widetilde{\mathbf{x}} = \mathbf{A}_1^{'}\mathbf{P}\mathbf{y}_1 + \lambda\mathbf{P}_{\mu}\boldsymbol{\mu}. \tag{3.29}$$

By solving (3.29), we obtain

$$\widetilde{\mathbf{x}} = \left(\mathbf{A}_1^{'}\mathbf{P}\mathbf{A}_1 + \lambda\mathbf{P}_{\mu}\right)^{-1}\left(\mathbf{A}_1^{'}\mathbf{P}\mathbf{y}_1 + \lambda\mathbf{P}_{\mu}\boldsymbol{\mu}\right), \tag{3.30}$$

$$D(\widetilde{\mathbf{x}}) = \sigma_1^2\left(\mathbf{A}_1^{'}\mathbf{P}\mathbf{A}_1 + \lambda\mathbf{P}_{\mu}\right)^{-1}\left(\mathbf{A}_1^{'}\mathbf{P}\mathbf{A}_1\right)\left(\mathbf{A}_1^{'}\mathbf{P}\mathbf{A}_1 + \lambda\mathbf{P}_{\mu}\right)^{-1}. \tag{3.31}$$

For $\boldsymbol{\mu} = 0$ the solution vector resembles that of the Tikhonov regularization and of ridge regression.

The partial redundancies r_1 and $r_{\boldsymbol{\mu}}$, associated with the observation $\mathbf{y}_1$ and the prior information $\boldsymbol{\mu}$, respectively, are computed by

$$\begin{cases} r_1 = n_1 - tr(\frac{1}{\sigma_1^2}\mathbf{A}_1^{'}\mathbf{P}\mathbf{A}_1\mathbf{N}^{-1}), \\ r_{\boldsymbol{\mu}} = m - tr(\frac{1}{\sigma_{\boldsymbol{\mu}}^2}\mathbf{P}_{\boldsymbol{\mu}}\mathbf{N}^{-1}), \end{cases}, \tag{3.32}$$

,

where

$$N = \frac{1}{\sigma_1^2}\mathbf{A}_1^{'}\mathbf{P}\mathbf{A}_1 + \frac{1}{\sigma_{\boldsymbol{\mu}}^2}\mathbf{P}_{\boldsymbol{\mu}} \tag{3.33}$$

is the normal equations matrix.

In order to avoid the computation of the inverse matrix, $\mathbf{N}^{-1}$, an alternative method to calculate r_1 and $r_{\boldsymbol{\mu}}$ exists by a stochastic trace estimation, but will not be elaborated here [Koch and Kusche, 2002]. The iteration begins by specifying initial values for σ_1^2 and $\sigma_{\boldsymbol{\mu}}^2$, then computing the residual vectors $\widetilde{\mathbf{e}}_1$ and $\widetilde{\mathbf{e}}_{\boldsymbol{\mu}}$, and getting the estimates $\hat{\sigma}_1^2$ and $\hat{\sigma}_{\boldsymbol{\mu}}^2$, eventually. Iteration is performed until both variance component estimates converge and the final Bayesian solution, $\widetilde{\mathbf{x}}$, is achieved. Figure 3.2 shows the flowchart of the detailed procedure.

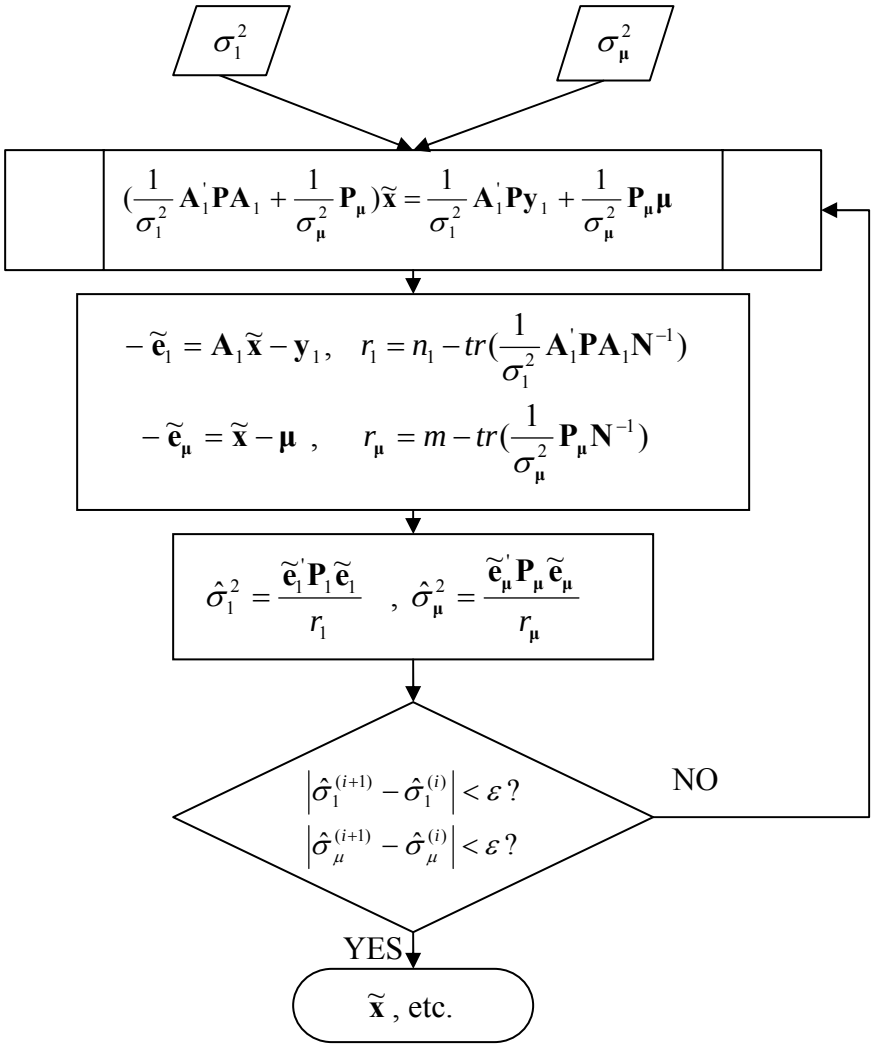

Figure 3.2: Bayesian inference with variance components

3.3.2. An optimal regularization factor via formulas for the repro-BIQUUE of variance components

The Tikhonov-Phillips regularization became widely known from its application to integral equations from the work of A.N. Tikhonov and D.L. Phillips. It is based on the minimization of the sum of the (weighted) squared residual norm and the squared R-norm of the unknown parameters within a Gauss-Markov Model. However, the regularization parameter α, which is to determine the trade-off between the (weighted) Squared residual norm and the squared R-norm of the unknown parameters, is usually unknown. Often in practical problems, the regularization parameter α, is customized for a specific problem and cannot be adapted to other purposes.

The Tikhonov-Phillips regularization, also knows as "ridge regression" in statistics, is equivalent to S(Selective)-homBLE (Best homogeneously Linear Estimation) [Schaffrin, 2007]. Let us introduce the (possibly rank-deficient) Gauss-Markov Model

$$\mathbf{y} = \mathbf{A}\boldsymbol{\xi} + \mathbf{e}\,,\ \mathrm{rk}\,\mathbf{A} =: q \le m < n\,,\ e \sim (0, \sigma_{\mathrm{y}}^2\ \underset{n\times n}{\mathbf{P}}^{-1} =: \textstyle\sum_{\mathrm{y}})\,, \tag{3.34}$$

in which $\mathbf{y}$ is the $n\times 1$ vector of observations, $\mathbf{A}$ is the $n\times m$ coefficient matrix, $\boldsymbol{\xi}$ is the $m\times 1$ vector of unknown parameters, $\mathbf{e}$ is the $n\times 1$ vector of random errors, σ_{y}^2 is the unknown variance component, $\mathbf{P}$ is the $n\times n$ symmetric, positive-definite weight matrix, $\sum_{\mathrm{y}}$ is the $n\times n$ symmetric, positive-definite dispersion matrix. With LEast-Squares Solution, the normal equations are

$$\mathbf{N}\hat{\boldsymbol{\xi}} = \mathbf{c}\ \text{ for } [\mathbf{N}, \mathbf{c}] := \mathbf{A}^T\mathbf{P}[\mathbf{A}, \mathbf{y}]\,. \tag{3.35}$$

However in inverse problem the coefficient matrix, $\mathbf{A}$, is often ill-conditioned numerically. The normal equations can still be solved but the estimates will endure unacceptable uncertainties, since any measurement errors in $\mathbf{y}$ will be magnified by the large eigenvalues of $\mathbf{N}^{-1}$ (inverse eigenvalues of $\mathbf{N}$). As an alternative, let us first introduce the homogeneously linear estimators,

$$\bar{\boldsymbol{\xi}} = \mathbf{L}\mathbf{y}\,, \tag{3.36}$$

where the $m\times n$ matrix $\mathbf{L}$ is to be determined. By applying the minimum MSE (Mean Sqaure Error) principle we obtain

$$\begin{aligned} trMSE(\bar{\boldsymbol{\xi}}) &= tr(D(\bar{\boldsymbol{\xi}}) + E(\bar{\boldsymbol{\xi}} - \boldsymbol{\xi})(\bar{\boldsymbol{\xi}} - \boldsymbol{\xi})^T) \\ &= \sigma_y^2 tr[(\mathbf{L}\mathbf{P}^{-1}\mathbf{L}^T) + (\mathbf{I} - \mathbf{L}\mathbf{A})\boldsymbol{\xi}\boldsymbol{\xi}^T(\mathbf{I} - \mathbf{L}\mathbf{A})^T] = \min_{\mathbf{L}^T}. \end{aligned} \tag{3.37}$$

If the prior knowledge on $\boldsymbol{\xi}$ does not exist, we can introduce a substitute matrix, $\alpha^{-1}\mathbf{S}$, to replace $\boldsymbol{\xi}\boldsymbol{\xi}^T$, where $\mathbf{S}$ is a given symmetric nonnegative-definite matrix and $\alpha \in \mathbf{R}_+$ is an unknown positive constant. Note that although the rank of $\boldsymbol{\xi}$ is 1, $\mathbf{S}$ may even be chosen as an invertible matrix. Then we arrive at the new target function,

$$\sigma_y^2 tr[(\mathbf{L}\mathbf{P}^{-1}\mathbf{L}^T) + \alpha^{-1}(\mathbf{I} - \mathbf{L}\mathbf{A})\mathbf{S}(\mathbf{I} - \mathbf{L}\mathbf{A})^T] = \min_{\mathbf{L}^T}. \tag{3.38}$$

Since the variance term $tr(\mathbf{L}\mathbf{P}^{-1}\mathbf{L}^T)$ and the bias term $tr(\mathbf{I} - \mathbf{L}\mathbf{A})\mathbf{S}(\mathbf{I} - \mathbf{L}\mathbf{A})^T$ are balanced by the factor α^{-1}, α functions as "weight" for the two terms. Thus we shall call the estimate $\bar{\boldsymbol{\xi}}$, the α-weighted S-homBLE. The normal equations (for $\mathbf{L}^T$) are now obtained as,

$$(\mathbf{P}^{-1} + \mathbf{A}\boldsymbol{\xi}\sigma_y^{-2}\boldsymbol{\xi}^T\mathbf{A}^T)\mathbf{L}^T = \mathbf{A}\boldsymbol{\xi}\sigma_y^{-2}\boldsymbol{\xi}^T\,, \tag{3.39}$$

which leads to

$$(\alpha\sigma_Y^2\mathbf{P}^{-1} + \mathbf{A}\mathbf{S}\mathbf{A}^T)\mathbf{L}^T = \mathbf{A}\mathbf{S}\,, \tag{3.40}$$

and

$$\mathbf{L} = \mathbf{S}\mathbf{A}^T(\alpha\sigma_Y^2\mathbf{P}^{-1} + \mathbf{A}\mathbf{S}\mathbf{A}^T)^{-1}. \tag{3.41}$$

We then get the α-weighted S-homBLE as

$$\begin{aligned}\bar{\boldsymbol{\xi}} &= \mathbf{L}\mathbf{y} \\ &= \mathbf{S}\mathbf{A}^T(\alpha\sigma_Y^2\mathbf{P}^{-1} + \mathbf{A}\mathbf{S}\mathbf{A}^T)^{-1}\mathbf{y} \\ &= \mathbf{S}\mathbf{A}^T\mathbf{P}(\alpha\sigma_Y^2 + \mathbf{A}\mathbf{S}\mathbf{A}^T\mathbf{P})^{-1}\mathbf{y} \\ &= (\alpha\sigma_y^2\mathbf{I}_m + \mathbf{S}\mathbf{N})^{-1}\mathbf{S}\mathbf{c}\end{aligned} \tag{3.42}$$

Starting from the simplest case, namely, the matrix $\mathbf{S}$ is nonsingular, we obtain

$$\bar{\boldsymbol{\xi}} = (\alpha\sigma_{\mathrm{y}}^2\mathbf{S}^{-1} + \mathbf{N})^{-1}\mathbf{c} = (\alpha\mathbf{S}^{-1} + \sigma_{\mathrm{y}}^{-2}\mathbf{N})^{-1}(\alpha\mathbf{S}^{-1}\cdot\mathbf{0} + \sigma_{\mathrm{y}}^{-2}\mathbf{c}), \tag{3.43}$$

$$\begin{aligned}D(\bar{\boldsymbol{\xi}}) &= (\alpha\mathbf{S}^{-1} + \sigma_{\mathrm{y}}^{-2}\mathbf{N})^{-1}(\sigma_{\mathrm{y}}^{-2}\mathbf{N})(\alpha\mathbf{S}^{-1} + \sigma_{\mathrm{y}}^{-2}\mathbf{N})^{-1} \\ &= (\alpha\mathbf{S}^{-1} + \sigma_{\mathrm{y}}^{-2}\mathbf{N})^{-1} - (\alpha\mathbf{S}^{-1} + \sigma_{\mathrm{y}}^{-2}\mathbf{N})^{-1}(\alpha\mathbf{S}^{-1})(\alpha\mathbf{S}^{-1} + \sigma_{\mathrm{y}}^{-2}\mathbf{N})^{-1},\end{aligned} \tag{3.44}$$

where $\mathbf{0}$ denotes a *fixed m×1* vector of zeros, in contrast to the vector of "prior" information used by Koch and Kusche [2002, p.261]. Furthermore, we may apply the formulas for repro-BIQUUE (reproducing Best Invariant Quadratic Uniformly Unbiased Estimate) of two "variance components" (here α^{-1} and σ_{y}^2) to determine the ratio

$$\lambda := \frac{\sigma_{\mathrm{y}}^2}{\alpha^{-1}} = \alpha\sigma_{\mathrm{y}}^2. \tag{3.45}$$

This ratio λ is nothing but the Tikhonov-Phillips regularization factor.

Let us introduce the following vectors

$$\bar{\mathbf{e}} := \mathbf{y} - \mathbf{A}\bar{\boldsymbol{\xi}} = \mathbf{y} - \mathbf{A}(\mathbf{N} + \lambda\mathbf{S}^{-1})^{-1}\mathbf{c}, \tag{3.46}$$

$$\bar{\mathbf{e}}_0 := \mathbf{0} - \bar{\boldsymbol{\xi}} = -(\mathbf{N} + \lambda\mathbf{S}^{-1})^{-1}\mathbf{c}. \tag{3.47}$$

After applying the formulas for repro-BIQUUE we can get

$$\hat{\sigma}_{\mathrm{y}}^2 = \hat{\sigma}_{\mathrm{y}}^2(\hat{\lambda}) = \bar{\mathbf{e}}^T\mathbf{P}\bar{\mathbf{e}}\cdot\left[n - tr(\mathbf{N} + \lambda\mathbf{S}^{-1})^{-1}\mathbf{N}\right] \geq 0, \tag{3.48}$$

$$\hat{\lambda} = \left(\frac{n}{n - tr(\mathbf{N} + \lambda\mathbf{S}^{-1})^{-1}\mathbf{N}} - 1\right)\cdot\left(\frac{\bar{\mathbf{e}}^T\mathbf{P}\bar{\mathbf{e}}}{\bar{\mathbf{e}}_0^T\mathbf{S}^{-1}\bar{\mathbf{e}}_0}\right) \geq 0, \tag{3.49}$$

which ought to be solved iteratively. After convergence $\hat{\lambda}$ can be entered into (3.48) to obtain $\hat{\sigma}_{\mathrm{y}}^2$, and a new solution $\bar{\boldsymbol{\xi}}$ ought to be computed from (3.43), along with the vectors $\bar{\mathbf{e}}$ and $\bar{\mathbf{e}}_0$ from (3.46) and (3.47), in order to start a new cycle. This procedure is continued until $\hat{\lambda}$ converges.

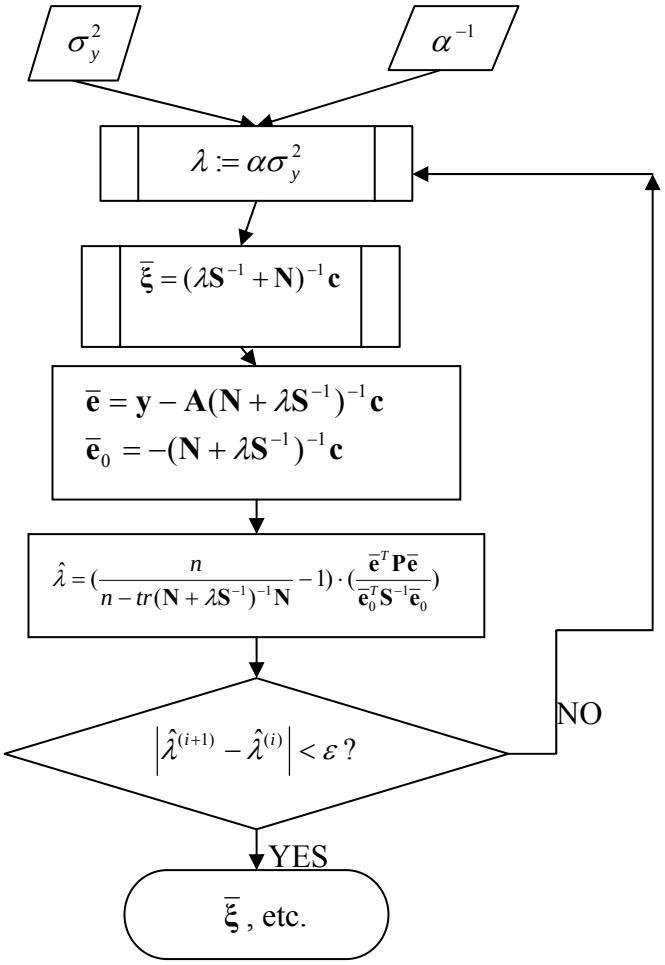

Figure 3.3: An optimal regularization factor via formulas for the repro-BIQUUE of variance components

3.3.3. Iterative least-squares estimation with simultaneous updating of a prior covariance

Let us first introduce the observation equations as follows:

$$\mathbf{y} = \mathbf{A}\boldsymbol{\xi} + \mathbf{e}\,,\ \mathbf{e} \sim (\mathbf{0}, \sigma_y^2\mathbf{I})\,, \tag{3.50}$$

where $\mathbf{y}$ is the $n \times 1$ vector of observations, such as geopotential differences or LOS gravity differences from the satellite data, $\boldsymbol{\xi}$ is the $m \times 1$ parameter vector to be estimated, such as the continental water change, $\mathbf{A}$ is the known $n \times m$ coefficient matrix, and $\mathbf{e}$ is the error vector belonging to the measurements in $\mathbf{y}$. The variance component σ_y^2 ought to be determined.

A-priori information such as prior estimates, $\mathbf{x}_0$, and the associated covariance matrix, $\mathbf{C}_x$, for ξ , is utilized to resolve the ill-conditioned problem existing in the downward continuation process. The corresponding a-priori information equations can be written in terms of pseudo-observations:

$$\mathbf{x_0} = \mathbf{I}\xi + \mathbf{e_0},\ \mathbf{e_0} \sim (\mathbf{0}, \mathbf{C_x}). \tag{3.51}$$

The least-squares solution including the estimated parameters $\hat{\xi}$, the dispersion matrix of the estimates, $D\{\hat{\xi}\}$, and a variance component estimate, $\hat{\sigma}_y^2$, are given as follows:

$$\hat{\xi} = (\mathbf{A}^T\mathbf{A} + \sigma_y^2\mathbf{C}_x^{-1})^{-1}(\mathbf{A}^T\mathbf{y} + \sigma_y^2\mathbf{C}_x^{-1}\mathbf{x}_0), \tag{3.52}$$

$$\hat{\sigma}_y^2 = \frac{\mathbf{y}^T\mathbf{y} - \hat{\xi}^T(2\mathbf{A}^T\mathbf{y}) + \hat{\xi}^T(\mathbf{A}^T\mathbf{A})\hat{\xi}}{n - (\mathbf{x}_0 - \hat{\xi})^T\mathbf{C}_x^{-1}(\mathbf{x}_0 - \hat{\xi})}, \tag{3.53}$$

$$D\{\hat{\xi}\} = (\mathbf{A}^T\mathbf{A}\sigma_y^{-2} + \mathbf{C}_x^{-1})^{-1}, \tag{3.54}$$

where n is the number of the observations. All three quantities contain the variance component, σ_y^2 along with $\hat{\xi}$. Therefore, we need to solve for $\hat{\xi}$ and $\hat{\sigma}_y^2$ iteratively, starting with an initial value of σ_y^2. After the convergence, we get $D\{\hat{\xi}\}$ by putting the converged value $\hat{\sigma}_y^2$, into (3.54), and similarly into (3.52) to get $\hat{\xi}$.

However, in reality we may not have good information about the covariance matrix, $\mathbf{C}_x$. In this case we choose to perform an iteration too for $\mathbf{C}_x$, starting from an initial covariance matrix. To avoid estimating all the unknown parameters inside $\mathbf{C}_x$, we instead approximate $\mathbf{C}_x$ by a covariance function model with only two parameters such as the variance and correlation distance:

$$\mathbf{C}_x\{i, j\} = \sigma_x^2 \exp(-\frac{r_{i,j}}{l}), \tag{3.55}$$

where σ_x^2 and l are variance and correlation distance, respectively, and $r_{i,j}$ is the distance between the two locations of two components in the vector, $\mathbf{x}$. During the iterations for $\hat{\xi}$ and $\hat{\sigma}_y^2$, we add one more step for $\mathbf{C}_x$. We can namely compute the empirical values for each covariance, $\hat{\mathbf{C}}_x\{i, j\}$, using the intermediate estimates, $\hat{\xi}$. The distance is known by two coordinates. As a result, the least-squares estimates of σ_x^2 and l can be computed after linearization of (3.55). Then, the covariance matrix, $\hat{\mathbf{C}}_x$, is updated with new estimates of σ_x^2 and l. With this new covariance matrix, the next iteration for $\hat{\xi}$ and $\hat{\sigma}_y^2$ is performed. The iteration is continued until the solutions converge. It has to be pointed out that the measurements in $\mathbf{y}$ has been used twice, i.e., once in the procedure of computing the empirical values for $\hat{\mathbf{C}}_x\{i, j\}$ through the

intermediate estimates, $\hat{\boldsymbol{\xi}}$, and once more used in estimating $\hat{\boldsymbol{\xi}}$ using (3.52). This should be avoided in a typical Least-Squares solution, so we can only apply the procedure above to achieve a solution when it is really difficult to get any good information about the covariance matrix, $\mathbf{C}_x$.

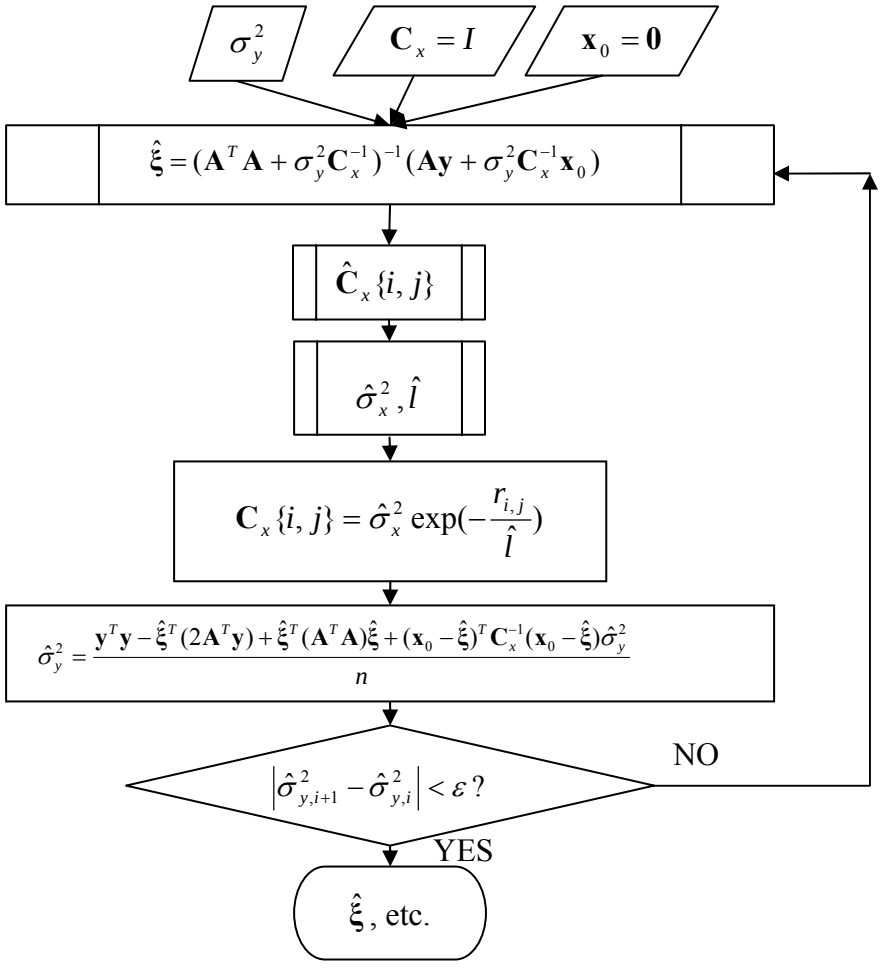

Figure 3.4: Iterative least-squares estimation with simultaneous updating of a prior covariance

CHAPTER 4

A SIMULATION TO ESTIMATE TERRESTRIAL WATER STORAGE CHANGE GLOBALLY AND REGIONALLY

4.1. Closed-loop simulation

A closed-loop simulation study was used, in order to show and prove the performance of the different strategies to recover the terrestrial water change globally and regionally as described in Chapter 2 and Chapter 3.

The raw data of the continental water storage for our simulations come from the NCEP (National Centers for Environmental Prediction)/NCAR (National Center for Atmospheric Research) reanalysis project (www.cdc.noaa.gov). Daily continental water storage, defined as the sum of soil wetness and snow water, is computed by converting the soil water (in volumetric fraction) and snow water (kg/m^2) into equivalent water thickness (ftp://ftp.csr.utexas.edu/pub/ggfc/water/NCEP). The time span of these data is from Jan. 1979 to Dec. 2004; they are defined as the sum of soil wetness and snow water within two layers (0-10 and 10-200 cm). The spatial resolution is about 2 degrees. The gridded data sets cover all continents, except Greenland and Antarctica. Missing data in Greenland and Antarctica, as well as those over the oceans are set to zero. Figure 4.1 shows the global terrestrial water storage on Jan.1, 2003.

It must be emphasized, that what GRACE is able to observe, is the terrestrial water storage change instead of the terrestrial water storage itself. For each grid point, by using the daily water storage data from the NCEP/NCAR model, daily water storage change can be calculated, using either the mean value of a whole year, or a monthly mean value from a certain month such as the first month, as the reference.

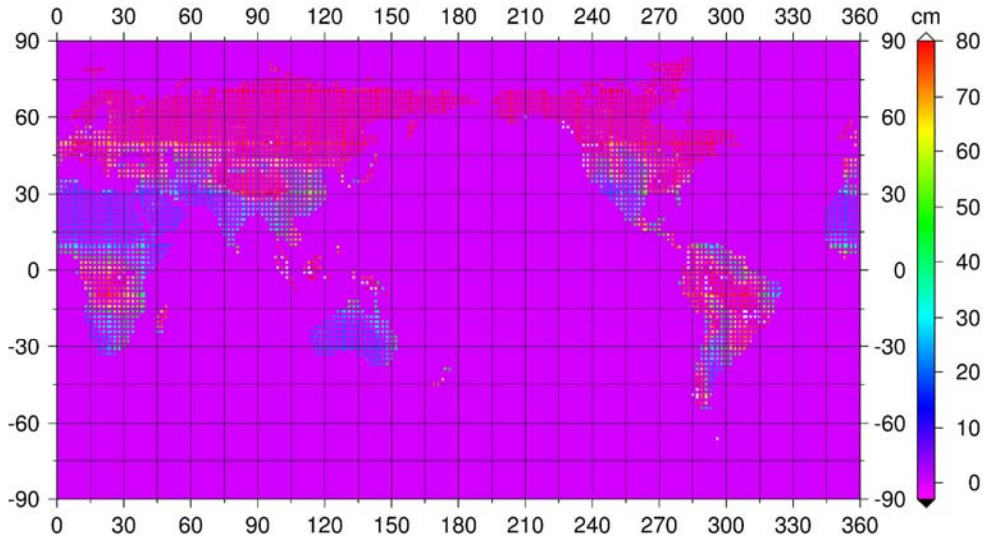

Figure 4.1: Global continental water storage on Jan.1, 2003 (NCEP/NCAR)

In this study, one year (2003) of daily gridded data of NCEP/NCAR are used to calculate daily water storage change. For each grid point, we first calculate the mean value of water storage for the first month. The next step is to subtract the monthly mean value of the first month from the water storage of each day at every grid point, which is the so-called daily water storage change, representing the residual water content at a certain time with respect to the water content at a reference epoch, i.e., the first month of the year. The whole year daily continental water storage changes are then used to fit Stokes' coefficients, complete to degree and order 90, corresponding to a spatial resolution of 2×2 degree. The daily Stokes' coefficients are then added to the static gravity field of the Earth, EGM96, to get 365 total daily modified EGM96 models.

To generate perturbed orbits of the two GRACE satellites by numerical integration, the daily modified EGM96 models are employed up to degree and order 90. The simulated orbits of the two GRACE satellites have the following characteristics:

- Initial altitude: ~450 km
- Inclination: $\sim 89^{\circ}$
- Eccentricity: ~0.001 for nearly circular orbits
- Time interval: 5 seconds
- Consider mean Earth rotation only (no nutation, precession, UT1 nor other variations)
- Data span of 365 days

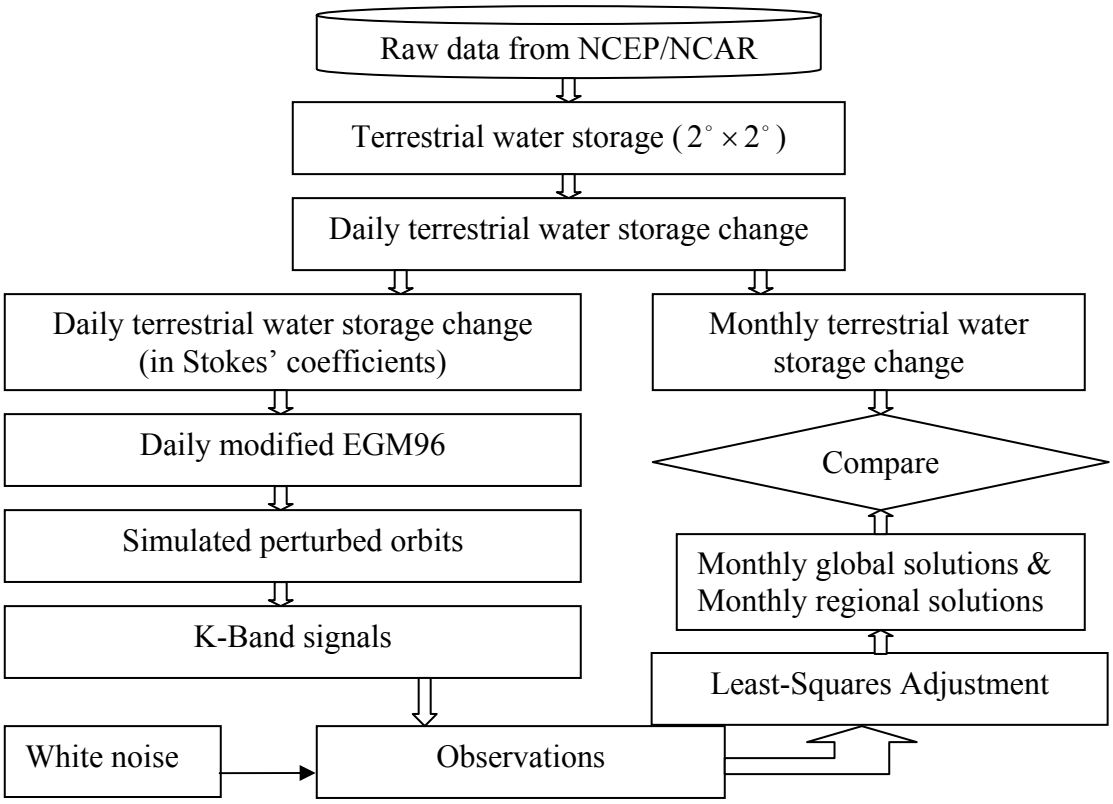

Figure 4.2: Flowchart of the closed-loop simulation

The synthetic observations, KBR range, range rate and range acceleration, are computed according to the simulated GRACE orbits. Reasonable random noise, at an order of magnitude less than the observations are added to the simulated observables.

4.2. Global and regional solutions from *in situ* geopotential differences

Figure 4.3 shows the time series of the global terrestrial water storage change in 2003 according to the raw data from NCEP/NCAR. The ocean areas are augmented with zeros and masked out to highlight the results over the continents. The pronounced features of terrestrial water storage changes over the continents are clearly visible in the large tropical river basins, such as Amazon in South America, Congo and Niger in Africa, Ganges and Brahmapoutra in North India, Mississippi in North America, Ob and Yenissei in the Russian basins, and Murray-Darling in Australia.

The global data of terrestrial water storage change (padding zeros for the ocean areas) have been expanded into time averaged monthly sets of spherical harmonics complete to degree and order 90. These twelve monthly sets of spherical harmonics will be

considered as the "truth", i.e., reality, and will be compared to both the global solutions from *in situ* geopotential differences and the global solutions from *in situ* LOS gravity differences. A weighted least-squares approach is used to estimate the annual component, semi annual component, and a linear trend for the twelve sets of the monthly mean terrestrial water storage change,

$$y(t) = a + b \cdot t + c \cdot \cos(\frac{2\pi}{T_1}(t - t_0)) + d \cdot \sin(\frac{2\pi}{T_1}(t - t_0)) + e \cdot \cos(\frac{2\pi}{T_2}(t - t_0)) + f \cdot \sin(\frac{2\pi}{T_2}(t - t_0)) \quad , \tag{4.1}$$

where, a, b, c, d, e, f are the unknown parameters for the constant, linear trend, annual amplitude for the cosine part, annual amplitude for the sine part, semi-annual amplitude for the cosine part and semi-annual for the sine part. t denotes the time and it can be in the unit of year, and t_0 is the reference time. T_1 and T_2 are the annual period and semi-annual period respectively. The units of t and T_1 and T_2 should be the same. $y(t)$ is the monthly mean terrestrial water storage change at a grid point at time t.

Figure 4.4 shows the cosine part (c) and the sine part of the annual signal (d). It also confirms where pronounced features of continental water storage changes exist. Based on the two figures, we pick up an area which is appropriate for us to do regional inversions. "Appropriate" means that the area cannot be either too big which will lead to a huge normal matrix for the regional inversion, or too small which could be difficult for any precise recovery of water change, considering the low spatial resolution from the measurements at an altitude of 450 km. The Amazon area is chosen to be the area to test our global and regional inversions using both *in situ* geopotential differences and *in situ* LOS gravity differences. The other reason to choose the Amazon basin is that in the next chapter we will compare different regional and global solutions, using the real GRACE L1B data over the study area.

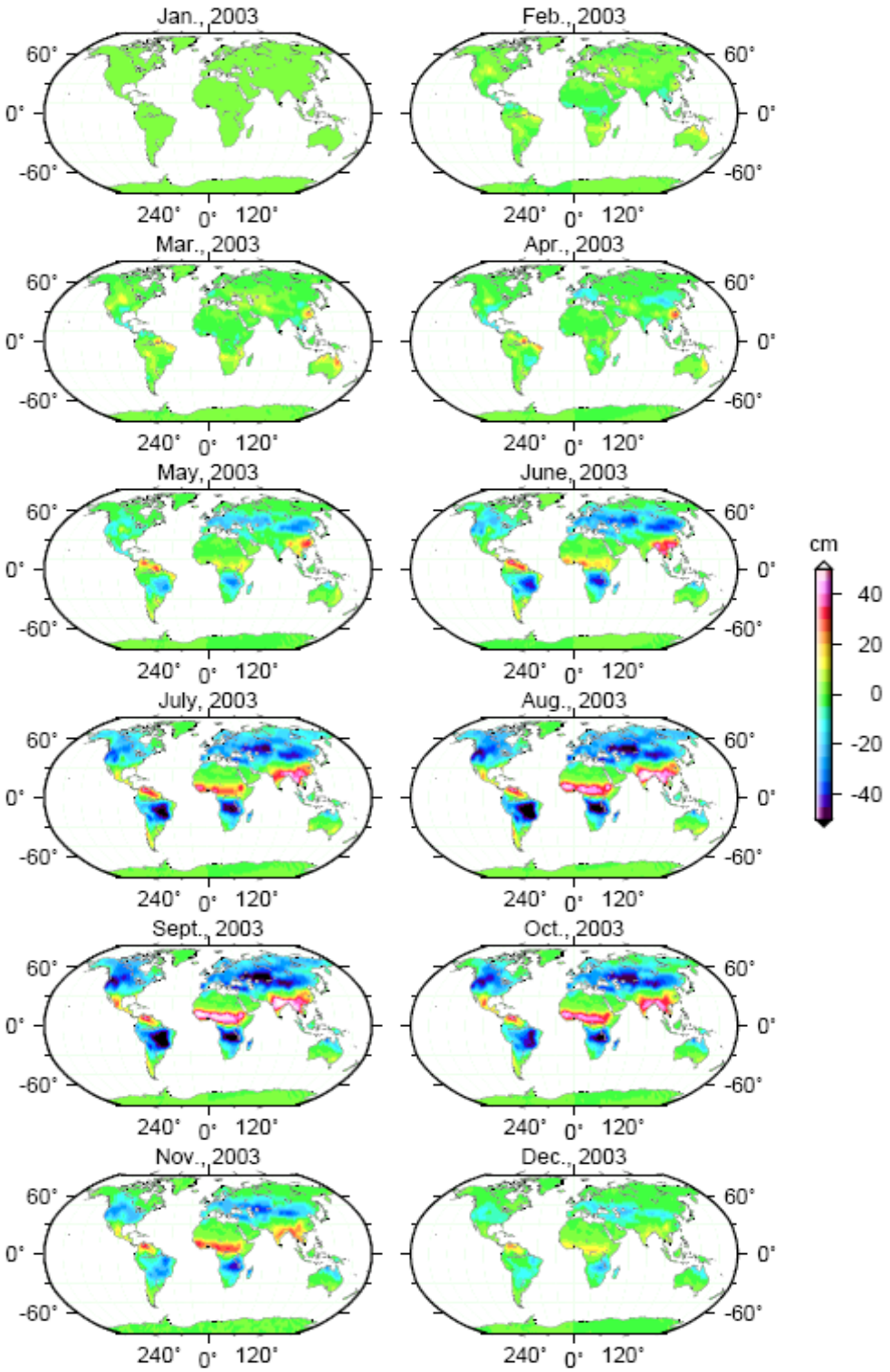

Figure 4.3: Global terrestrial water storage changes in 2003 according to the hydrology model from NCEP/NCAR, with reference to the mean value of the first month of 2003

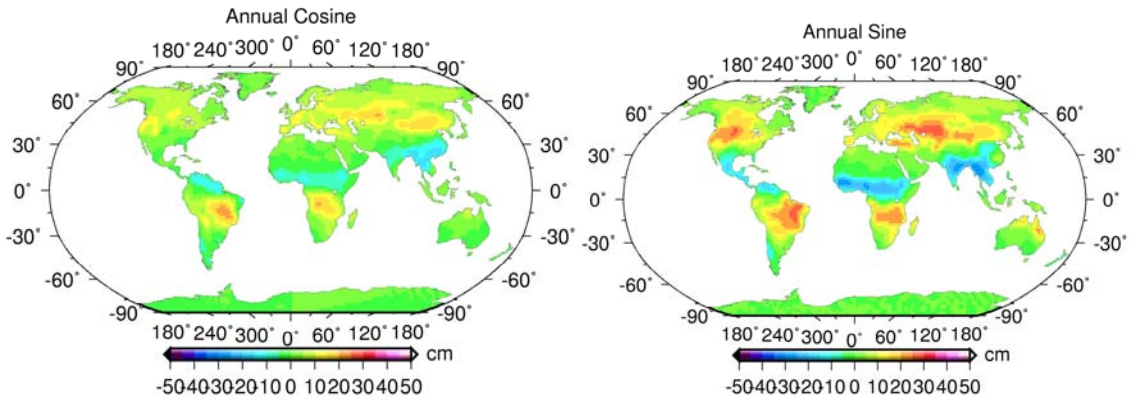

Figure 4.4: The cosine part and the sine part of the annual signal of the global terrestrial water storage change

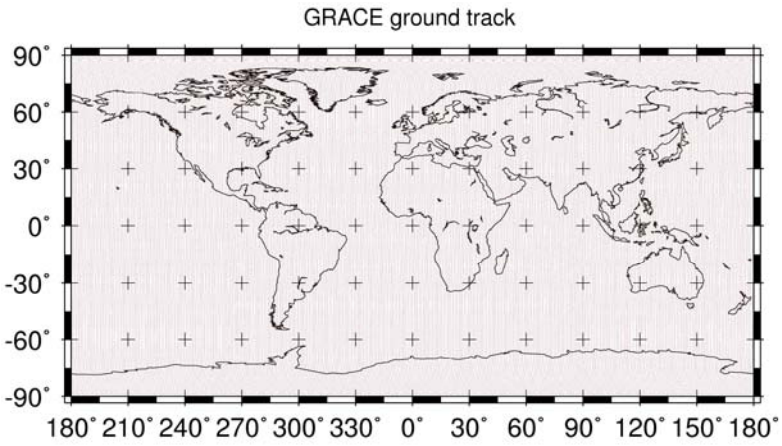

Figure 4.5: Ground track of the GRACE satellites in July 2003

By adding the daily spherical harmonics of the continental water change to EGM96, the daily modified EGM96 models are used to simulate daily orbits of the two GRACE satellites. Only the gravity field of the Earth is considered, and a uniform rotation of the Earth is applied for the numerical integration of the GRACE satellites. No N-body effects, no tides and no non-conservative forces are considered. The initial positions of the two GRACE satellites are chosen such that their initial altitudes are around 450 km, the inclinations are about 89°, etc. The other important thing is to set the initial distance

between the satellites to be around 250 km. The daily orbits are continuous in a month. In order to keep the distance between the two GRACE satellites to be always close to 250 km, the positions of the two satellites are set to the initial positions at the start day of each month. The time interval for the integration is 10 seconds, so in a month there are around 259200 observations. Figure 4.5 shows the ground track pattern for July of 2003, which is uniform and dense globally.

Assume that there is a mass anomaly on or under the surface of the Earth, the range, range rate and range acceleration between the two GRACE satellites will change accordingly. Because the KBR range measurement is always biased and the bias cannot be predicted, only range rate and range acceleration are studied in our simulation. As the range rate is the time derivative of the range, and the range acceleration is the time derivative of the range rate, we can see from our simulated data that, whenever the range rate reaches the maximum value or the minimum value, the range acceleration is zero as shown in Figure 4.6.

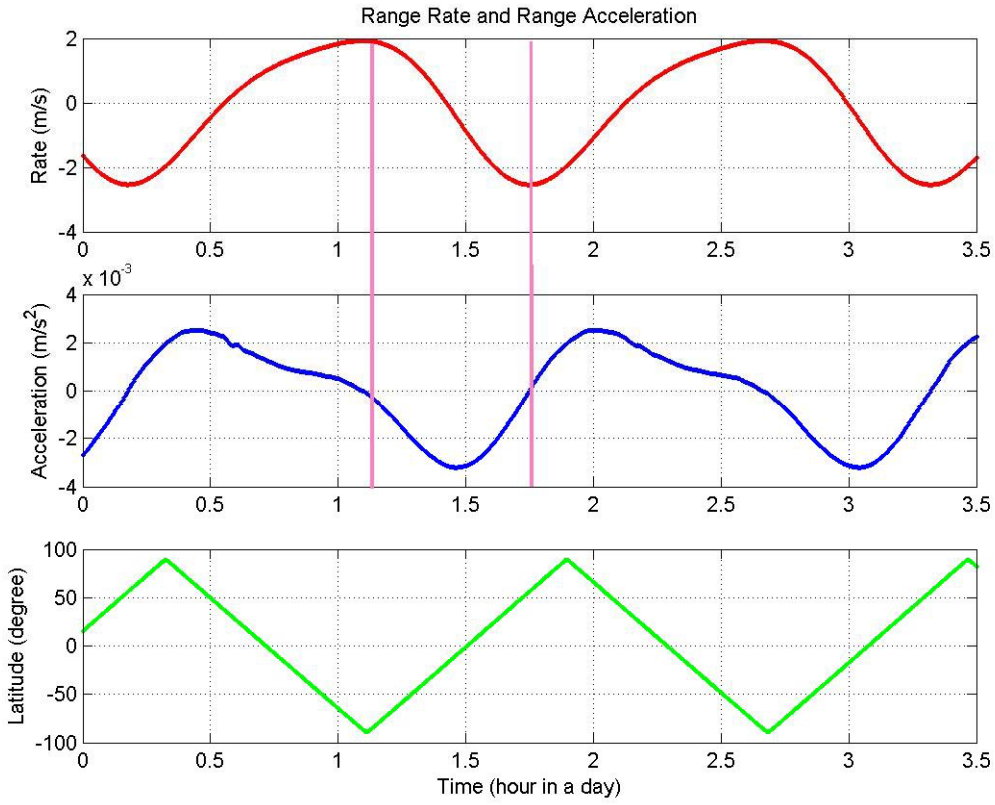

Figure 4.6: Range rate (red) and range acceleration (blue). The green line represents the average latitude of the two GRACE satellites.

Range and range rate between the two satellites are calculated using the simulated positions of the two GRACE satellites, so the disturbing geopotential difference can be simulated. No friction energy is modeled or considered here in our simulation. EGM96 coefficients are used as the reference gravity field up to degree and order 90. Figure 4.7 shows the global disturbing potential differences of July 2003. Based on the same simulated positions of the two satellites, Figure 4.8 presents the disturbing LOS gravity differences globally of the same month. For the convenience of future comparisons with the modeling errors of ocean tides and of the atmosphere, we set the unit of the color scale of the plot to be $10^{-3}\ \ m^2/s^2$ even though the overall magnitude of disturbing geopotential differences on the continents are at the order of $10^{-2}\ \ m^2/s^2$. The unit of the color scale of the plot of the disturbing LOS gravity differences is set to be $10^{-10}\ \ m/s^2$ for the same reason.

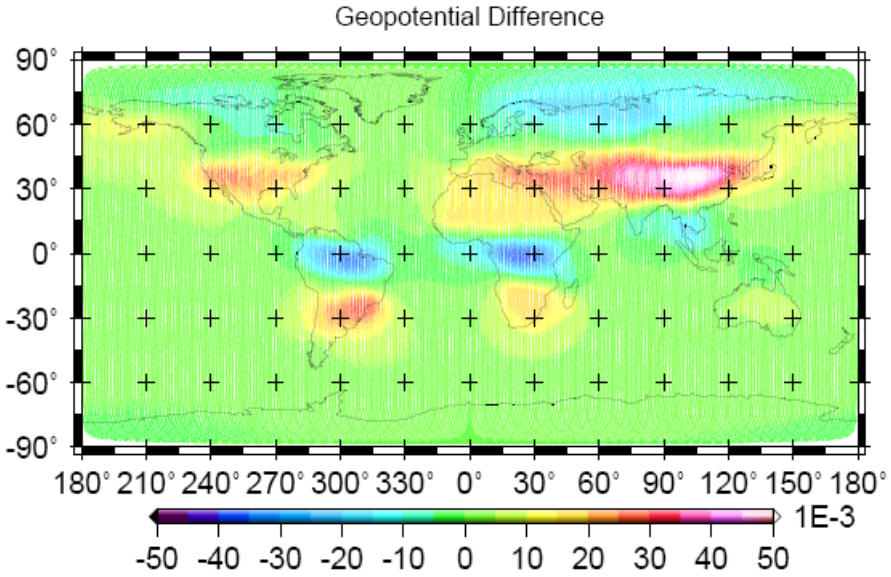

Figure 4.7: Simulated geopotential differences in July 2003

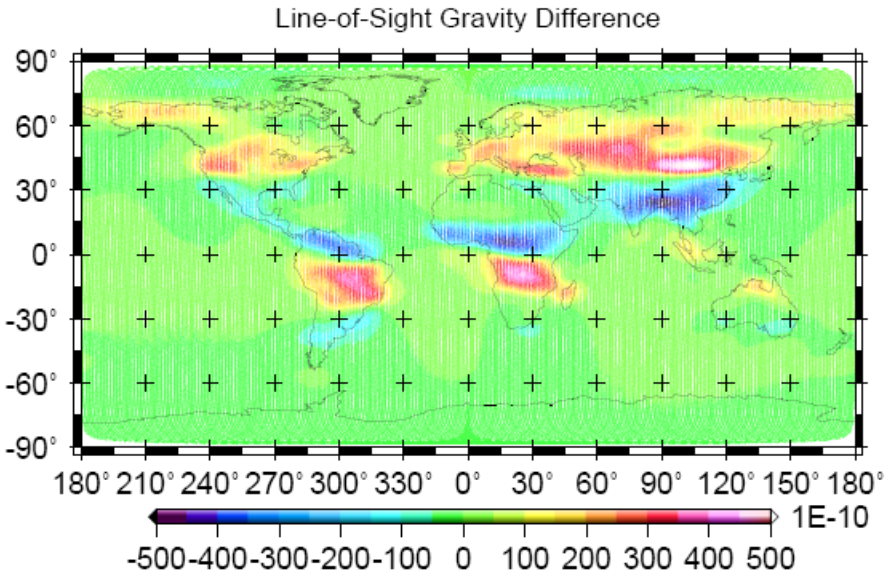

Figure 4.8: Simulated LOS gravity differences in July 2003

We use both the geopotential difference and the LOS gravity difference observations to recover the water storage change in the Amazon basin, globally and regionally. Figure 4.9 displays the time series of the raw data of water storage change in the Amazon basin. This figure is considered as “truth” (reality) and will be compared to all global and regional solutions. Also, from the time series of the water storage change in the Amazon area, annual and semi-annual signals are estimated together with a linear trend, and are shown in Figure 4.10.

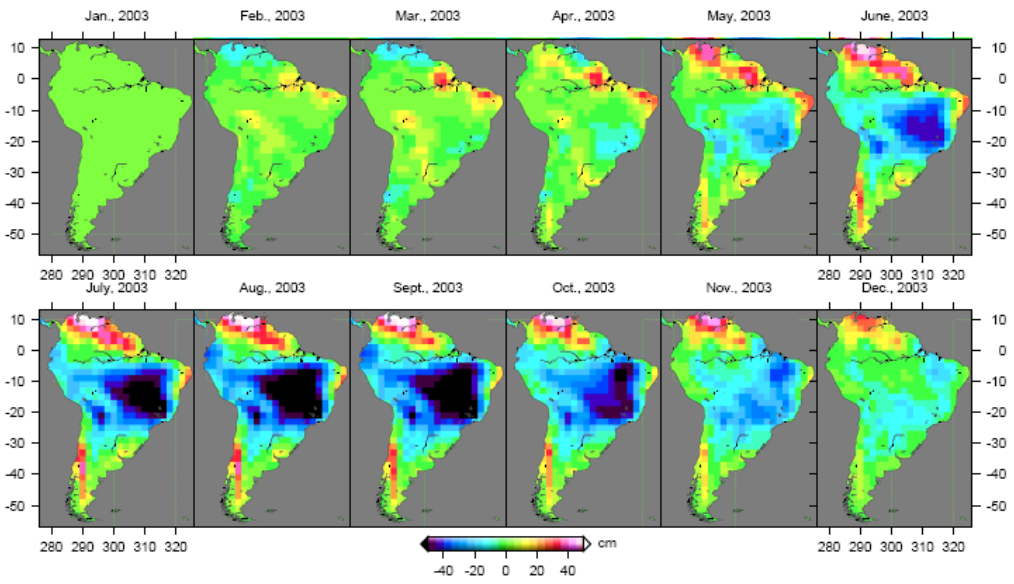

Figure 4.9: Terrestrial water storage change in the South America area ("truth")

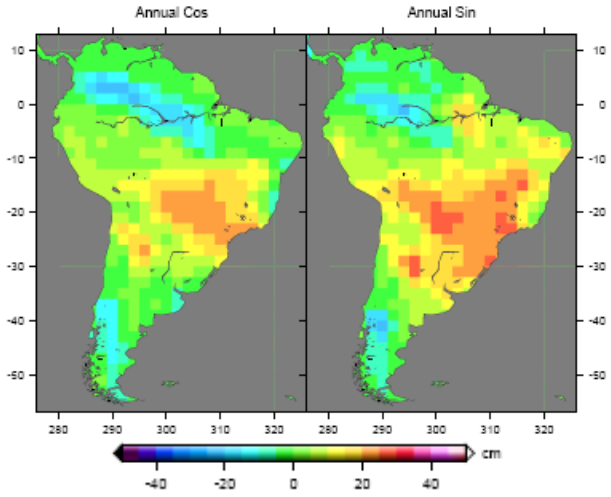

Figure 4.10: The cosine part and the sine part of the annual signal of the regional terrestrial water storage change

4.2.1. Global solutions

For each month from Jan. 2003 to Dec. 2003, we solve for the monthly global spherical harmonics coefficients, using the disturbing geopotential differences within each month. Then, for each monthly solution, we evaluate the water storage change, using (2.44) in Chapter 2. Figure 4.11 shows the results for the Amazon basin area. The obvious North-South "stripes" are geographically-correlated high frequency errors caused by inadequate observance (and system error) which results in ill-conditioning especially for downward continuation [Wahr et al., 2004; Swenson and Wahr, 2006]. Jekeli [1981] developed a Gaussian averaging function to compensate for poorly known short wave-length spherical harmonics coefficients, and this method was used at different filtering radii from 200 km to 600 km. Figure 4.12 shows the results after the Gaussian smoothing with a radius of 200 km; Figure 4.13 shows the results after the Gaussian smoothing with a radius of 400 km; Figure 4.14 shows the results after the Gaussian smoothing with a radius of 600 km. It is evident from the three figures that a radius of at least 400 km is necessary for stable results.

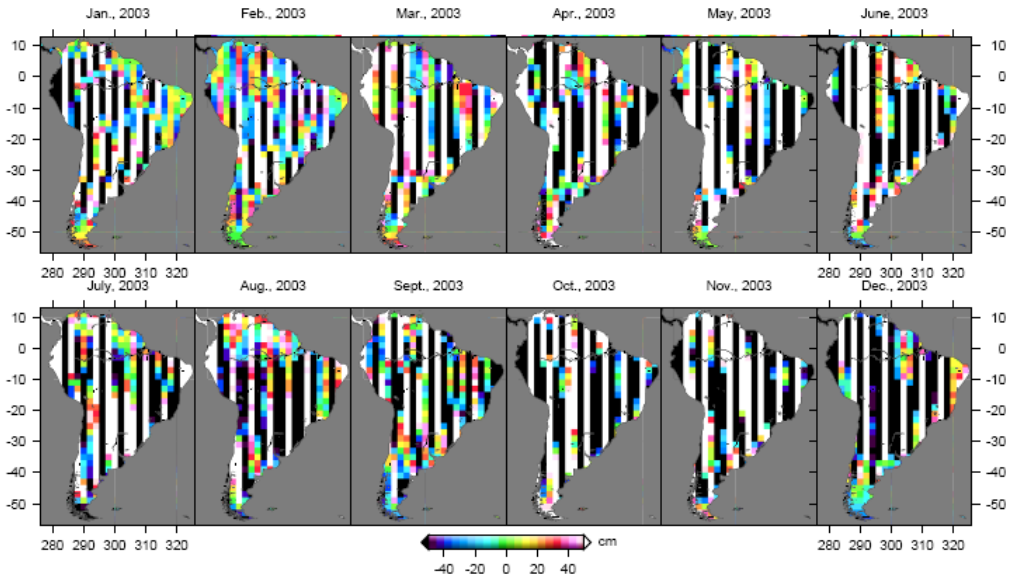

Figure 4.11: Global solutions (South America shown) from *in situ* geopotential differences (no smoothing)

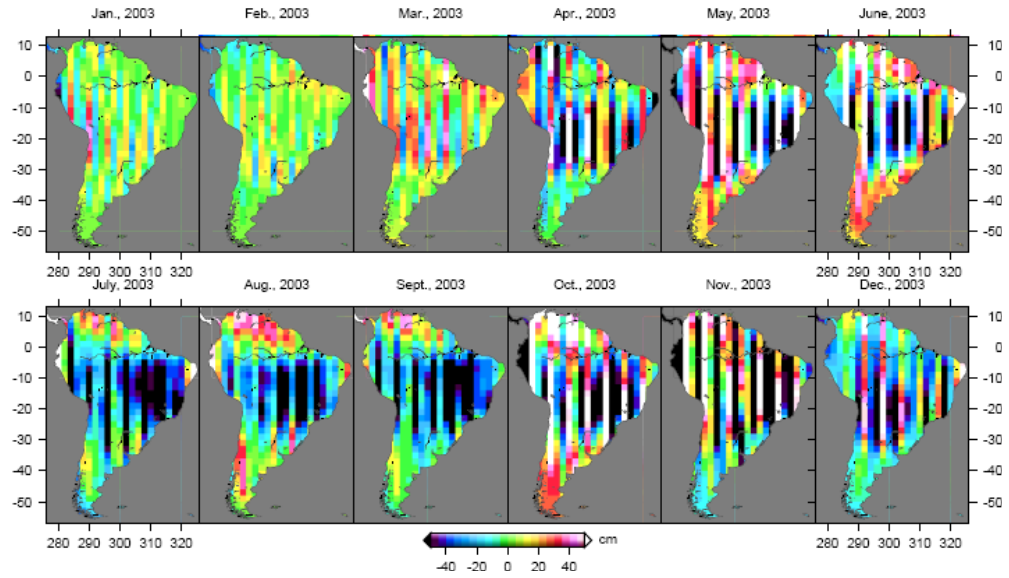

Figure 4.12: Global solutions (South America shown) from *in situ* geopotential differences (Gaussian smoothing with radius 200 km)

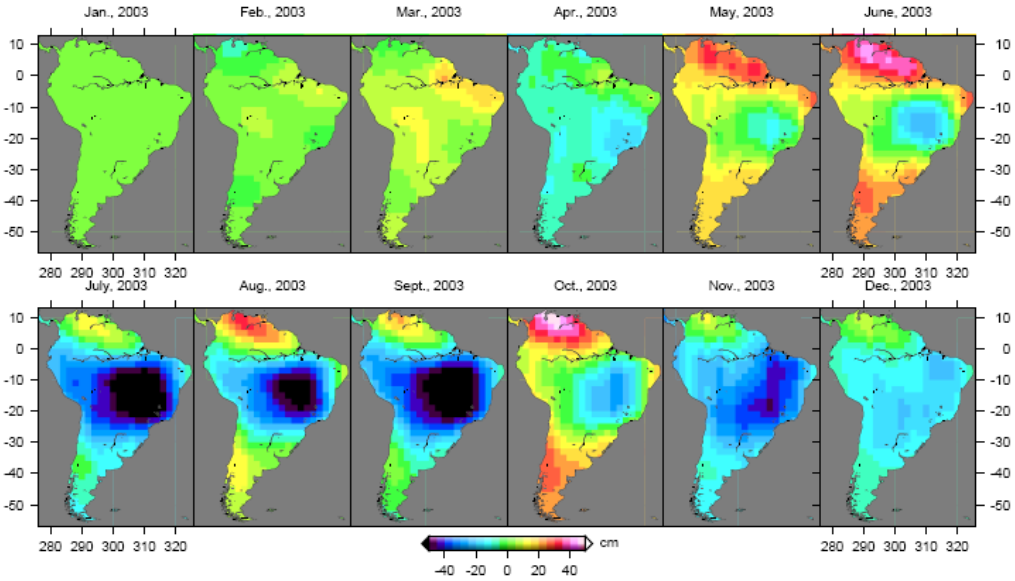

Figure 4.13: Global solutions (South America shown) from *in situ* geopotential differences (Gaussian smoothing with radius 400 km)

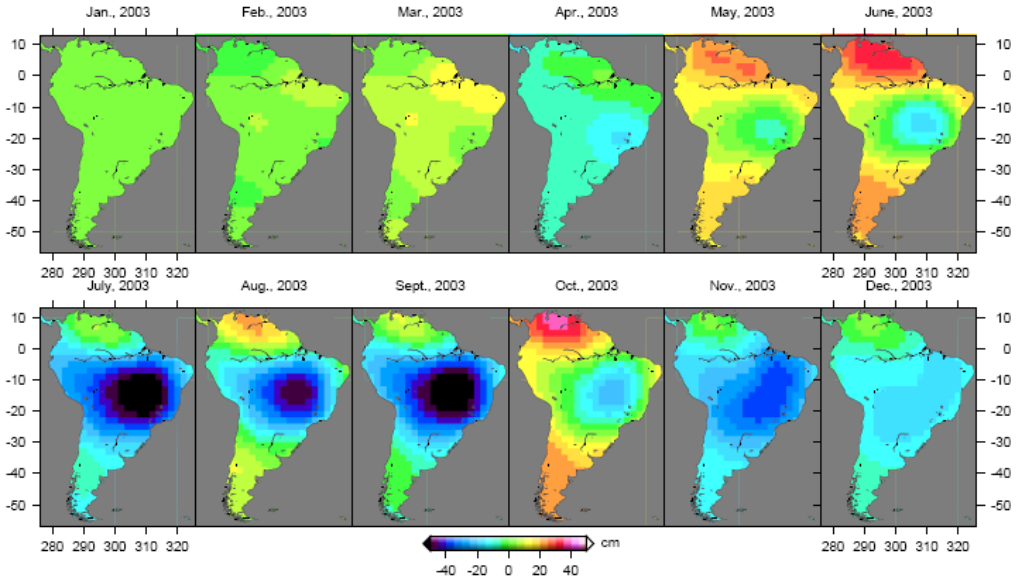

Figure 4.14: Global solutions (South America shown) from *in situ* geopotential differences (Gaussian smoothing with radius 600 km)

In the global inversion, we solve for spherical harmonics coefficients up to degree and order 90. The normal equations matrix to be inverted will be a very large matrix. However, to solve the large linear system of equations efficiently, we apply the conjugate gradient method which is among the most popular iterative methods. This method surely converges if the normal equations matrix is symmetric and positive-definite. The detailed procedure of the conjugate gradient method can be found in Ditmar and Klees, [2002], and Han [2003b]. Figure 4.15 (a) shows the degree variances (in cm for equivalent water thickness) after each iteration. The red line represents the degree variances after the first iteration, the green line denotes the degree variances after the second iteration and the black line represents the results after the 15th iteration. In order to illustrate the tiny differences between each consecutive iteration more clearly, we take the differences between them and, as shown in Figure 4.15 (b), the differences between the 14th and 15th iteration are at the order of 10^{-14} cm.

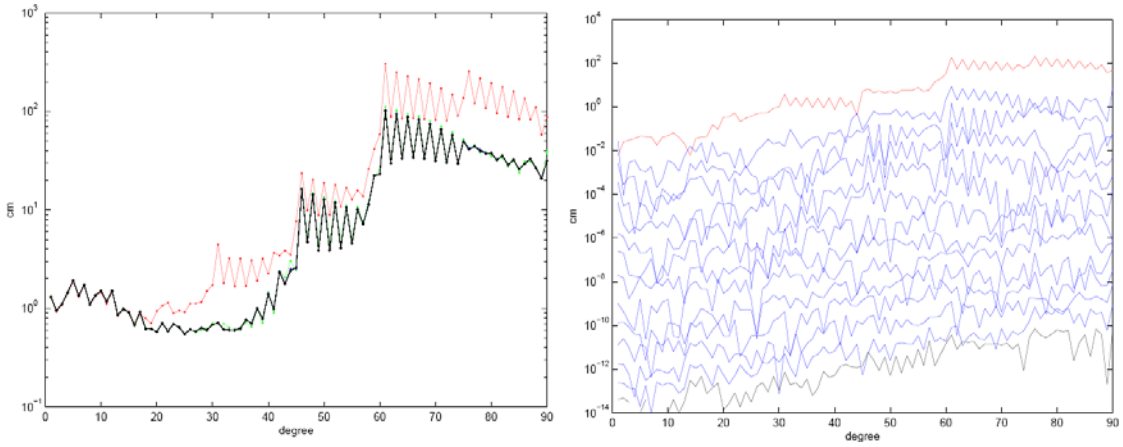

Figure 4.15: Degree variances (in the unit of equivalent water thickness, cm) for the coefficients estimated from disturbing geopotential differences, May, 2003. (a), left figure: red line represents the results after the first iteration, green line represents the results after the 2nd iteration, black line represents the results after the 15th iteration; (b), right figure: red line represents the differences between the results of the second iteration and the first iteration; black line represents the differences between the results of the 15th and the 14th iteration; blue line represents the differences for all the other consecutive iterations

4.2.2. Regional solutions

Based on equation (3.4) and the other corresponding formulas of Chapter 3.3 for solving the ill-conditioning problem, the regional water storage change using the simulated *in situ* geopotential differences is estimated over our study area, the Amazon basin area. Figures 4.16 through 4.18 show the three regional solutions from the three regularization methods described in Chapter 3.3. By comparing the solutions from the three different approaches, it is obvious that the solutions from iterative least-squares estimation with simultaneous updating of the a-priori covariance (Chapter 3.3.3) are stable and reliable. The solutions from an optimal regularization factor via formulas for the repro-BIQUUE of variance components (Chapter 3.3.2) agree well with the reality (Figure 4.9), too, except for March and April. The solutions from Bayesian inference with variance components have similar patterns as the "truth" (Figure 4.9); but there are noticeable high-frequency errors in each monthly solution. The power spectral density (PSD) values of all the twelve monthly regional solutions for each regularization method, except Bayesian inference with variance components, are computed and averaged to achieve a mean PSD for each method. The mean PSD values of the two regularizations corresponding to Figure 4.16 and Figure 4.18, respectively, are compared to each other and to the global solutions using the geopotential differences. As shown in Figure 4.19, the regularization method, based on an optimal regularization factor via formulas for the repro-BIQUUE of variance components, can achieve a solution with much higher frequency information than the

other method, iterative least-squares estimation with simultaneous updating of the a-priori covariance. Although the differences between the two regional solutions are small, both of the regional solutions perform much better than the global solutions when judged in terms of degree variances.

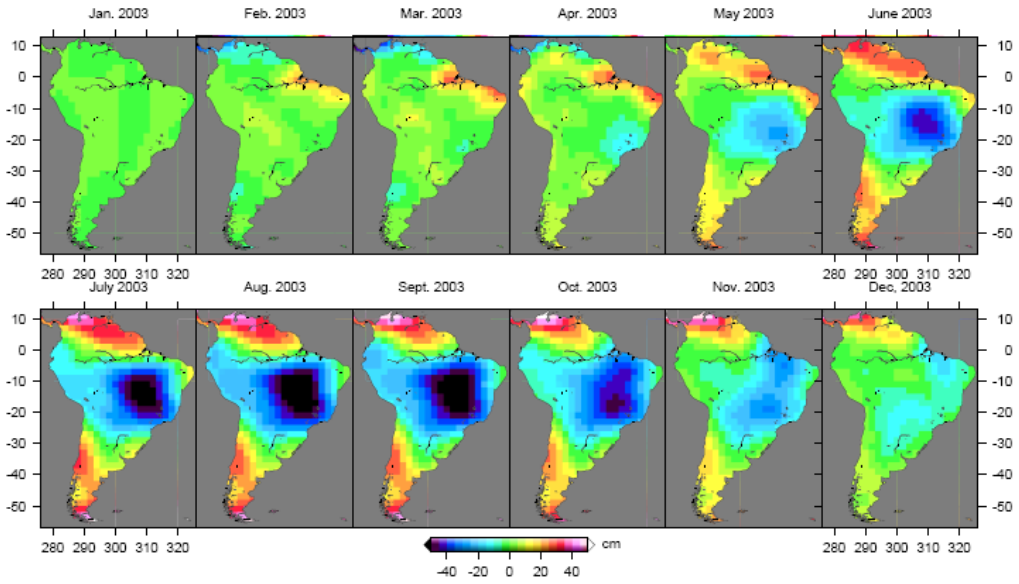

Figure 4.16: Regional solutions from *in situ* geopotential differences and iterative least-squares estimation with simultaneous updating of the a-priori covariance

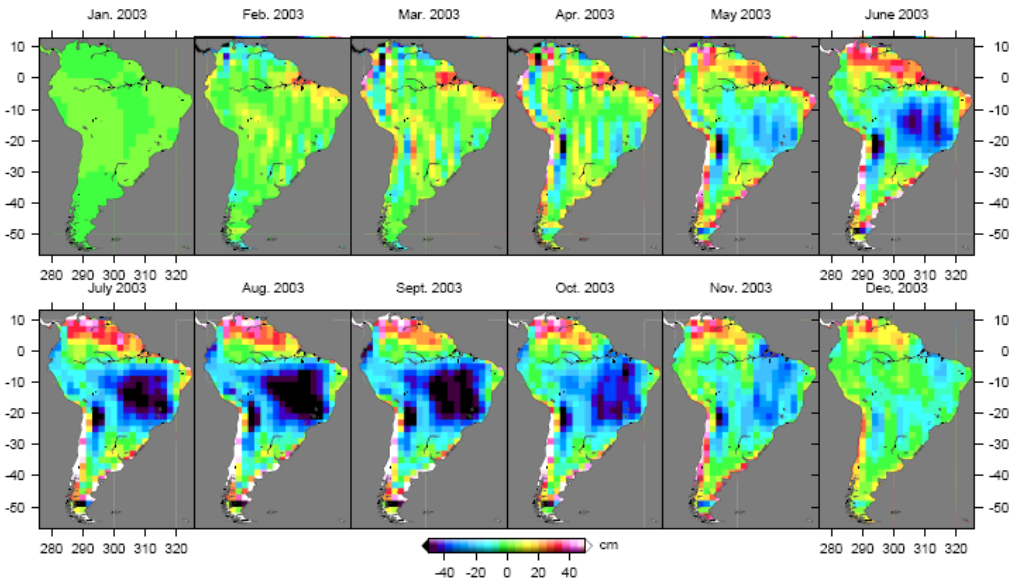

Figure 4.17: Regional solutions from *in situ* geopotential differences and Bayesian inference with variance components

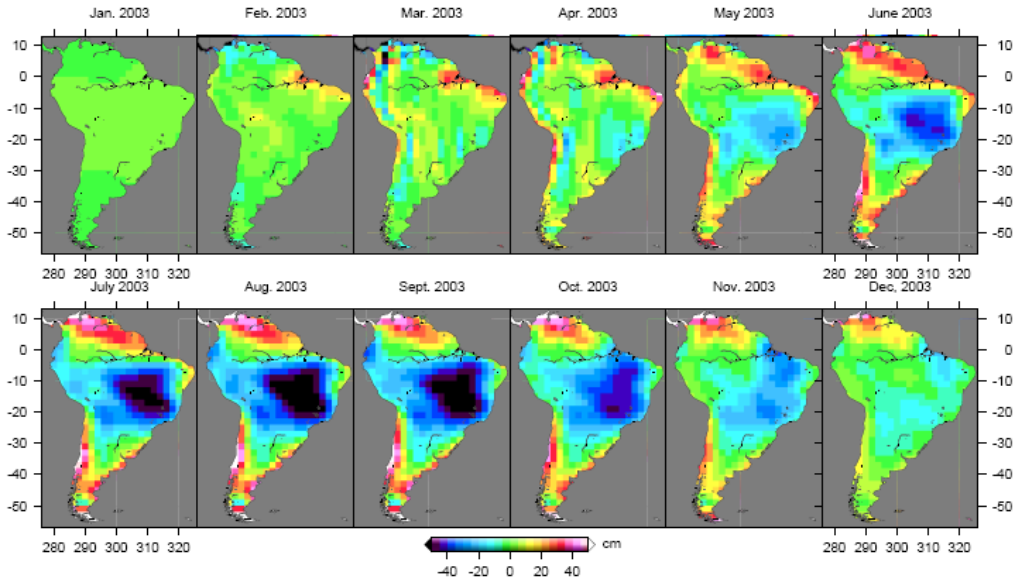

Figure 4.18: Regional solutions from *in situ* geopotential differences and an optimal regularization factor via formulas for the repro-BIQUUE of variance components

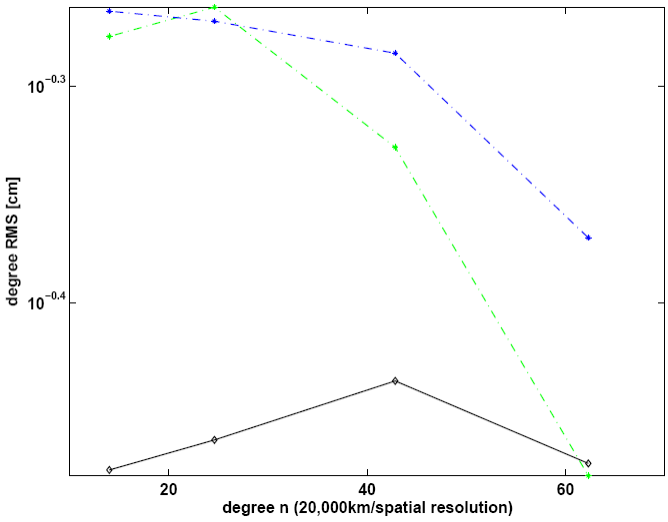

Figure 4.19: Square root of PSD of estimated water height change. The blue dashed line represents the results of an optimal regularization factor via formulas for the repro-BIQUUE of variance components corresponding to Figure 4.18; the green dashed line represents the results of iterative least-squares estimation with simultaneous updating of the a-priori covariance corresponding to Figure 4.16; the black solid line represents the global solutions using geopotential differences corresponding to Figure 4.14.

4.3. Global and regional solutions from *in situ* LOS gravity differences

4.3.1. Global solutions

Using the *in situ* LOS gravity differences within each month, we also solve for the monthly global spherical harmonics coefficients for each month in 2003. Then, for each monthly solution, we evaluate the water storage change using (2.44) in Chapter 2. The obvious North-South "stripes" exist, too, (see Figure 4.20) and we have to apply the Gaussian averaging function to smooth the global solutions. Figures 4.21 through 4.23 show the improved/smoothed solutions with different radii of 200 km, 400 km and 600 km. It may also be claimed that a stable solution can only be achieved by a Gaussian averaging function with a radius of at least 400 km.

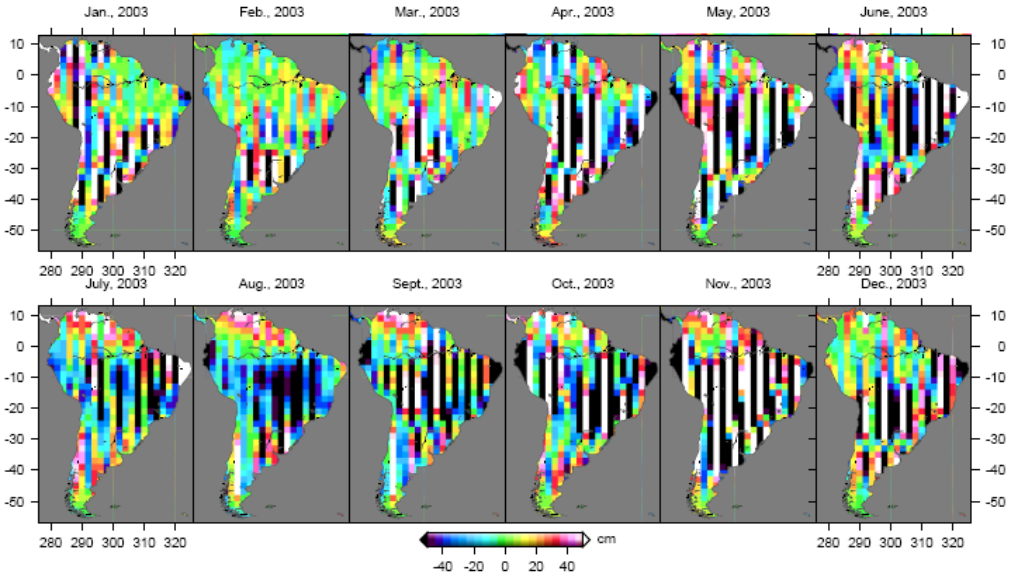

Figure 4.20: Global solutions (South America shown) from *in situ* LOS gravity differences (no smoothing)

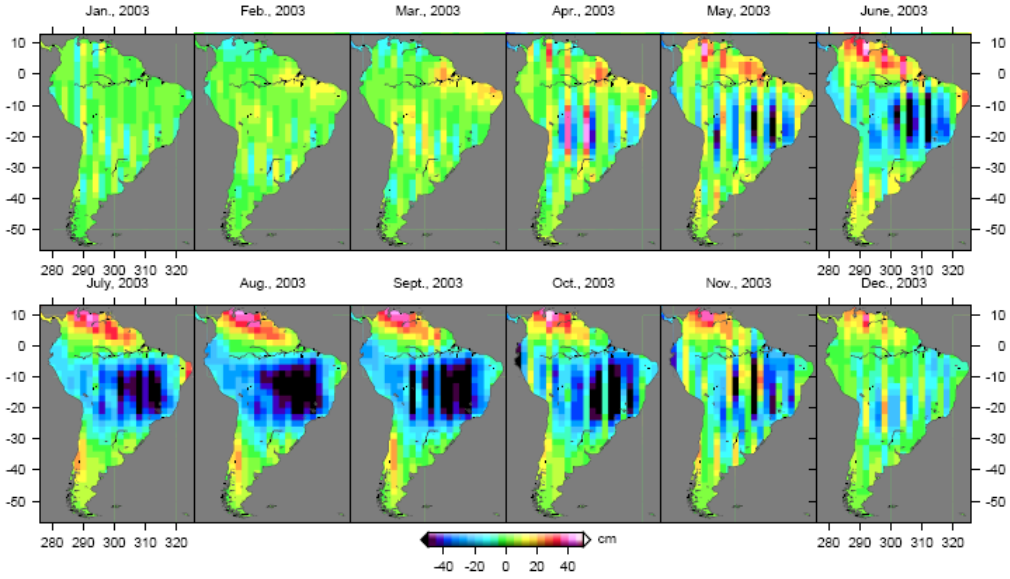

Figure 4.21: Global solutions (South America shown) from *in situ* LOS gravity differences (Gaussian smoothing with radius 200 km)

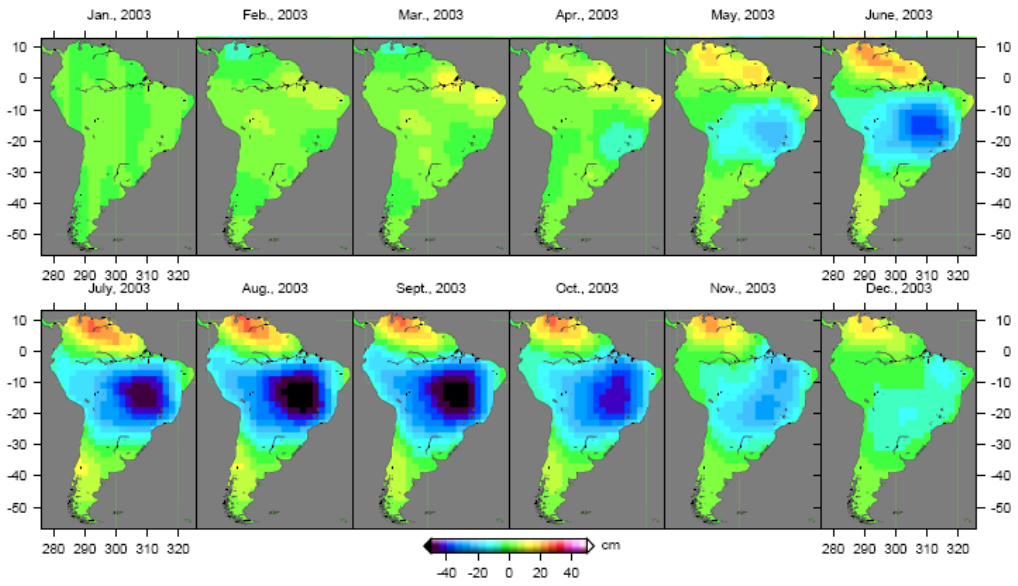

Figure 4.22: Global solutions (South America shown) from *in situ* LOS gravity differences (Gaussian smoothing with radius 400 km)

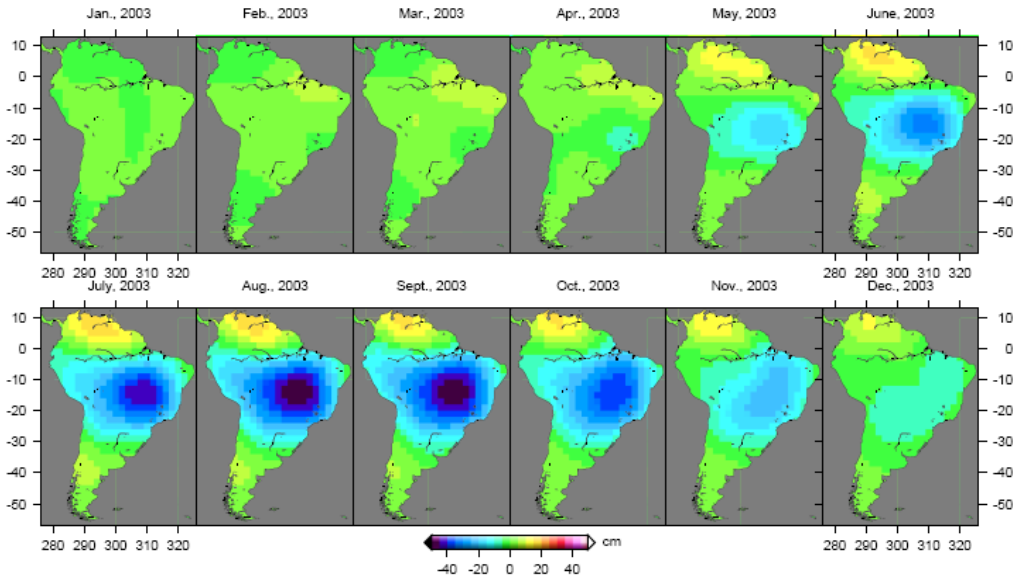

Figure 4.23: Global solutions (South America shown) from *in situ* LOS gravity differences (Gaussian smoothing with radius 600 km)

To compare the global solutions from using *in situ* LOS gravity differences with the global solutions from using *in situ* geopotential differences, we calculate their degree variances (in cm in equivalent water thickness), respectively. The red line in Figure 4.24 shows the degree RMS of the raw data from NECP/NCAR, the green line represents the degree variances of the global solutions using *in situ* geopotential differences and the blue line represents the degree variances of the global solutions using *in situ* LOS gravity differences. Both the green line and the blue line agree well with the red line at those low degrees, but above the degree 30 and the degree 40, the green line and the blue line jump away from the red line, respectively. This means that, while the global solutions using *in situ* geopotential differences are only reliable below degree 30 (corresponding to a spatial resolution of $6^\circ \times 6^\circ$ at the equator), the global solutions using *in situ* LOS gravity differences can achieve a resolution of degree 40 (corresponding to a spatial resolution of $4.5^\circ \times 4.5^\circ$ at the equator).

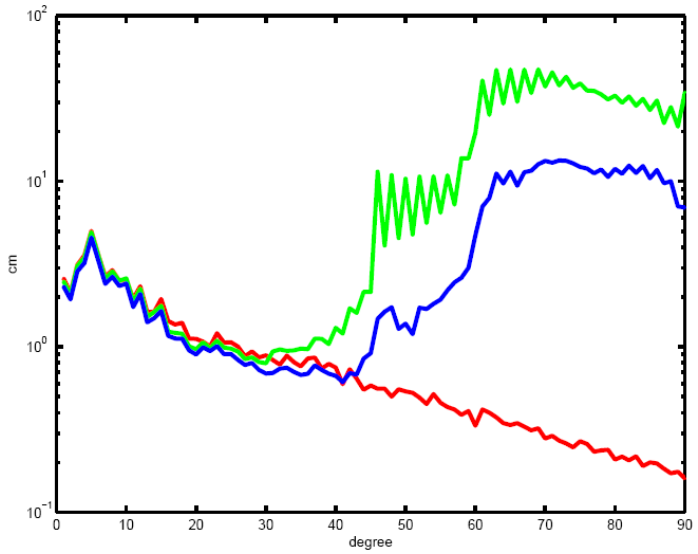

Figure 4.24: Degree variances of water storage changes in July 2003 (red); degree variances of estimated water storage changes in July 2003 from *in situ* geopotential differences (green); degree variances of estimated water storage changes in July 2003 from *in situ* LOS gravity differences (blue)

4.3.2. Regional solutions

Following the same procedure in Section 4.2.2, I also estimate regional solutions but using *in situ* LOS gravity differences. The results are different from the results of Section 4.3.1 above. First, the solutions from iterative least-squares estimation with simultaneous

updating of the a-priori covariance, are still the most stable and reliable solutions. Second, the approach, based on an optimal regulization factor via formulas for the repro-BIQUUE of variance components, achieves stable and reliable solutions, too. The solutions from Bayesian inference with variance components are still not smoothed enough for most of the months. Also, from Figure 4.28, the regularization method, based on an optimal regulization factor via formulas for the repro-BIQUUE of variance components, can achieve the highest frequency information, and both of the regional solutions perform much better than the global solutions.

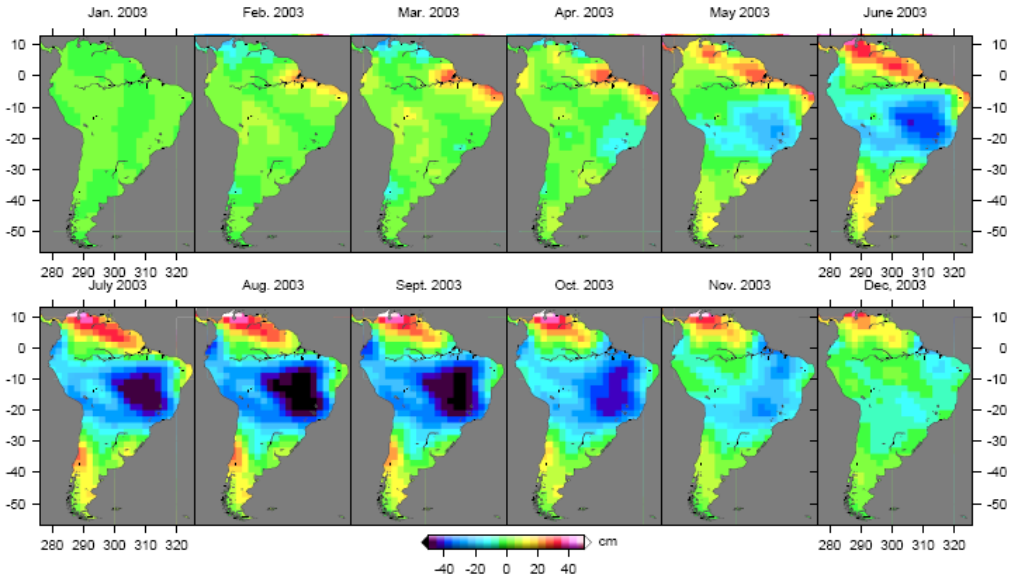

Figure 4.25: Regional solutions from *in situ* LOS gravity differences and iterative least-squares estimation with simultaneous updating of the a-priori covariance

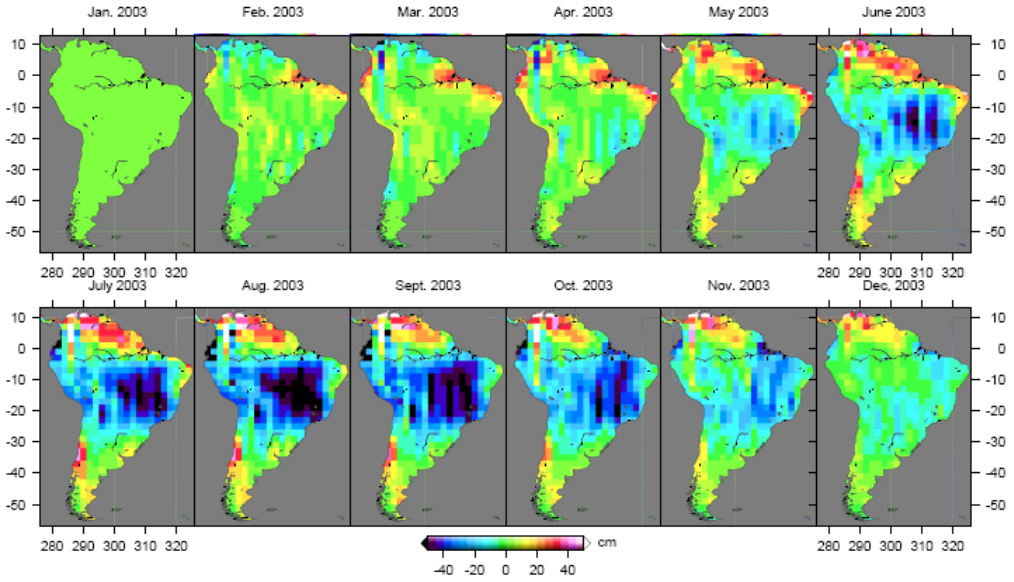

Figure 4.26: Regional solutions from *in situ* LOS gravity differences and Bayesian inference with variance components

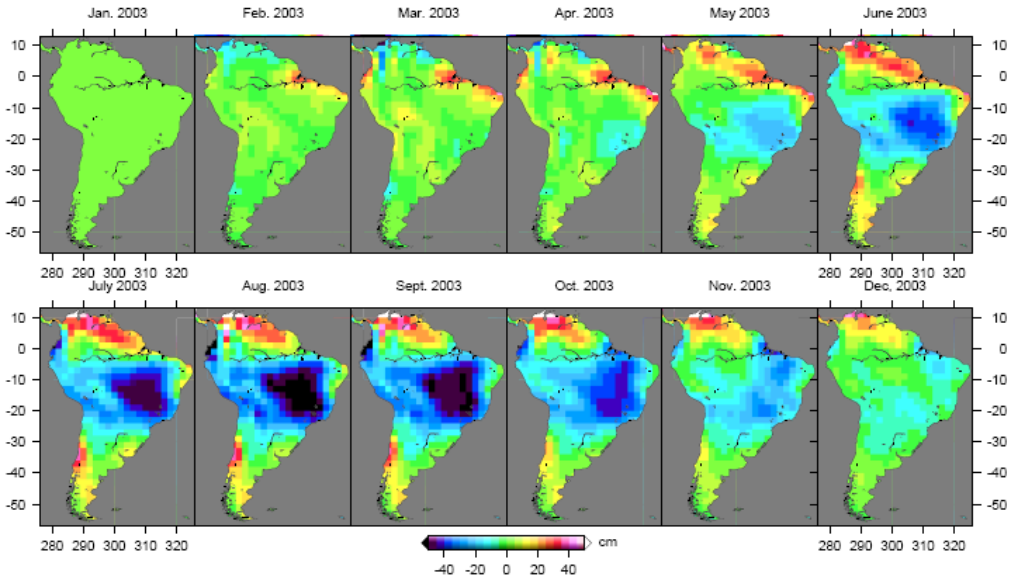

Figure 4.27: Regional solutions from *in situ* LOS gravity differences and an optimal regularization factor via formulas for the repro-BIQUUE of variance components

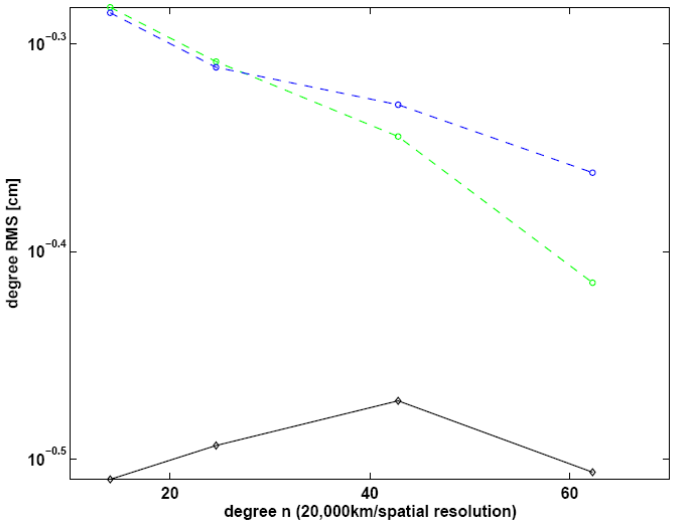

Figure 4.28: Square root of PSD of estimated water height change. The blue dashed line represents the results of an optimal regularization factor via formulas for the repro-BIQUUE of variance components corresponding to Figure 4.27. the green dashed line represents the results of iterative least-squares estimation with simultaneous updating of the a-priori covariance corresponding to Figure 4.25. the black solid line represents the global solutions using LOS gravity difference corresponding to Figure 4.22.

4.4. Effects of the modeling errors of the time-variable ocean tides and the atmosphere

In the real GRACE data processing, we must consider the short term mass variations in the atmosphere, because these time-varying effects cannot be eliminated by the repeated observations of the GRACE measurements [Han 2003b; Han et al., 2004]. Either the model from the European Center for Medium-range Weather Forecast (ECMWF) or the one from the National Centers for Environmental Prediction (NCEP) can be used to correct the short term mass variations of the atmosphere. To analyze the effects of the modeling error of the short term mass variations of the atmosphere on the recovery of continental water storage change, I simply take the difference between these two models as an indicator for any modeling error. The other large systematic effect comes from the ocean tides, which can be either corrected by the model CSR4.0 [Eanes and Bettadpur, 1995] or by the model NAO99 [Matsumoto et al., 2000]. I also take the difference between these two models, and analyze the effects of the modeling error of the ocean tides on the recovery of the continental water storage change, but shall consider just four components, namely, K_1, O_1 , M_2 and S_2.

The global atmospheric pressure data are available from both ECMWF and NCEP, and the pressure data, p_s, can be converted into equivalent water thickness or height by the following relationship,

$$h(\lambda,\theta,t) = \frac{p_s(\lambda,\theta,t)}{g\rho_w}, \tag{4.1}$$

where $h(\lambda,\theta,t)$ is the equivalent water height, i.e., the expression of the atmosphere pressure in terms of water height. g is the nominal gravity value, ρ_w is the density of water. λ, θ are the longitude and latitude of the surface pressure data point, and t is the time.

We choose to use spherical surface functions to represent a global grid of $h(\lambda,\theta,t)$ at a certain time epoch t, by using a quadrature to calculate the corresponding spherical surface coefficients,

$$\begin{Bmatrix} \Delta\overline{C}_{lm}(t) \\ \Delta\overline{S}_{lm}(t) \end{Bmatrix} = \frac{3(1+k_l)\rho_w}{4\pi R\rho_E(2l+1)} \int_0^{2\pi} d\phi \int_0^{\pi} \sin\theta d\theta \cdot h(\lambda,\theta,t)\overline{P}_{lm}(\cos\theta) \begin{Bmatrix} \cos(m\lambda) \\ \sin(m\lambda) \end{Bmatrix}, \tag{4.2}$$

where $\Delta\overline{C}_{lm}(t)$ and $\Delta\overline{S}_{lm}(t)$ are the spherical surface coefficients of the time-varying surface mass change, k_l is the Love number, ρ_E is the mean density of the Earth.

Both ECMWF and NCEP provide gridded surface pressure data every 6 hours, so that we use (4.2) to calculate the corresponding spherical surface coefficients using the differences of the equivalent water height between the two models every 6 hours in a day. These calculated coefficients will be used to calculate increments for the geopotential differences and the LOS gravity differences between the two satellites, considered as the system errors coming from the non-perfect modeling of the atmosphere; then, they are added to the previously simulated *in situ* geopotential differences and the simulated *in situ* LOS gravity differences, respectively. Figure 4.29 shows the time-varying atmospheric model errors along the GRACE orbit for July 2003 in terms of *in situ* geopotential differences. By comparing Figure 4.29 with Figure 4.7, it is clear that overall the effects of the modeling error of the atmosphere are one order smaller than the signals of terrestrial water storage change, and especially smaller on the continents. However, for the Antarctic area, the effects of the modeling error are very big, which can be contributed to the poor observations in the Antarctica area. The conclusions hold true when we are comparing the effects of the modeling error of the atmosphere with the original signals of the terrestrial water storage in terms of the *in situ* LOS gravity differences, as shown in Figure 4.30.

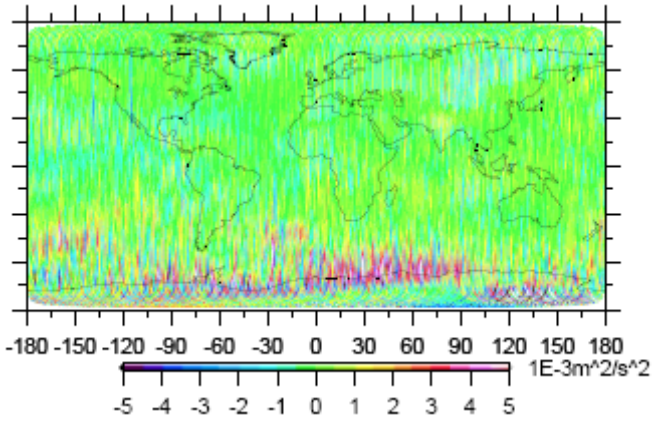

Figure 4.29: Time-varying atmospheric model error along the GRACE orbits for July 2003 in terms of *in situ* geopotential differences

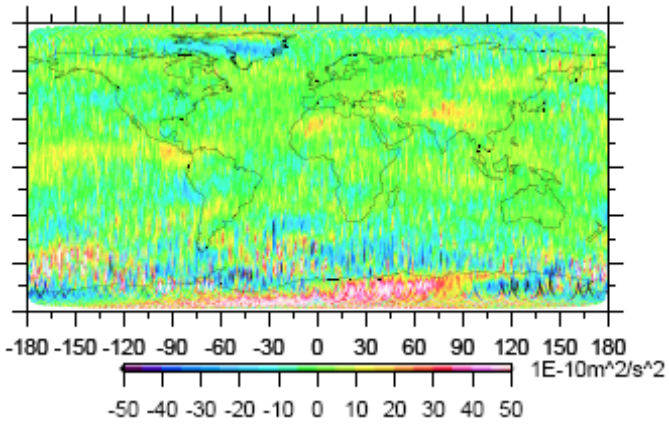

Figure 4.30: Time-varying atmospheric model error along the GRACE orbits for July 2003 in terms of *in situ* LOS gravity differences

The effects of the ocean tidal error in terms of both the geopotential differences and the LOS gravity differences are computed, and then added to the simulated *in situ* geopotential differences and the simulated *in situ* LOS gravity differences, respectively. First, the time-variable ocean tide is decomposed into temporal sine and cosine components, and each component is expanded into spherical surface coefficients so that each tidal constituent consists of four sets of coefficients, $\overline{C}_{nm}^{C}$ and $\overline{S}_{nm}^{C}$ for the cosine component, $\overline{C}_{nm}^{S}$ and $\overline{S}_{nm}^{S}$ for the sine components. The gravitional potential at satellite altitude generated by a particular ocean tidal constituent with frequency, ω, and initial phase, φ^{0}, is given by [Han, 2003b]:

$$V(r,\theta,\lambda;t) = \frac{GM}{R}\sum_{n=0}^{\infty}\sum_{m=0}^{n}\left(\frac{R}{r}\right)^{n+1}\overline{P}_{nm}(\cos\theta)\left(\overline{C}_{nm}(t)\cdot\cos m\lambda + \overline{S}_{nm}(t)\cdot\sin m\lambda\right), \quad (4.3)$$

where, $\overline{C}_{nm}(t) = \overline{C}_{nm}^{C}\cos(\omega t + \varphi^0) + \overline{C}_{nm}^{S}\sin(\omega t + \varphi^0)$, and

$\overline{S}_{nm}(t) = \overline{S}_{nm}^{C}\cos(\omega t + \varphi^0) + \overline{S}_{nm}^{S}\sin(\omega t + \varphi^0)$.

Similarly, we can also calculate the LOS gravity differences generated by a particular ocean tidal constituent, after $\overline{C}_{nm}(t)$ and $\overline{S}_{nm}(t)$ have been calculated, with a little modifications to the formulas (2.21) through (2.23).

Figure 4.31 shows the geopotential differences generated by the constituents K_1, O_1, M_2 and S_2. In general, the effects of the ocean tidal modeling error are one order smaller than the signals from the terrestrial water storage change. One point to mention is that the effects of the modeling error of S_2 can hardly be eliminated in a monthly solution because the aliasing period of S_2 is 182.5 solar days, while the other constituents K_1, O_1 and M_2 have their aliasing periods as 23.94 hours, 25.82 hours and 13.7 days [Han, 2003b]. Figure 4.32 shows the LOS gravity differences generated by the same constituents, and the order of the effects of ocean tidal error are one order smaller than the signals from the continental water storage change, too.

We consider their effects on the *in situ* geopotential differences and the *in situ* LOS gravity differences, and solve for regional solutions again. Only the results after applying the iterative least-squares estimation with simultaneous updating of the a-priori covariance are presented and shown in Figure 4.33 and Figure 4.34. By comparing these two figures with Figures 4.16 and 4.25, it can be concluded that the recovery of terrestrial water storage change is not affected significantly by the modeling errors of the atmosphere and the ocean tides. Of course, this is based on the assumption that the differences of the two different models reflect the modeling errors properly, for either the atmosphere pressure or ocean tides.

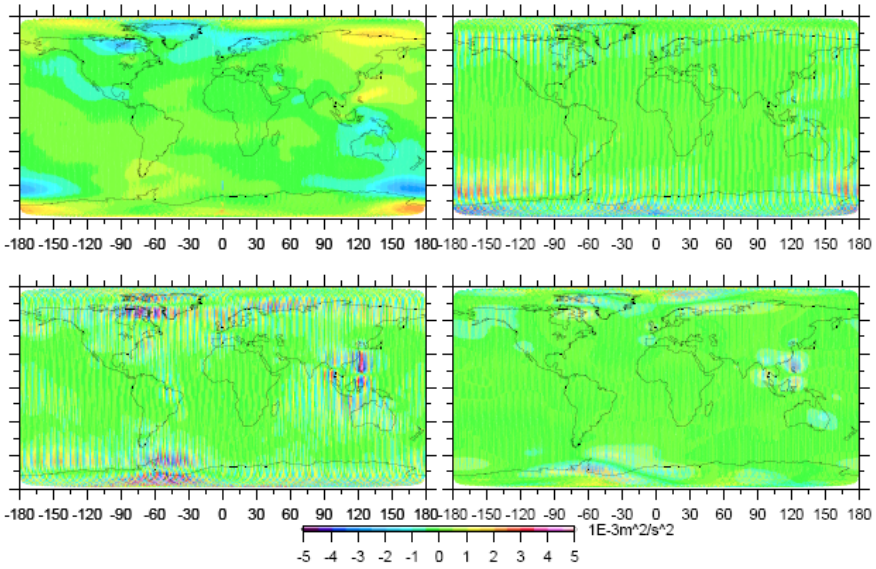

Figure 4.31: Time-varying tidal model errors computed along the GRACE orbits for July 2003 in terms of *in situ* geopotential differences. (a) K_1, top left; (b), O_1, top right; (c), M_2 bottom left; (d) S_2, bottom right

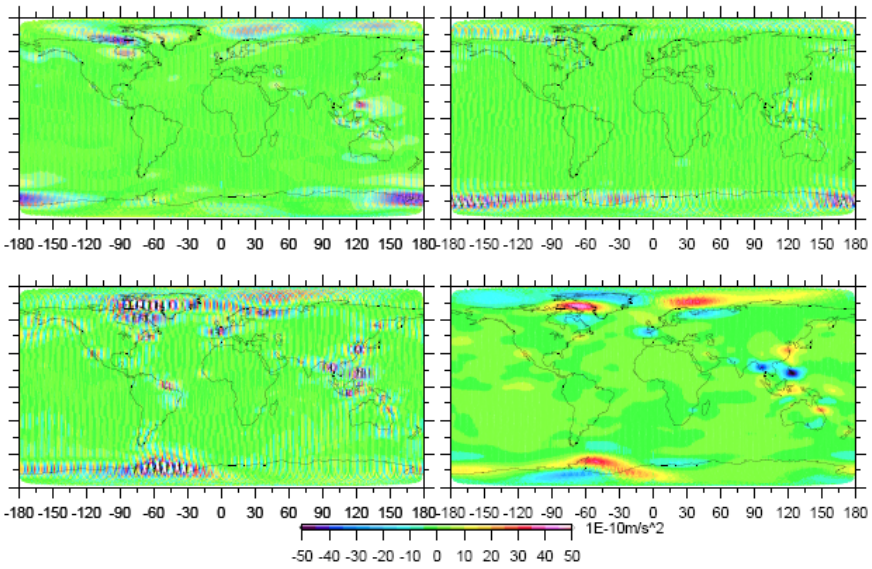

Figure 4.32: Time-varying tidal model errors computed along the GRACE orbits for July 2003 in terms of *in situ* LOS gravity differences. (a) K_1, top left; (b), O_1, top right; (c), M_2 bottom left; (d) S_2, bottom right

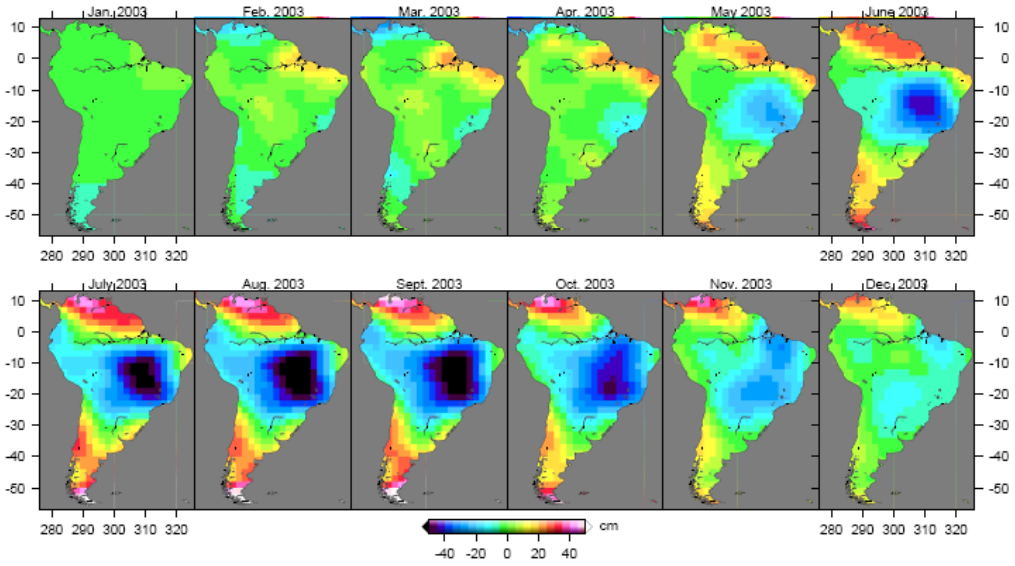

Figure 4.33: Regional solutions from *in situ* geopotential differences and iterative least-squares estimation with simultaneous updating of the a-priori covariance

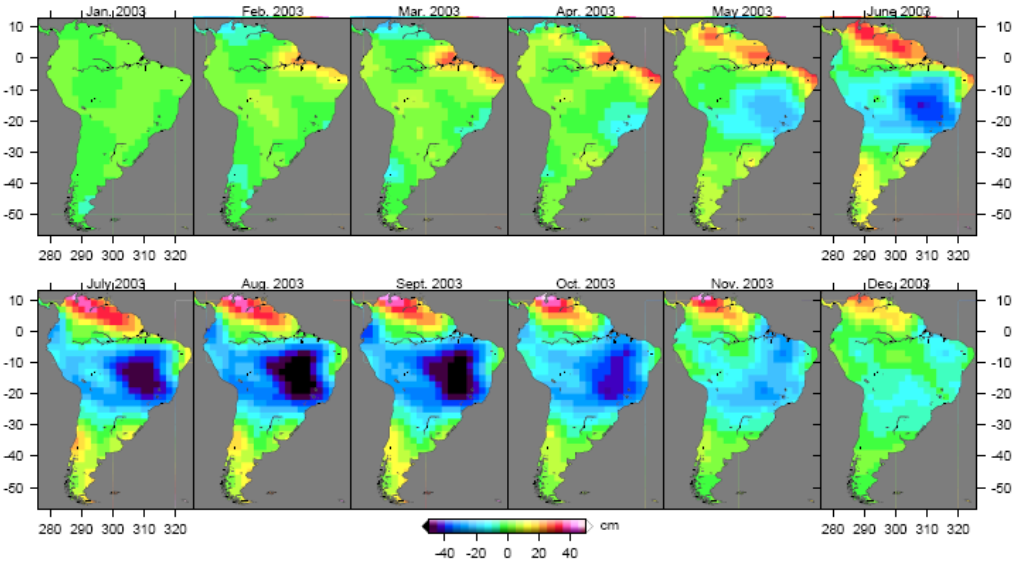

Figure 4.34: Regional solutions from *in situ* LOS gravity differences and iterative least-squares estimation with simultaneous updating of the a-priori covariance

CHAPTER 5

RECOVERY OF TERRESTRIAL WATER STORAGE CHANGE GLOBALLY AND REGIONALLY

5.1. Introduction to GRACE data

The data from the GRACE mission include the inter-satellite range change measurements, as well as the accelerometer, GPS and attitude measurements from each satellite.

The GRACE products are developed, processed and archived in a joint Science Data System (SDS) between the Jet Propulsion Laboratory (JPL), the University of Texas Center for Space Research (UTCSR), and the GeoForschungsZentrum Potsdam (GFZ). Figure 5.1 shows the GRACE mission data flow.

The GRACE data are divided into four different levels: the Level-0 (L0), the Level-1A (L1A), the Level-1B (L1B), and the Level-2 (L2). The L0 data are the raw data, consisting of raw, unprocessed telemetry data that have been decommutated by Deutsches Zentrum für Luft- und Raumfahrt (DLR) and the German Remote Sensing Data Center (DFD). The L0 data are calibrated and time-tagged in a non-destructive sense, and then labeled Level-1A (L1A). L1A data products are not distributed to the public. These data undergo extensive and irreversible processing, and are converted to edited data products at 5 second sampling [Wu et al., 2004]. The products labeled L1B include, among others, the inter-satellite range, range-rate, range-acceleration, the non-gravitational accelerations on each satellite, the orientation estimates, the orbits, etc. The L1B products are processed to produce the monthly gravity field estimates in form of spherical harmonics coefficients. Occasionally, several months of data are combined to produce an estimate of the mean or static gravity field. These estimates are labeled L2. After validation, all L2 and accompanying L1B products are released to the public through two portals. One data center is the Physical Oceanography Distributed Active Archive Center (PO.DAAC) at the Jet Propulsion Laboratory, Pasadena, USA. The other is the Information System & Data Center (ISDC) at the GeoForschungsZentrum Potsdam in Germany. The monthly estimates are only distributed through the PO.DAAC or ISDC websites. Table 5.1, Table 5.2 and Table 5.3 show the components of the L1A products, L1B products and L2 products.

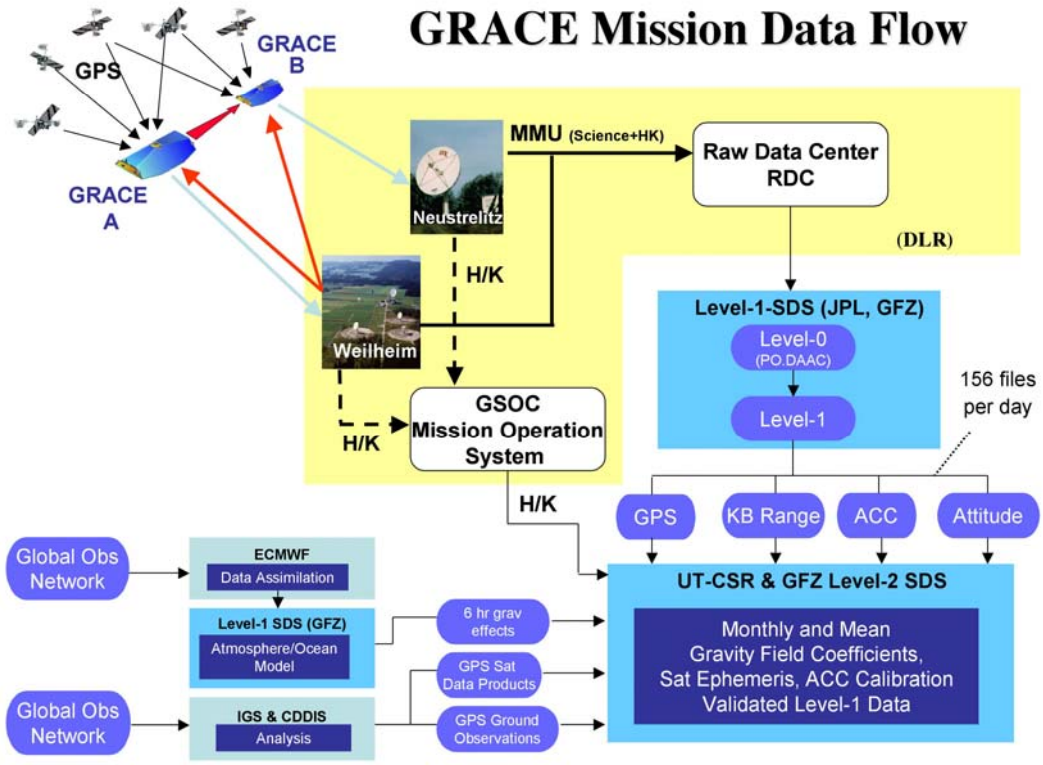

Figure 5.1: GRACE mission data flow (http://www.csr.utexas.edu/grace/asdp.html)

Measurements	Product	Sample rate
K-Band Ranging	K and Ka frequency integrated carrier phase	10 Hz
GPS RO-Measurements	SNR & phase	50 Hz
GPS Orbit Data	SNR & phase	1 – 10 Hz
Acceleration	Linear & angular accelerations	10 Hz
SCA Quaternions	Orientation of SCA axes relative to inertial frame	0.2 - 2 Hz

Table 5.1: Level-1A products

Measurements	Product	Sample rate
K-Band Ranging	Biased range & derivatives	0.2 Hz
Laser Ranges to Satellite	Ground site-GRACE distance	0.2 Hz
Satellite Position & Velocity	Cartesian	0.2 Hz
Acceleration	Non-gravitational linear accelerations	0.2 Hz
Spacecraft Attitude	S/C and ACC attitude	0.2 Hz

Table 5.2: Level-1B products

Measurement	Product	Sample interval
Geopotential Field	Spherical harmonic coefficients	30 days or longer
Satellite Position & Velocity	Cartesian	5 s

Table 5.3: Level-2 products

By using the GRACE L2 products, it is possible to globally detect the continental water storage change at a certain resolution from the GRACE mission. Wahr et al. [1998], first connected changes in the coefficients of the gravity field to changes in surface mass density, by expressing changes in surface mass in equivalent water thickness. Rodell and Famiglietti [1999] tested 20 drainage basins, ranging in size from 130,000 km^2 to 5782,000 km^2, and used estimates of uncertainty in the GRACE technique to determine in which basins water storage changes may be detectible by GRACE and how that detectibility may vary in space and time. Rodell and Famiglietti [2001] enhanced their study based on observations of groundwater and surface water variations as well as snow and soil water variations, rather than on models. Tapley et al. [2004b] showed the month-to-month geoid variability for South America during 2003, claiming that for the Amazon basin, which is worldwide the largest drainage basin (>5 million km^2), a local maximum of 14.0 mm relative to the mean was observed in April 2003, and a local minimum of -7.7 mm was observed in October 2003.

KBR range-rate and range-acceleration measurements, the GRACE L1B data, can be used to regionally recover the continental water storage changes. Han et al. [2005b] studied the estimation of continental water storage regionally, instead of globally, and claimed that higher frequency information of the continental water storage has been

acquired by fully exploiting the high accuracy of the KBR range rate ($\pm\ 0.1\mu m/\sec$). Mayer-Gürr et al. [2005a,b] used a combination of range, range rate, and range acceleration after decorrelation and achieved a new spherical harmonics model, ITG-GRACE01s, which is comparable to the solutions of both GFZ and CSR, with the advantage of no accumulated force effects and of low computational costs.

In this chapter, both the *in situ* geopotential observations and the *in situ* LOS gravity difference observations are used to estimate continental water storage change regionally by applying the different regularization approaches described in Chapter 3.3; the results will be compared to each other, and to the global solutions.

5.2. Transformations and perturbations in GRACE data processing

The primary GRACE L1B data I used are the KBR inter-satellite range rates and range accelerations with a sampling rate of $5\ s$, and a precision of $\pm 0.1\ \mu m/s$ for range rate and a precision of $\pm 0.1\ \mu gal$ (Kim [2000]) for range acceleration. Precise absolute orbits for the GRACE satellites [S. Bettadpur, Center for Space Research (CSR), personal communication, D. Yuan, Jet Propulsion Laboratory (JPL), personal communication, and S. Zhu, GFZ, personal communication] are provided with a sampling rate of $5\ s$ and an estimated accuracy of $\pm 2\ cm$ for the position error. The background models for the precise orbit determination (POD) are described in the GRACE L2 Handbook [Bettadpur, 2006]. For example, the GGM01C [Tapley et al., 2004a] geopotential model was used for the background gravitational force model. The accelerometer data have a sampling rate of $1\ s$ and a claimed precision of $\pm 10^{-2}\ \mu gal$, and the star sensor data have a sampling rate of $5\ s$ and a precision of about $\pm 100\ \mu rad$.

5.2.1. Transformation of time systems

In this section I just simply introduce the transformation between the GPS time (used in GRACE data processing) and the Terrestrial Dynamic Time (TDT). For other time systems such as the Universal Time or the Sidereal Time, please refer to Seeber [2003]. The primary time system used in the GRACE data processing is the GPS time t_{GPS}. It is connected to the International Atomic Time (TAI) by a constant offset:

$$TAI = t_{GPS} + 19s\,. \tag{5.1}$$

The difference between TDT and TAI is

$$TDT = TAI + 32.184s\,. \tag{5.2}$$

So, the difference between TDT and t_{GPS} is

$$TDT = t_{GPS} + 51.184s\,. \tag{5.3}$$

The time tags of all GRACE observations, t_{GPS}^{GRACE}, are seconds in GPS time past 12:00:00, Jan. 01, 2000 [Bettadpur 2003]; so, whenever we are transforming t_{GPS}^{GRACE} to TDT, we must consider the constant difference between the origin of GPS time (0:00:00, Jan.06, 1980) and the origin of GRACE GPS time (12:00:00, Jan. 01, 2000), which, in the unit of Julian days equals 2451545.0.

5.2.2. Transformation between inertial and Earth-Centered-Earth-Fixed frames

The Earth-Centered-Earth-Fixed (ECEF) reference frame is necessary for associating observations and models to the geodetic locations; the inertial reference frame is necessary for dynamics, integration and ephemerides. The transformation matrix C_e^i at epoch t between the inertial and the ECEF reference frame is implemented as:

$$C_e^i = P(t)N(t)R(t)W(t), \tag{5.4}$$

where P, N, R and W are the rotation matrices arising from the precession, nutation, earth rotation and the polar motion, respectively. In Chapter 5 of IERS Conventions (2003) [McCarthy and Petit, 2004], a procedure in detail is dedicated to describe the transformation between the inertial frame and the ECEF frame, and all necessary codes in Fortran are provided on the IERS Conventions web page.

W accounts for the polar motion and is implemented as

$$W = R_1(y_p)R_2(x_p), \tag{5.5}$$

where (x_p, y_p) are the pole motion as tabulated by the International Earth Rotation and Reference Systems Service (IERS). R is the sidereal rotation and is implemented as

$$R = R_3(-GMST + corrections), \tag{5.6}$$

where the Greenwich Mean Sidereal Time (GMST) and the corrections are calculated according to IERS Conventions, 2003. P and N are precession and nutation, respectively, and are estimated and provided by IERS as well.

5.2.3. Satellite attitude

The inertial orientation of the GRACE satellite is modeled using tabular input data quaternions. The same data are used for rotating the accelerometer data to the inertial frame. At epochs when the GRACE quaternion product is not available, linear interpolation between adjacent values is used.

The attitude measurements obtained by the star sensor are given in the form of quaternions as follows: $q_1 = e_x \cdot \sin\frac{\delta}{2}$, $q_2 = e_y \cdot \sin\frac{\delta}{2}$, $q_3 = e_z \cdot \sin\frac{\delta}{2}$, $q_4 = \cos\frac{\delta}{2}$, where e_x, e_y and e_z are the direction cosines of the rotation axis and δ is the rotation angle. Since q_1, q_2, q_3 and q_4 are given in the i-frame, the matrix

$$C_s^i = \begin{pmatrix} q_4^2 + q_1^2 - q_2^2 - q_3^2 & 2(q_1 q_2 + q_3 q_4) & 2(q_1 q_3 - q_2 q_4) \\ 2(q_1 q_2 - q_3 q_4) & q_4^2 + q_2^2 - q_1^2 - q_3^2 & 2(q_2 q_3 + q_4 q_1) \\ 2(q_1 q_3 + q_2 q_4) & 2(q_2 q_3 - q_4 q_1) & q_4^2 + q_3^2 - q_1^2 - q_2^2 \end{pmatrix} \tag{5.7}$$

transforms a vector from the spacecraft frame to the inertial frame.

5.2.4. N-body perturbations

Assuming that the Sun and the Moon can be considered to be point-masses, as is the satellite, the perturbing acceleration, caused by the gravitational influence of the perturbing body j, is

$$\ddot{\mathbf{r}}_j = Gm_j\left(\frac{\mathbf{r}_j - \mathbf{r}}{(|\mathbf{r}_j| - |\mathbf{r}|)^3} - \frac{\mathbf{r}_j}{|\mathbf{r}_j|^3}\right), \tag{5.8}$$

where G is the gravitational constant and m_j the mass of the respective disturbing body. The geocentric vectors $\mathbf{r}_j$ and $\mathbf{r}$ point to the disturbing body j and the satellite, respectively.

To calculate the perturbing potential V_j arising from the disturbing body j, we use the harmonic development of the tide generating potential and neglect the items higher than order 2,

$$V_j = Gm_j \frac{|\mathbf{r}|^2}{|\mathbf{r}_j|^3}\left(\left(\frac{1}{2}\left(3\cos^2\theta_j\right) - 1\right) + \frac{|\mathbf{r}|}{|\mathbf{r}_j|}\left(\frac{1}{2}\left(5\cos^3\theta_j\right) - 3\cos\theta_j\right)\right), \tag{5.9}$$

where θ_j is the geocentric zenith distance of the body j from the satellite.

Cartesian coordinates for all the perturbing planetary bodies are available at JPL, and the planetary ephemerides DE405 are chosen for this study.

5.2.5. Ocean tides

The ocean tides are modeled as variations to the spherical harmonic coefficients as specified in Chapter 6 of IERS Conventions (2003),

$$\Delta\overline{C}_{nm} - i\Delta\overline{S}_{nm} = F_{nm} \sum_{s(n,m)} \sum_{+}^{-} \left(C_{snm}^{\pm} \mp iS_{snm}^{\pm}\right) e^{\pm\theta_s}, \tag{5.10}$$

where

$$F_{nm} = \frac{4\pi G\rho_w}{g_e}\sqrt{\frac{(n+m)!}{(n-m)!(2n+1)(2-\delta_{om})}}\left(\frac{1+k_n^{'}}{2n+1}\right). \tag{5.11}$$

Here, g_e and G are the mean equatorial gravity and the constant of gravitation , ρ_w is the density of seawater ($1025\,kgm^{-3}$), $k_n^{'}$ are the load deformation coefficients ($k_2^{'} = -0.3075$, $k_3^{'} = -0.195$, $k_4^{'} = -0.132$, $k_5^{'} = -0.1032$, $k_6^{'} = -0.0892$), $C_{snm}^{\pm}$ and $S_{snm}^{\pm}$ are the ocean tide coefficients (m) for the tide constituent s, θ_s is the argument of the

tide constituent s. The summation over + and – denotes the respective addition of the retrograde waves using the top sign and the prograde waves using the bottom sign. CSR 4.0 is used for our GRACE data processing, where only eight major (semi-diurnal and diurnal) tides are used and no minor tides are used.

5.2.6. Solid Earth tide

The Earth is not a perfectly rigid body as the tides from other planetary bodies deform the Earth and can produce variation in gravitational acceleration as large as 0.2 *mgals* on the surface of the Earth; this can be approximated by [Seeber, 2003]:

$$\ddot{\mathbf{r}} = \frac{k_2}{2}\frac{Gm_j}{|\mathbf{r}_j|^3}\frac{R^5}{|\mathbf{r}|^4}(3-15\cos^2\theta_j)\frac{\mathbf{r}}{|\mathbf{r}|} + 6\cos\theta_j\frac{\mathbf{r}_j}{|\mathbf{r}_j|}, \tag{5.12}$$

where k_2 is the Love number describing the elasticity of the Earth body, m_j and $\mathbf{r}_j$ are the mass and position vector of the disturbing body j. R is the mean Earth radius, $\mathbf{r}$ is the position vector of the satellite, θ_j is the geocentric zenith distance of the body j from the satellite.

The changes induced by the solid Earth tides in the free space potential are most conveniently modeled as variations in the standard geopotential coefficients $\overline{C}_{nm}$ and $\overline{S}_{nm}$. The contributions $\Delta\overline{C}_{nm}$ and $\Delta\overline{S}_{nm}$ from the tides are expressible in terms of the Love number. The computation of the tidal contributions to the geopotential coefficients is most efficiently done by a two-step procedure. The first step is to compute the time independent terms including the permanent contribution to the geopotential coefficient $\overline{C}_{20}$, according to:

$$\Delta\overline{C}_{nm} - i\Delta\overline{S}_{nm} = \frac{k_{nm}}{2n+1}\sum_{j=2}^{3}\frac{Gm_j}{GM}\left(\frac{R_e}{|\mathbf{r}_j|}\right)^{n+1}\overline{P}_{nm}(\sin\Phi_j)e^{-im\lambda_j}, \tag{5.13}$$

where, k_{nm} is the nominal Love number for degree n and order m, R_e the equatorial radius of the Earth, G the gravitational constant, m_j the mass of body j ($j=2$ for the Moon and $j=3$ for the Sun), M the mass of the Earth, $\mathbf{r}_j$ the position vector of the body j from the geocenter, Φ_j and λ_j the body-fixed geocentric latitude and longitude of the body j. $\overline{P}_{nm}$ is the normalized associated Legendre function.

Equation (5.13) yields $\Delta\overline{C}_{nm}$ and $\Delta\overline{S}_{nm}$ for both $n=2$ and $n=3$ for all m, apart from the corrections for frequency dependence that needs to be evaluated in the step 2. The computation of changes in the coefficients of degree 4 produced by the tides of degree 2 is given by:

$$\Delta\overline{C}_{4m} - i\Delta\overline{S}_{4m} = \frac{k_{2m}^{(+)}}{5}\sum_{j=2}^{3}\frac{Gm_j}{GM}\left(\frac{R_e}{|\mathbf{r}_j|}\right)^{3}\overline{P}_{2m}(\sin\Phi_j)e^{-im\lambda_j}, (m=0,\ 1,\ 2), \tag{5.14}$$

which has the same form as equation (5.13) for $n = 2$, except for the replacement of k_{2m} by $k_{2m}^{(+)}$. The parameters k_{nm} and $k_{2m}^{(+)}$ for the computation of step 1 are given in Table 6.1 of Chapter 6 of IERS 2003.

The frequency dependence corrections to the $\Delta\overline{C}_{nm}$ and $\Delta\overline{S}_{nm}$ values, obtained from step 1, are computed in step 2 as the sum of contributions from a number of tidal constituents belonging to the respective bands such as long period, diurnal and semi-diurnal periods. More details can be found in the IERS Conventions [McCarthy and Petit, 2004].

5.2.7. Atmospheric and Oceanic variability

The short term mass variations in the atmosphere and in the oceans need to be removed in the GRACE data processing. These time varying effects have to be considered since they cannot be eliminated by the repeated observations of the GRACE measurements. The non-tidal variability can be removed by using the GRACE AOD1B products (Flechtner, 2005b). It is a combination of the ECMWF operational atmospheric fields (0.5° of spatial and 6 hours of temporal resolutions) and a barotropic ocean model driven by this atmospheric fields. The AOD1B products provide spherical surface coefficients up to degree and order 100 at an interval of 6 hours, and the value of the surface functions at intermediate epochs is obtained by linear interpolation between the bracketing data points.

5.2.8. Pole tide

The pole tide is generated by the centrifugal effect of polar motion and affects the geopotential coefficients C_{21} and S_{21}. It can be calculated according to

$$\Delta\overline{C}_{21} = -1.333\times10^{-9}(m_1 - 0.0115m_2), \tag{5.15}$$

$$\Delta\overline{S}_{21} = -1.333\times10^{-9}(m_2 + 0.0115m_1), \tag{5.16}$$

where (m_1, m_2) denote the wobble variables in seconds of arc; their relation to the polar motion variables (x_p, y_p) can be found in Chapter 7 of the IERS Conventions [McCarthy and Petit, 2004].

5.3. Data processing strategy

In this section we describe the approach to estimate the *in situ* geopotential differences and LOS gravity differences precisely, using the KBR data, accelerometer data and star sensor data (attitude data) with consideration of systematic errors in the KBR and accelerometer data.

5.3.1. Generating *in situ* LOS gravity difference observations

The KBR instrument of the GRACE satellites provides precise range measurements between the two satellites, one following the other in approximately the same plane. Let $\mathbf{r}_1 = [x_1 \quad y_1 \quad z_1]^T$ and $\mathbf{r}_2 = [x_2 \quad y_2 \quad z_2]^T$ represent the position vectors of the two satellites in the inertial frame, and ρ_{12}, $\dot{\rho}_{12}$ and $\ddot{\rho}_{12}$ represent the observed range, range

rate and range acceleration between the two satellites. From Appendix A, in case of absent random errors, we know:

$$\ddot{\rho}_{12} = \ddot{\mathbf{r}}_{12} \cdot \mathbf{e}_{12} + \frac{\left|\dot{\mathbf{r}}_{12}\right|^2 - \dot{\rho}_{12}^2}{\rho_{12}}, \tag{5.17}$$

where $\mathbf{e}_{12}$ denotes the LOS unit vector from the first satellite to the second satellite.

Introducing the KBR measurement error e into (5.17), leads to:

$$\tilde{\ddot{\rho}}_{12} = \ddot{r}_{12}^{LOS} + \frac{\left|\dot{\mathbf{r}}_{12}\right|^2 - \dot{\rho}_{12}^2}{\rho_{12}} + e, \tag{5.18}$$

where the symbol tilde indicates that the quantity was measured with the error e, and $\ddot{r}_{12}^{LOS}$ is defined to be equal to $\ddot{\mathbf{r}}_{12} \cdot \mathbf{e}_{12}$. For the convenience of future formula derivations, we introduce a new function $f(\ddot{r}_{12}^{LOS}, \mathbf{r}_{12}, \dot{\mathbf{r}}_{12}) := \ddot{r}_{12}^{LOS} + \frac{\left|\dot{\mathbf{r}}_{12}\right|^2 - \dot{\rho}_{12}^2}{\left|\mathbf{r}_{12}\right|}$ so that

$$\tilde{\ddot{\rho}}_{12} = f(\ddot{r}_{12}^{LOS}, \mathbf{r}_{12}, \dot{\mathbf{r}}_{12}) + e. \tag{5.19}$$

Since the KBR range measurements are biased and the biases are changing irregularly even over a day, in the real GRACE data processing we replace ρ_{12} by $\left|\mathbf{r}_{12}\right|$ in (5.18). The non-linear observation equations are linearized with respect to the inter-satellite state vectors and the parameter $\ddot{r}_{12}^{LOS}$ as follows:

$$y = \tilde{\ddot{\rho}}_{12} - f(\ddot{r}_{12}^{LOS}\big|_0, \mathbf{r}_{12}\big|_0, \dot{\mathbf{r}}_{12}\big|_0) = \mathbf{a}^T \boldsymbol{\xi} + e, \tag{5.20}$$

where

$$\mathbf{a}^T = \left[1 \quad \left(\frac{\partial f}{\partial \mathbf{r}_{12}}\bigg|_0 \right)^T \quad \left(\frac{\partial f}{\partial \dot{\mathbf{r}}_{12}}\bigg|_0 \right)^T \right],$$

and $\boldsymbol{\xi}^T = \left[\ddot{r}_{12}^{LOS} \quad \Delta\mathbf{r}_{12}^T \quad \Delta\dot{\mathbf{r}}_{12}^T \right]$ with $\Delta\mathbf{r}_{12}^T = \mathbf{r}_{12}^T - \mathbf{r}_{12}^T\big|_0$ and $\Delta\dot{\mathbf{r}}_{12}^T = \dot{\mathbf{r}}_{12}^T - \dot{\mathbf{r}}_{12}^T\big|_0$. The a-priori information for the inter-satellite state vectors can be obtained from the precise orbit determination, namely:

$$\begin{bmatrix} \tilde{\mathbf{r}}_{12} \\ \tilde{\dot{\mathbf{r}}}_{12} \end{bmatrix} = \begin{bmatrix} \mathbf{r}_{12} \\ \dot{\mathbf{r}}_{12} \end{bmatrix} + \mathbf{e}_0, \ \mathbf{e}_0 \sim N(\mathbf{0}, \mathbf{C}_x), \tag{5.21}$$

where $\mathbf{C}_x$ is the covariance matrix of a-priori information on the inter-satellite state vectors. The other a-priori information on the LOS gravity differences can be obtained from available geopotential and other force models,

$$\tilde{\ddot{r}}_{12}^{LOS} = \ddot{r}_{12}^{LOS} + e_{\tilde{\ddot{r}}}, \ e_{\tilde{\ddot{r}}} \sim N(0, \Sigma_{\tilde{\ddot{r}}}^2). \tag{5.22}$$

(5.19) through (5.22) are primarily used to improve the inter-satellite state vector by using the KBR measurements; this means that the parameters $\ddot{r}_{12}^{LOS}$, $\mathbf{r}_{12}$ and $\dot{\mathbf{r}}_{12}$ are estimated simultaneously to get $\hat{\ddot{r}}_{12}^{LOS}$, $\hat{\mathbf{r}}_{12}$ and $\hat{\dot{\mathbf{r}}}_{12}$. The estimated parameter $\ddot{r}_{12}^{LOS}$ is denoted by $\hat{\ddot{r}}_{12}^{LOS}$ and its covariance matrix is denoted by $N_{e_{\hat{\ddot{r}}}}^{-1}$.

The parameter $\ddot{r}_{12}^{LOS}$ includes the gravitational acceleration, non-gravitational acceleration, and also the system errors in the accelerometer and KBR measurements.

We model the systematic errors $\Delta\ddot{\rho}$ in the KBR measurements as follows:

$$\Delta\ddot{\rho} = B_1 + B_2\cos(\frac{2\pi}{T}t) + B_3\sin(\frac{2\pi}{T}t) + B_4\cos(\frac{4\pi}{T}t) + B_5\sin(\frac{4\pi}{T}t), \qquad (5.23)$$

where B_1, B_2, B_3, B_4 and B_5 are the empirical parameters to be estimated, T is the orbital period and t is the time. The systematic errors $\Delta\ddot{\rho}$ consist of bias and periodic components with frequencies such as 1-cpr (cycle-per-revolution) and 2-cpr.
We use the following error model for the accelerometer measurements:

$$\tilde{\mathbf{a}}^s(t) = \mathbf{a}^s(t) + \delta\mathbf{a}^s + \left[\tilde{\mathbf{a}}^s(t)\right]\mathbf{s}^s + (t-t_0)\delta\dot{\mathbf{a}}^s + \mathbf{e}^s(t), \qquad (5.24)$$

where $\tilde{\mathbf{a}}^s$ is the observed non-conservative force in the sensor frame denoted by the superscript s; $\delta\mathbf{a}^s$, $\mathbf{s}^s$ and $\delta\dot{\mathbf{a}}^s$ are the bias, scale factor and the drift vectors; $\left[\tilde{\mathbf{a}}^s(t)\right]$ is a 3 by 3 diagonal matrix, and $\mathbf{e}^s(t)$ is the random error of the measurement.

When considering the systematic errors in the KBR and accelerometer measurements, we define

$$\hat{\dot{r}}_{12}^{LOS} = \mathbf{g}_{12}\cdot\mathbf{e}_{12} + \mathbf{a}_{12}\cdot\mathbf{e}_{12} + \Delta\ddot{\rho} + \Delta\ddot{r}_{ACC}\cdot\mathbf{e}_{12} + e_{\hat{\dot{r}}}, \qquad (5.25)$$

where $\mathbf{g}_{12}$ is the difference of gravitational acceleration between the two satellites in the inertial frame, $\mathbf{a}_{12}$ is the difference of the measured non-gravitational acceleration vector between the two satellites transformed to the inertial frame,
$\Delta\ddot{r}_{ACC} := C_s^i\left[\delta\mathbf{a}^s + \left[\tilde{\mathbf{a}}^s(t)\right]\mathbf{s}^s + (t-t_0)\delta\dot{\mathbf{a}}^s\right]$, and $e_{\hat{\dot{r}}}$ is the random error of $\hat{\dot{r}}_{12}^{LOS}$,
$e_{\hat{\dot{r}}} \sim (0, \sigma_0^2 N_{e_{\hat{\dot{r}}}}^{-1})$. The LOS unit vector $\mathbf{e}_{12}$ in (5.25) should be denoted as estimate, $\hat{\mathbf{e}}_{12}$, since it is actually calculated from the estimated vector of $\hat{\mathbf{r}}_{12}$, but for simplicity we still denote it as $\mathbf{e}_{12}$.

Let $\boldsymbol{\beta}^T = \begin{bmatrix} B_1 & B_2 & B_3 & B_4 & B_5 \end{bmatrix}$,

$$\mathbf{b}^T = \begin{bmatrix} 1 & \cos(\frac{2\pi}{T}t) & \sin(\frac{2\pi}{T}t) & \cos(\frac{4\pi}{T}t) & \sin(\frac{4\pi}{T}t) \end{bmatrix},$$

$\boldsymbol{\gamma}^T = \begin{bmatrix} \delta\mathbf{a}^s & \mathbf{s}^s & \delta\dot{\mathbf{a}}^s \end{bmatrix}$,

$\mathbf{I}^T = \begin{bmatrix} C_i^s(t)\cdot\mathbf{e}_{12}(t) & C_i^s(t)\cdot\left[\tilde{\mathbf{a}}^s(t)\right]\cdot\mathbf{e}_{12}(t) & (t-t_0)\cdot C_i^s(t)\cdot\mathbf{e}_{12}(t) \end{bmatrix}$, then arrive at

$$\hat{\dot{r}}_{12}^{LOS} - \mathbf{g}_{12}\cdot\mathbf{e}_{12} - \mathbf{a}_{12}\cdot\mathbf{e}_{12} = \mathbf{b}^T\boldsymbol{\beta} + \mathbf{I}^T\gamma + e_{\tilde{\dot{r}}}. \qquad (5.26)$$

(5.26) is used to estimate the empirical parameters of the KBR measurements and to calibrate the accelerometer by a weighted least-squares adjustment. A global gravity model of the Earth such as EGM96 ought to be used to calculate the value of $\mathbf{g}_{12}\cdot\mathbf{e}_{12}$ in (5.25). The systematic accelerometer error vector is solved for everyday, and the systematic KBR error vector is solved for every full and every half orbital revolution. After correcting for the KBR system error $\hat{\boldsymbol{\beta}}$ and for the accelerometer system error $\hat{\boldsymbol{\gamma}}$,

and after substituting $\mathbf{g}_{12} \cdot \mathbf{e}_{12}$ and $\mathbf{a}_{12} \cdot \mathbf{e}_{12}$ by g_{12}^{LOS} and a_{12}^{LOS}, respectively, we have finally obtained the *in situ* LOS gravity differences as follows,

$$\overline{g}_{12}^{LOS} = \hat{\dot{r}}_{12}^{LOS} - a_{12}^{LOS} - \mathbf{b}^T \hat{\boldsymbol{\beta}} - \mathbf{I}^T \hat{\boldsymbol{\gamma}} . \tag{5.27}$$

5.3.2. Generating *in situ* geopotential differences observations

Estimating *in situ* geopotential difference precisely follows a similar procedure as to the estimation of LOS gravity differences the details of which can be found in Han et al., [2006b]. Here for completeness we simply introduce the models used.

Let ρ_{12} represent the observed range between the two satellites. Then we have,

$$\dot{\rho}_{12} = \dot{\mathbf{r}}_{12} \cdot \mathbf{e}_{12} , \tag{5.28}$$

and after introducing the KBR measurement error e into (5.28), it follows:

$$\widetilde{\dot{\rho}}_{12} = \dot{\mathbf{r}}_{12} \cdot \mathbf{e}_{12} + e , \tag{5.29}$$

where the symbol tilde again indicates that the quantity was measured with the random error e.

By considering the energy conservation principle along the orbit and from (2.12), we obtain

$$g(\mathbf{r}_{12}, \dot{\mathbf{r}}_{12}, V_{12}) = V_{12} - \dot{\mathbf{r}}_1^T \dot{\mathbf{r}}_{12} - \frac{1}{2}\left|\dot{\mathbf{r}}_{12}\right|^2 + E_{12}^R + E_{12}^F + C_{12} , \tag{5.30}$$

where, $E_{12}^F = \int_{t_0}^{t} (\dot{\mathbf{r}}_2 \cdot \mathbf{f}_2 - \dot{\mathbf{r}}_1 \cdot \mathbf{f}_1) dt$ and

$E_{12}^R = \omega_e (x_{12}\dot{y}_{12} + x_{12}\dot{y}_1 - y_{12}\dot{x}_{12} - y_1\dot{x}_{12} + x_1\dot{y}_{12} - y_{12}\dot{x}_1)$.

By introducing a new parameter, P_{12}, which combines the gravitational potential, dissipating potential energy and the energy constant, it follows:

$$P_{12} = V_{12} + E_{12}^F + C_{12} . \tag{5.31}$$

The non-linear observation and constraint equations are now linearized with respect to the inter-satellite state vectors and the parameter P_{12} as follows:

$$y = \widetilde{\dot{\rho}}_{12} - \dot{\mathbf{r}}_{12} \cdot \mathbf{e}_{12} = \mathbf{a}^T \boldsymbol{\xi} + e , \tag{5.32}$$

$$\kappa = 0 - g(\mathbf{r}_{12}, \dot{\mathbf{r}}_{12}, V_{12}) = \mathbf{k}^T \boldsymbol{\xi} , \tag{5.33}$$

where

$$\mathbf{a}^T = \left[0 \quad \left(\frac{\partial f}{\partial \mathbf{r}_{12}}\bigg|_0 \right)^T \quad \left(\frac{\partial f}{\partial \dot{\mathbf{r}}_{12}}\bigg|_0 \right)^T \right],$$

$$\mathbf{k}^T = \left[\left(\frac{\partial g}{\partial P_{12}}\bigg|_0 \right) \quad \left(\frac{\partial g}{\partial \mathbf{r}_{12}}\bigg|_0 \right)^T \quad \left(\frac{\partial g}{\partial \dot{\mathbf{r}}_{12}}\bigg|_0 \right)^T \right],$$

and $\xi^T = \begin{bmatrix} P_{12} & \Delta\mathbf{r}_{12}^T & \Delta\dot{\mathbf{r}}_{12}^T \end{bmatrix}$ with $\Delta\mathbf{r}_{12}^T = \mathbf{r}_{12}^T - \mathbf{r}_{12}^T\big|_0$ and $\Delta\dot{\mathbf{r}}_{12}^T = \dot{\mathbf{r}}_{12}^T - \dot{\mathbf{r}}_{12}^T\big|_0$. The a-priori information for the inter-satellite state vectors can be obtained from the precise orbit determination, namely,

$$\begin{bmatrix} \widetilde{\mathbf{r}}_{12} \\ \widetilde{\dot{\mathbf{r}}}_{12} \end{bmatrix} = \begin{bmatrix} \mathbf{r}_{12} \\ \dot{\mathbf{r}}_{12} \end{bmatrix} + \mathbf{e}_0,\ \mathbf{e}_0 \sim N(\mathbf{0}, \mathbf{C}_x), \tag{5.34}$$

where $\mathbf{C}_x$ is the covariance matrix of a-priori values for the inter-satellite state vectors. The other a-priori information of the gravitational potential differences can be obtained from available geopotential and other force models,

$$\widetilde{P}_{12} = P_{12} + e_P,\ e_P \sim N(0, \sigma_{P_{12}}^2). \tag{5.35}$$

(5.31) through (5.35) are used to estimate the inter-satellite state vector and the parameter P_{12} simultaneously.

The parameter P_{12} includes the gravitational potential, dissipating potential energy and the energy constant, and also the systematic errors in the accelerometer and KBR measurements. So, we need to model the systematic errors and estimate them from P_{12}. After correcting the systematic KBR error $\hat{\boldsymbol{\beta}}$ (with the same definition as in Section 5.3.1) and the systematic accelerometer error $\hat{\boldsymbol{\gamma}}$ (with the same definition as in Section 5.3.1), we have finally obtained the *in situ* gravitational potential difference obtained as follows:

$$\overline{V}_{12} = \hat{P}_{12} - \mathbf{b}^T\hat{\boldsymbol{\beta}} - \hat{E}_{12}^F(\hat{\boldsymbol{\gamma}}) - B_0. \tag{5.36}$$

5.3.3. Two-step least-squares adjustment

In both Sections 5.3.1 and 5.3.2, since the systematic errors of the KBR measurements are related to different orbit arcs in a day, I actually applied a two-step adjustment; this entails that, first in the data preprocessing, we estimate the $\ddot{r}_{12}^{LOS}$ or P_{12} simultaneously with the inter-satellite vectors ($\mathbf{r}_{12}$ and $\dot{\mathbf{r}}_{12}$), by exploiting the high precision KBR range rate ρ and the range acceleration $\dot{\rho}$; then we estimate the KBR system error $\hat{\boldsymbol{\beta}}$ and the accelerometer system error $\hat{\boldsymbol{\gamma}}$ from either $\hat{\ddot{r}}_{12}^{LOS}$ or $\hat{P}_{12}$. However, it needs to be proved that the two-step method provides the same solution as the one-step method, namely when estimating all the systematic errors in one step.

Let us introduce the Gauss-Markov Model,

$$\mathbf{y} = \mathbf{A}(\mathbf{R}\xi) + \mathbf{e},\ \mathrm{rk}(\mathbf{AR}) = m < n,\ e \sim (\mathbf{0}, \sigma_{\mathrm{y}}^2 \underset{n\times n}{\mathbf{P}}^{-1} =: \Sigma_{\mathrm{y}}), \tag{5.37}$$

in which $\mathbf{y}$ is the $n\times 1$ vector of observations, $\mathbf{A}$ is the $n\times p$ coefficient matrix ($n > p$), $\mathbf{R}$ is a $p\times m$ matrix ($p > m$) and will be explained in more detail later, ξ is the $m\times 1$ vector of unknown parameters, $\mathbf{e}$ is the $n\times 1$ vector of random errors, σ_{y}^2 is the unknown variance component, $\mathbf{P}$ is the $n\times n$ symmetric, positive-definite weight matrix, Σ_{y} is the $n\times n$ symmetric, positive-definite dispersion matrix.

For the LEast-Squares Solution (LESS), the normal equations are

$$\mathbf{R}^T\mathbf{N}\mathbf{R}\hat{\boldsymbol{\xi}} = \mathbf{R}^T\mathbf{c} \text{ for } [\mathbf{N},\mathbf{c}] := \mathbf{A}^T\mathbf{P}[\mathbf{A},\mathbf{y}], \tag{5.38}$$

and the final solution for the parameter vector $\boldsymbol{\xi}$ is

$$\hat{\boldsymbol{\xi}} = (\mathbf{R}^T\mathbf{N}\mathbf{R})^{-1}\mathbf{R}^T\mathbf{c}. \tag{5.39}$$

Now suppose $\boldsymbol{\zeta} = \mathbf{R}\boldsymbol{\xi}$ in which case we obtain the LEast-Squares Solution for $\boldsymbol{\zeta}$ as

$$\hat{\boldsymbol{\zeta}} = \mathbf{N}^{-1}\mathbf{c}, \text{ for } [\mathbf{N},\mathbf{c}] := \mathbf{A}^T\mathbf{P}[\mathbf{A},\mathbf{y}]. \tag{5.40}$$

After having estimated $\boldsymbol{\zeta}$ first, we can set up another Gauss-Markov Model,

$$\hat{\boldsymbol{\zeta}} = \mathbf{R}\boldsymbol{\xi} + \mathbf{e}', \ \mathbf{e}' \sim (\mathbf{0}, \sigma_y^2\mathbf{N}^{-1}), \tag{5.41}$$

Thus the LEast-Squares Solution for $\boldsymbol{\xi}$ is

$$\hat{\hat{\boldsymbol{\xi}}} = (\mathbf{R}^T\mathbf{N}\mathbf{R})^{-1}\mathbf{R}^T\mathbf{N}\hat{\boldsymbol{\zeta}} = (\mathbf{R}^T\mathbf{N}\mathbf{R})^{-1}\mathbf{R}^T\mathbf{N}\mathbf{N}^{-1}\mathbf{c} = (\mathbf{R}^T\mathbf{N}\mathbf{R})^{-1}\mathbf{R}^T\mathbf{c}, \tag{5.42}$$

which equals $\hat{\boldsymbol{\xi}}$ in (5.39).

5.4. Results and analysis

A year of continuous GRACE L1B data (from Aug. 2003 to July 2004) has been chosen to test our different regularization approaches to recover terrestrial water storage regionally. To evaluate the approaches, we choose an area covering the Amazon and Orinoco basins since the mass changes there are mainly due to tropical precipitation and floods. Monthly GRACE derived gravity models are used to recover the water storage changes globally and to evaluate them for the Amazon area. GRACE L1B data including the inter-satellite range measurements from the KBR system, non-conservative data from the onboard accelerometers, as well as orientation data of the satellites from the star cameras, are processed daily. Precise absolute orbits for the two satellites for this study are provided by CSR [S. Bettadpur, Center for Space Research (CSR), personal communication, D. Yuan, Jet Propulsion Laboratory (JPL), personal communication, and S. Zhu, GFZ, personal communication]. The orbits provided by CSR are from Aug. 2002 to May 2006, and the orbits provided by JPL are from June 2006 to Dec. 2006.

5.4.1 The *in situ* LOS gravity differences and *in situ* geopotential differences

Figure 5.2 shows the different perturbations, in terms of LOS gravity differences, arising from N-body, Solid Earth tides, Ocean tides, Pole tide, and the non-tidal variability in the atmosphere and oceans. For each perturbation, its variations in both ascending and descending arcs are plotted. The perturbations from N-body and Solid Earth tides are periodic, depending on the relative positions of the two GRACE satellites and the planetary bodies with respect to the center of the Earth. The dominant frequencies of both perturbations are 2 cycles per revolution. The effect of the non-tidal variability in the atmosphere and the oceans has a magnitude at the order of 0.1 μgal ($1\mu gal = 10^{-8}\, m\sec^{-2}$), much smaller than the other perturbations which are at the order of 1 μgal. Figure 5.3 indicates the perturbations from the same sources, but computed in terms of geopotential differences, with the unit of potential, $m^2\sec^{-2}$. The effects of the

non-tidal variability in the atmosphere and the oceans are about $\pm 0.003\ m^2\ \sec^{-2}$, while the biggest perturbation from N-body can reach $0.3\ m^2\ \sec^{-2}$.

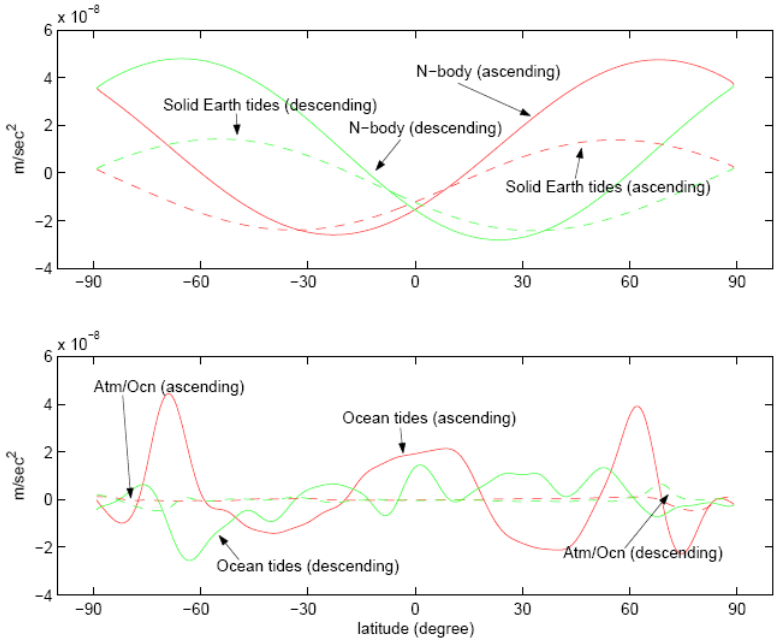

Figure 5.2: Perturbations in terms of LOS gravity differences. (a) Top: from N-body (solid), from Solid Earth tides (dashed); (b) Bottom: from Ocean tides (solid) and the non-tidal variability in the Atmosphere and Ocean (dashed). The x-axis is in latitude.

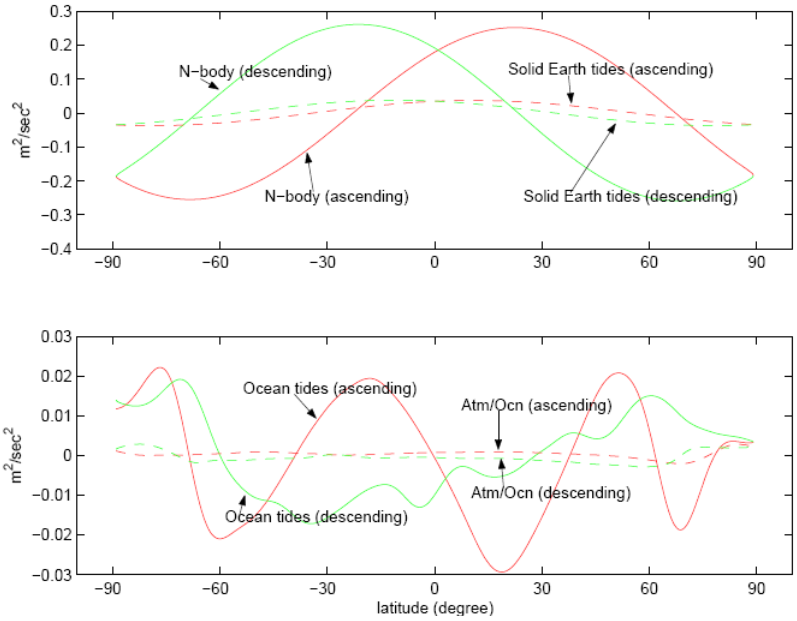

Figure 5.3: Perturbations in geopotential differences from N-body (Top panel, solid), Solid Earth tides (Top panel, dashed), Ocean tides (Bottom panel, solid), and the non-tidal variability in the Atmosphere and Ocean (Bottom panel, dashed). The x-axis is in latitude.

After all of the corrections have been based on the same geophysical models as used in the real GRACE L2 processing, both the *in situ* LOS gravity differences and the *in situ* geopotential differences are estimated following the calibration of the accelerometers and the KBR instruments, as has been developed and explained in Section 5.3. The geopotential model, GGM01C [Tapley et al., 2004a], truncated at degree and order 120, is used as a-priori approximation and subtracted from the estimates. Therefore, the estimates, δg_{12}^{LOS} or δV_{12}, represent the anomaly with respect to the GGM01C field, and should be called *in situ* incremental LOS gravity differences or incremental *in situ* geopotential differences. Instead, we will continue to call them *in situ* LOS gravity difference and *in situ* geopotential difference, and will only add the term "incremental" explicitly when it is really necessary. δg_{12}^{LOS} and δV_{12} will be predicted, too, from the monthly GRACE L2 coefficients corresponding to the same month when the GRACE L1B data are being used. Two profiles for both estimates of the *in situ* LOS gravity differences and *in situ* geopotential differences are shown in Figure 5.4. In the top part of Figure 5.4, the red line presents the *in situ* LOS gravity difference estimates, and the green line shows the same quantity, but predicted from a monthly GRACE L2 model. The x-axis of the plot is in latitude, and the profile is over the Amazon basin. The red line (the *in situ* LOS gravity differences) and green line (the predicted LOS gravity differences, but shifted by 3 μgal) agree well in phase; for instance, both of them have a jump at the region from -20° to 0° in latitude. The predicted δg_{12}^{LOS} is slightly smoother

than the *in situ* δg_{12}^{LOS}, which is to be expected since the later one is computed from a monthly GRACE gravity model, and this monthly GRACE gravity model is based on the GRACE L1B data of the whole month. The bottom part of Figure 5.4 shows the *in situ* geopotential differences and the predicted values from the same GRACE L2 model. The red line (the *in situ* geopotential differences) and the green line (the predicted geopotential differences, but shifted by $0.01\ m^2\ \sec^{-2}$) also agree well in phase generally. The two quantities, δg_{12}^{LOS} and δV_{12} are closely correlated if we compare the top figure with the bottom figure. Figure 5.4 indicates that δg_{12}^{LOS} provides more of the higher frequency information than δV_{12}, but δg_{12}^{LOS} does not have as much information as δV_{12} in the lower frequencies, since it is easier to see the low frequency variations of δV_{12} than that of δg_{12}^{LOS}. This can be explained in so far as δg_{12}^{LOS} can be seen as time derivative of δV_{12} so that it is filtered for high frequencies, and some of the low frequency information has been lost.

Figure 5.5 shows the square root of PSD of both the *in situ* LOS gravity differences δg_{12}^{LOS} and the *in situ* geopotential differences δV_{12}, and the square root of PSD of their predicted values from the corresponding monthly GRACE gravity field. The two figures on the left and right confirm that the estimates of both LOS gravity differences and geopotential differences contain more higher frequency information than their values predicted from the corresponding GRACE gravity model.

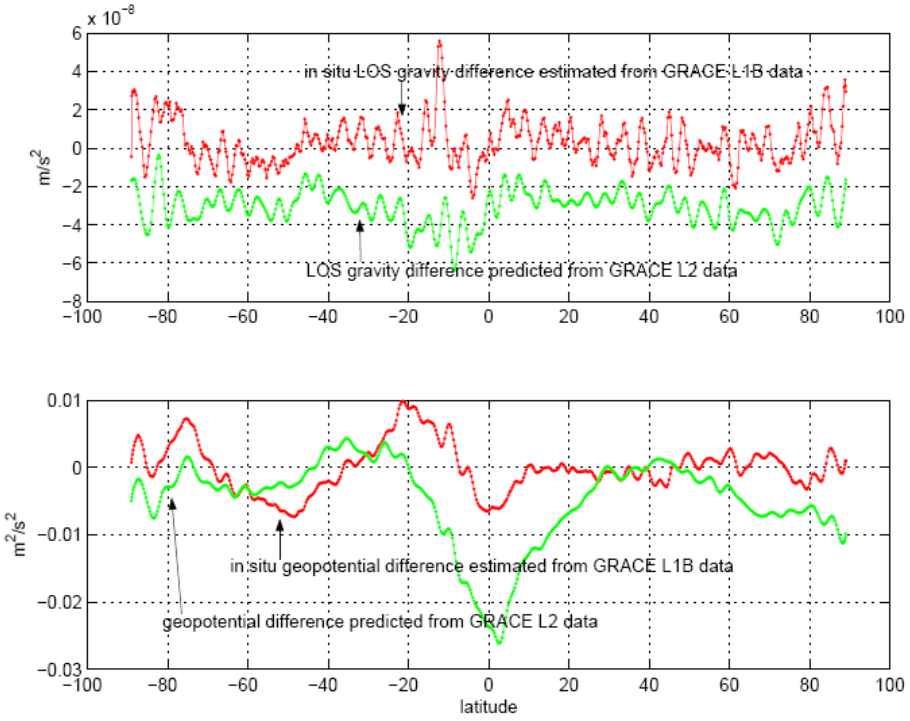

Figure 5.4: The *in situ* LOS gravity difference (top) and geopotential difference (down) estimates across the Amazon basin.

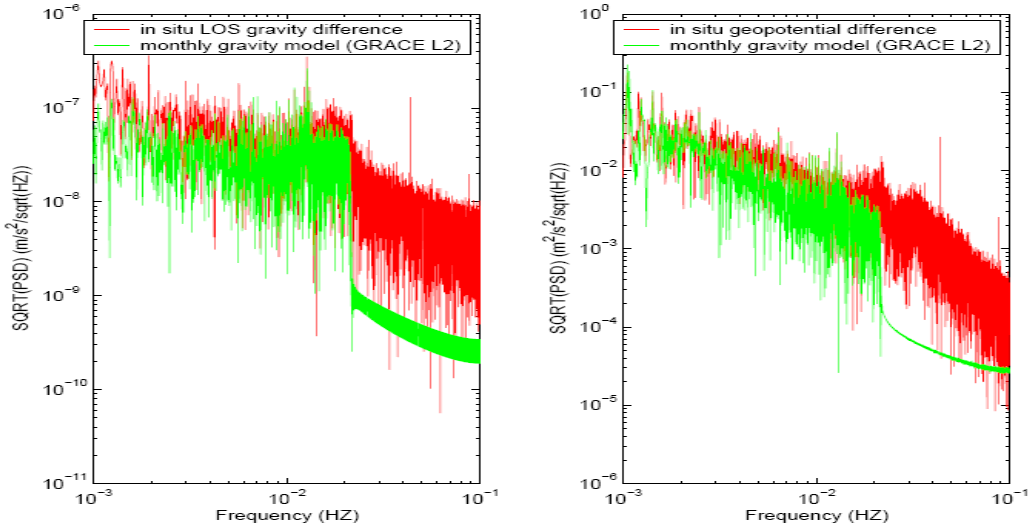

Figure 5.5: Left: Square root of PSD of *in situ* LOS gravity differences (red) and predicted values from the corresponding GRACE gravity model (green). Right: Square root of PSD of *in situ* geopotential differences (red) and predicted values from the corresponding GRACE gravity model (green).

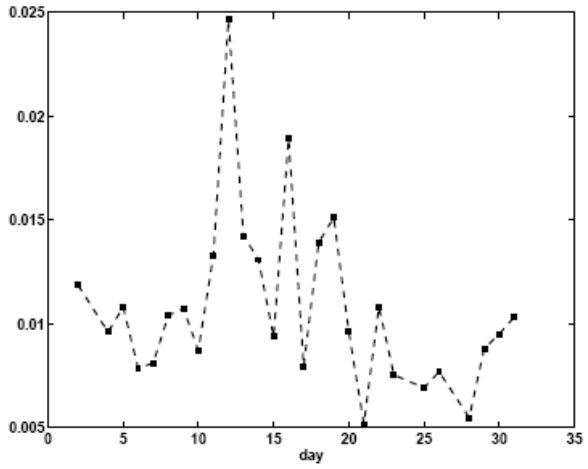

Figure 5.6: The differences of estimated *in situ* LOS gravity differences using two different initial orbits, one from CSR and the other one from GFZ. The abscissa is in day numbers of July 2003. The ordinate is in daily mean differences of the estimated *in situ* LOS gravity differences, and its unit is μgal

For this dissertation, I use the precise absolute orbits for the GRACE satellites [S. Bettadpur, Center for Space Research (CSR), personal communication], provided with a sampling rate of $5\ s$ and an estimated accuracy of $\pm 2\ cm$. We also have orbit data from the GFZ, but only for July 2003. The GFZ orbit is used to estimate the *in situ* LOS gravity differences for the month of July 2003, and Figure 5.6 shows the estimated *in situ* LOS gravity differences using two different orbits. The differences are small and $\sim 0.01 \mu gal$, indicating that the use of either orbit is sufficiently accurate for the computation.

5.4.2. Estimation of terrestrial water storage change of the Amazon basin

After obtaining the *in situ* LOS gravity differences or the *in situ* geopotential differences, the next step is to estimate the water storage change regionally. According to (3.4) or (3.9) of Chapter 3, we want to estimate continental water storage change on a set of grid points with dimentions of 2 degrees in longitude and 2 degrees in latitude. These grid points are shown as the black crosses in Figure 5.7. A month of ground tracks of the GRACE satellites, shown in the figure as blue dotted lines, guarantees that the whole Amazon basin area has been covered, even though not strictly uniformly. The green curve includes the Orinoco basin (the small upper one) and the Amazon basin (the large lower one).

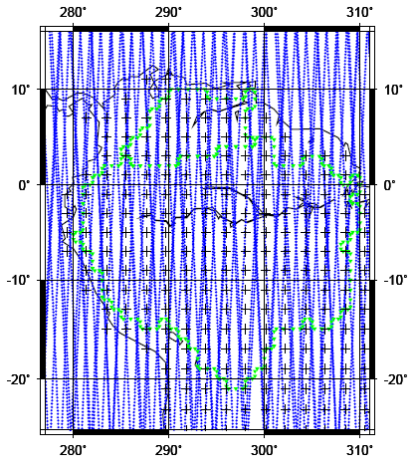

Figure 5.7: GRACE ground tracks in Aug. 2003, the $2^\circ \times 2^\circ$ grid points, and the boundaries of the Amazon and the Orinoco basins

Figures 5.8 through 5.11 are the regional solutions for which different approaches have been applied using the *in situ* LOS gravity differences. All the results cover the time period from Aug. 2003 to July 2004. Figure 5.8 shows the regional solution after applying iterative least-squares estimation with simultaneous updating of a prior covariance (Chapter 3.3.3). From the figure, we can see that the water is first accumulating at the south of the Amazon basin and then moves northward and eastward. Figure 5.9 shows the regional solution after applying Bayesian inference with variance components, which is not stable and, moreover, quite difficult to analyze as far as the pattern of the water change is concerned. This means that its final regularization parameter is too small and does not really improve or smooth the solutions enough. On the other hand, Figure 5.10 shows the regional solution after applying an optimal regularization factor via formulas for the repro-BIQUUE of variance components, with solutions that appear to be smoothed too much for the months of Aug., Sept., Oct., Nov. of the year 2003, as well as in Jan. and July of 2004. Furthermore, for Dec. 2003 and March 2004, the solutions have not been smoothed enough.

Since the approach of iterative least-squares estimation with simultaneous updating of a prior covariance achieves the best results, we tried the same approach again, but now using a new Matérn class covariance function for the a-priori covariance model [Rasmussen and Williams, 2006]. The covariance function for Figure 5.8 is the exponential function, $k(r) = \exp(-\frac{r}{l})$, where r is the distance of the two points and l is the correlation distance. However, for Figure 5.11 we use a new covariance function,

$k(r) = \left(1 + \frac{\sqrt{3}r}{l}\right)\exp(-\frac{\sqrt{3}r}{l})$. Both functions guarantee that the generated covariance matrices are positive-definite. By comparing Figure 5.8 with Figure 5.11, it can be claimed that the new covariance function also works well for this approach.

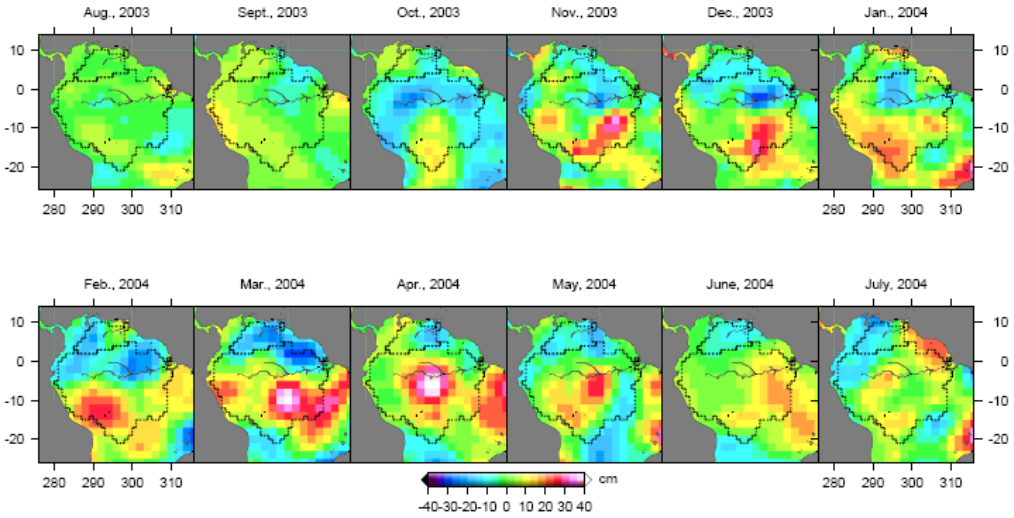

Figure 5.8: Estimates of terrestrial water storage after applying iterative least-squares estimation with simultaneous updating of a prior covariance, based on the in situ LOS gravity differences

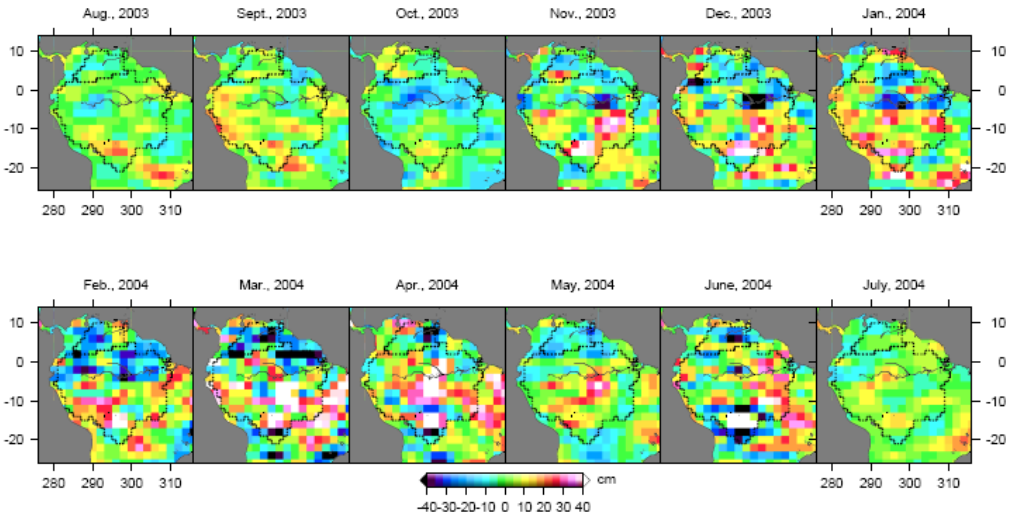

Figure 5.9: Estimates of terrestrial water storage after applying Bayesian inference with variance components, based on the *in situ* LOS gravity differences

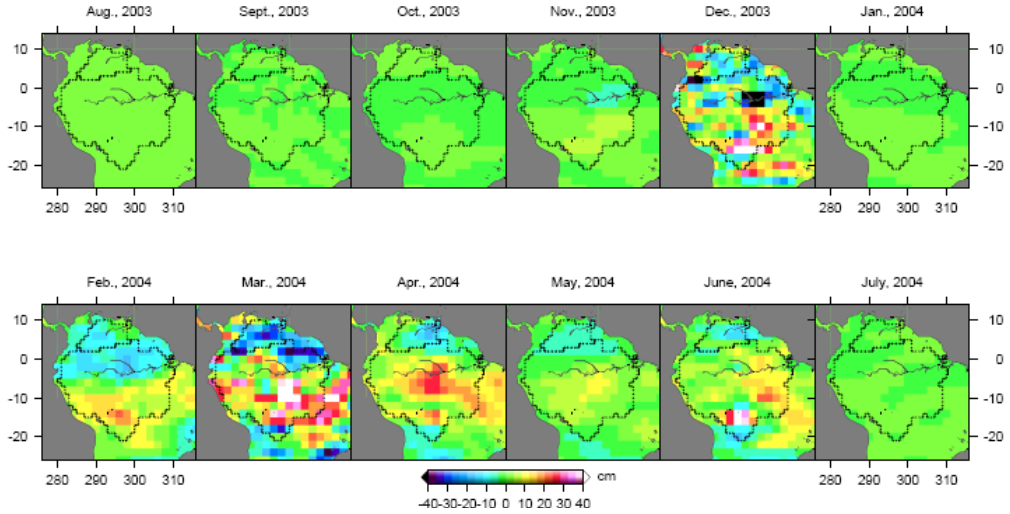

Figure 5.10: Estimates of terrestrial water storage after applying an optimal regularization factor via formulas for the repro-BIQUUE of variance components, based on the *in situ* LOS gravity differences

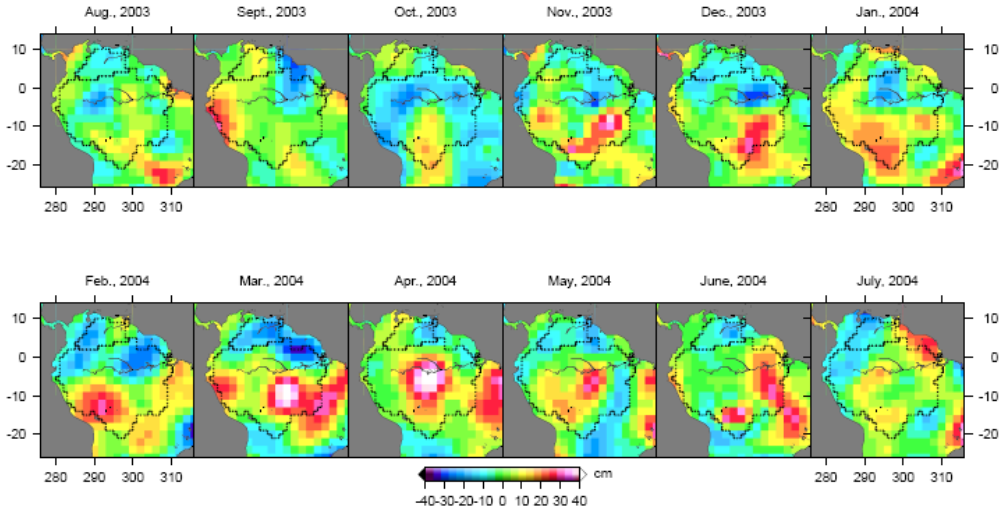

Figure 5.11: Estimates of terrestrial water storage after applying iterative least-squares estimation with simultaneous updating of a prior covariance (using a different Matérn class covariance model), based on the *in situ* LOS gravity differences

Figures 5.12 through 5.15 reflect the estimated water height changes from the *in situ* geopotential differences. Figure 5.12 represents the solutions after applying iterative least-squares estimation with simultaneous updating of a prior covariance. Figure 5.13 represents the solutions after applying Bayesian inference with variance components, resulting in unstable solutions as shown in Figure 5.9 before. Figure 5.14 shows the solutions after applying an optimal regularization factor via formulas for the repro-BIQUUE of variance components. Except for Aug. and Sept. of 2003, all other solutions agree well with the solutions shown in Figure 5.12. This means that this approach works better when using *in situ* geopotential differences instead of *in situ* LOS gravity differences, if we compare Figure 5.14 with Figure 5.12 and compare Figure 5.10 with Figure 5.8. The reason that this approach fails for Aug. and Sept. of 2003 may be that the ratio of the variance components (λ) converges to an unreasonable value, since an arbitrary initial value (zero) has been set for each parameter. Figure 5.15 is using the same approach as Figure 5.12, but a different covariance function, namely,

$k(r) = \left(1 + \frac{\sqrt{3}r}{l}\right)\exp(-\frac{\sqrt{3}r}{l})$, has been used.

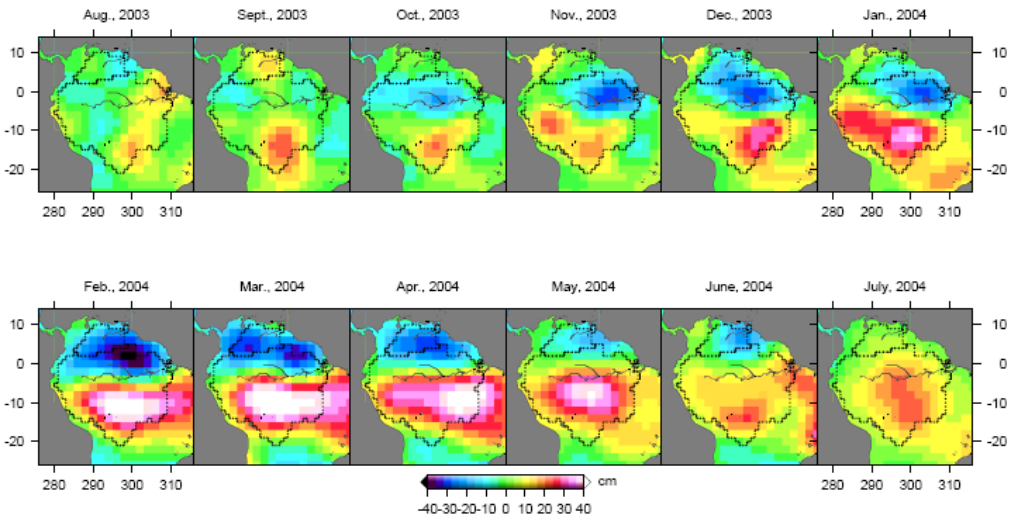

Figure 5.12: Estimates of terrestrial water storage after applying iterative least-squares estimation with simultaneous updating of a prior covariance, based on the *in situ* geopotential differences

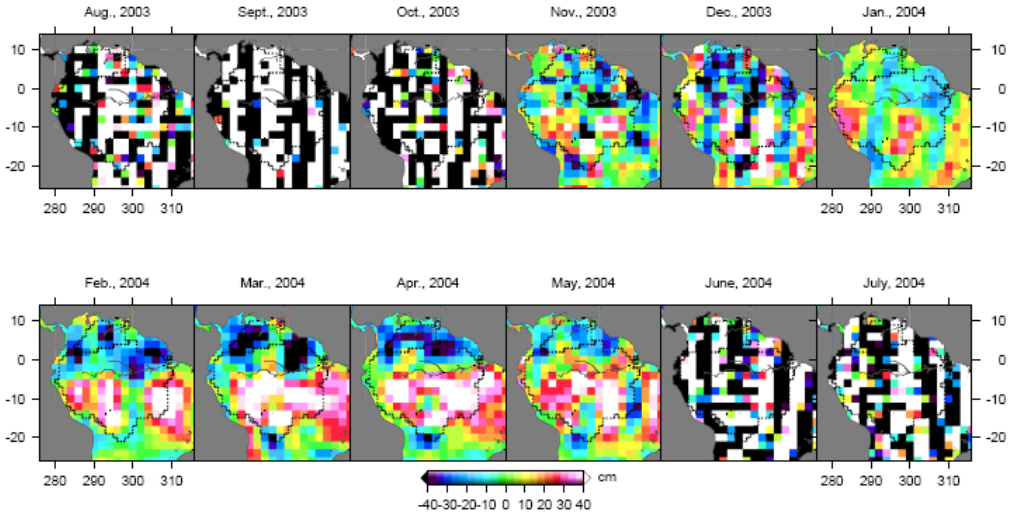

Figure 5.13: Estimates of terrestrial water storage after applying Bayesian inference with variance components, based on the *in situ* geopotential differences

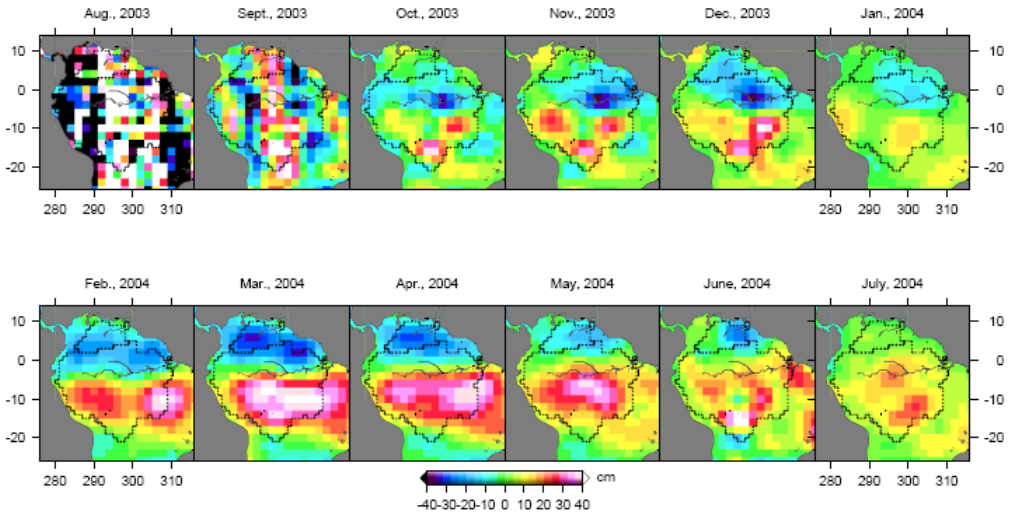

Figure 5.14: Estimates of terrestrial water storage after applying an optimal regularization factor via formulas for the repro-BIQUUE of variance components, based on the *in situ* geopotential difference

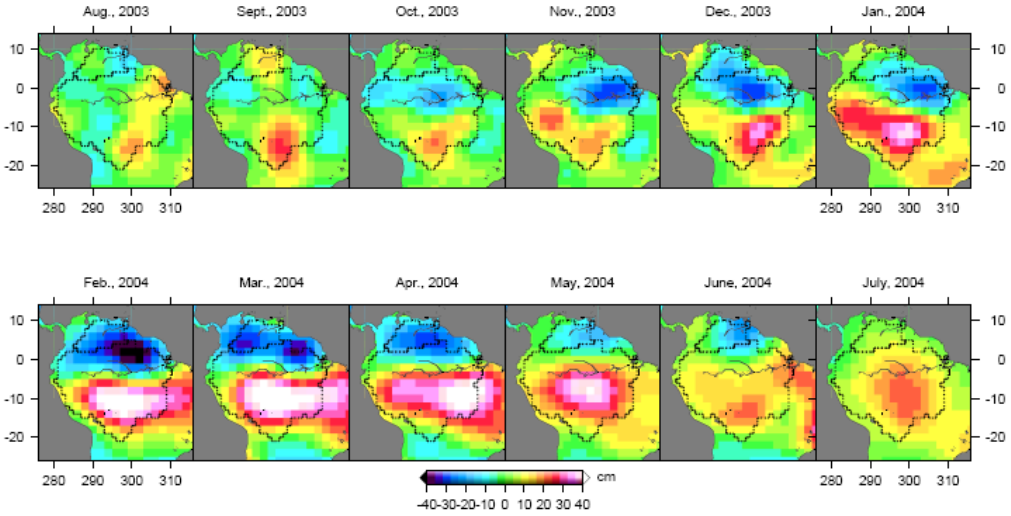

Figure 5.15: Estimates of terrestrial water storage after applying iterative least-squares estimation with simultaneous updating of a prior covariance (using a different Matérn class covariance model), based on the *in situ* geopotential differences

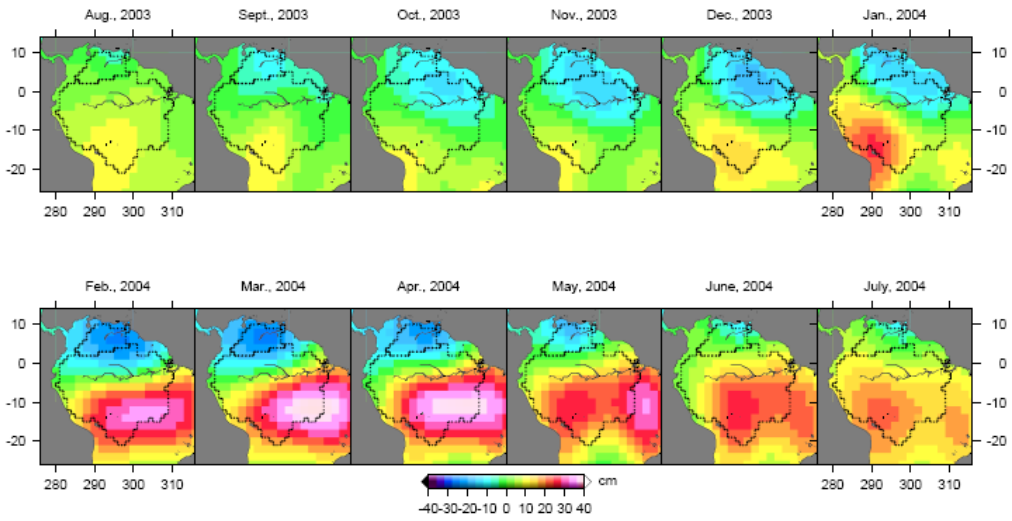

Figure 5.16: Terrestrial water storage changes using a monthly GRACE L2 gravity model after Gaussian smoothing (600km smoothing radius)

Figure 5.16 shows the global solution from the corresponding monthly GRACE gravity field models, after applying Gaussian smoothing with radius of 600 km. The regional solutions from Figures 5.8 through 5.15 are all qualified to be compared to the global solutions in Figure 5.16. First, the regional solutions using *in situ* geopotential difference show more higher frequency information than the global solutions; for instance, more of the water change estimates from Figure 5.12 than those from Figure 5.16 sit inside the boundaries of the Orinoco and the Amazon. Second, by comparing Figure 5.12 and Figure 5.8 to Figure 5.16, it can be claimed that higher frequency information can be achieved from *in situ* LOS gravity differences.

To have a clearer idea of how different approaches (except the Bayesian inference with variance components) perform for different observations in the frequency domain, I computed the averaged monthly Power Spectral Density (PSD) over the study region, and the results are shown in Figure 5.17. For the regional solutions, I used $n = 2\pi Rf$ to convert the planar frequency f to the spherical harmonics degree n [Jekeli, 1981]. In Figure 5.17 we can see that the approach based on iterative least-squares estimation with simultaneous updating of a prior covariance (using the covariance function $k(r) = \left(1 + \frac{\sqrt{3}r}{l}\right)\exp(-\frac{\sqrt{3}r}{l})$) achieves the highest resolution, if the observation are the *in situ* LOS gravity differences. If the observations, however, are the *in situ* geopotential differences, the approach of an optimal regularization factor via formulas for the repro-BIQUUE of variance components achieves the highest resolution. The approach based on Bayesian inference with variance components is not included in the comparison since its solutions are not stable for either observation type.

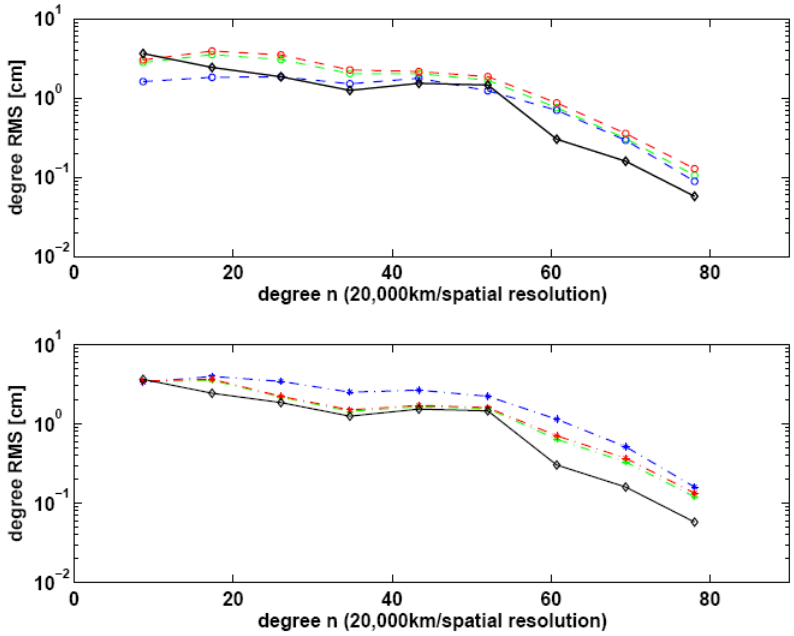

Figure 5.17: Square root of PSD of estimated water height changes. (a) The top panel is for the use of the *in situ* LOS gravity differences, red dashed line corresponds to Figure 5.11, green dashed line corresponds to Figure 5.8, blue dashed line corresponds to Figure 5.10; (b) The bottom panel is for the use of the *in situ* geopotential differences, red dashed line corresponds to Figure 5.15, green dashed line corresponds to Figure 5.12, blue dashed line corresponds to Figure 5.14. In both panels, the black solid line represents the estimated water height changes from a monthly GRACE geopotential model (GRACE L2 data product).

5.4.3. Estimation of the terrestrial water storage change of the Congo river area

To further investigate the recovery of the continental water storage change, we choose another place, the Congo River area, to test the two approaches using either the *in situ* geopotential differences or the *in situ* LOS gravity differences. The Congo River area is the largest river in the western part of central Africa. Its overall length of 4,700 km makes it the second longest in Africa (after the Nile). The river has the second-largest watershed of any river, trailing the Amazon. From the global hydrologic model of NCEP as shown in Figure 4.4, the Congo river area is also experiencing huge water changes with a period of about one year. Here, based on the results of section 5.4.2, we only show the results after applying iterative least-squares estimation with simultaneous updating of a prior covariance, either using *in situ* geopotential differences or *in situ* LOS gravity differences. It has to be pointed out that, in Jan. 2004, there have much less L1B data been available than for the other months (about ¼ of the other months). Figure 5.20 shows the results from the GRACE L2 data after Gaussian smoothing with a radius of 600 km. Figure 5.18 and Figure 5.19 show the results from using *in situ* LOS gravity differences and *in situ* geopotential differences, respectively. Figure 5.19 is closer to Figure 5.20 than Figure

5.18, which means that the regional solutions from using *in situ* geopotential differences perform better in the low frequency domain, while the regional solutions from using *in situ* LOS gravity differences achieve better results in the relatively high frequency domain. Figure 5.21 confirms the conclusions above.

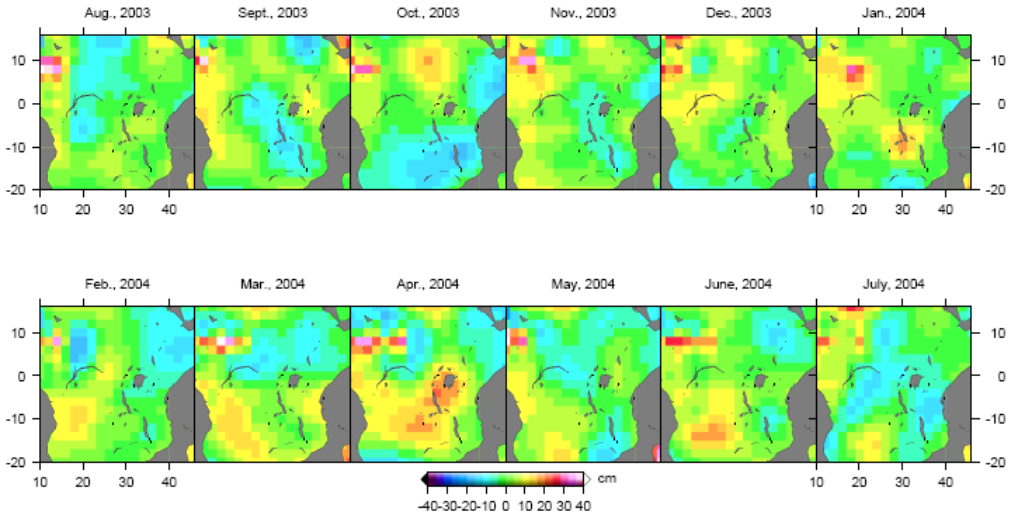

Figure 5.18: Estimates of terrestrial water storage after applying iterative least-squares estimation with simultaneous updating of a prior covariance, based on the *in situ* LOS gravity differences

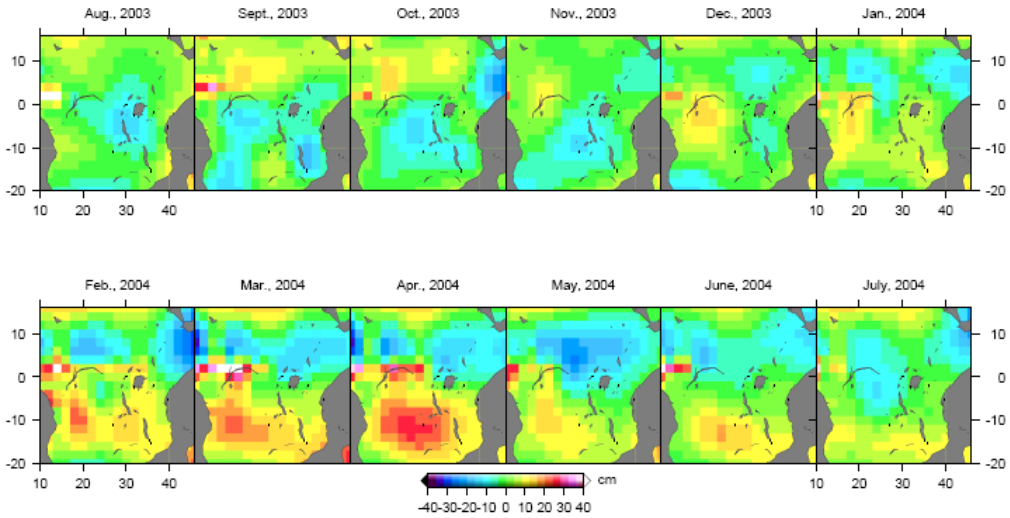

Figure 5.19: Estimates of terrestrial water storage after applying iterative least-squares estimation with simultaneous updating of a prior covariance, based on the *in situ* geopotential differences

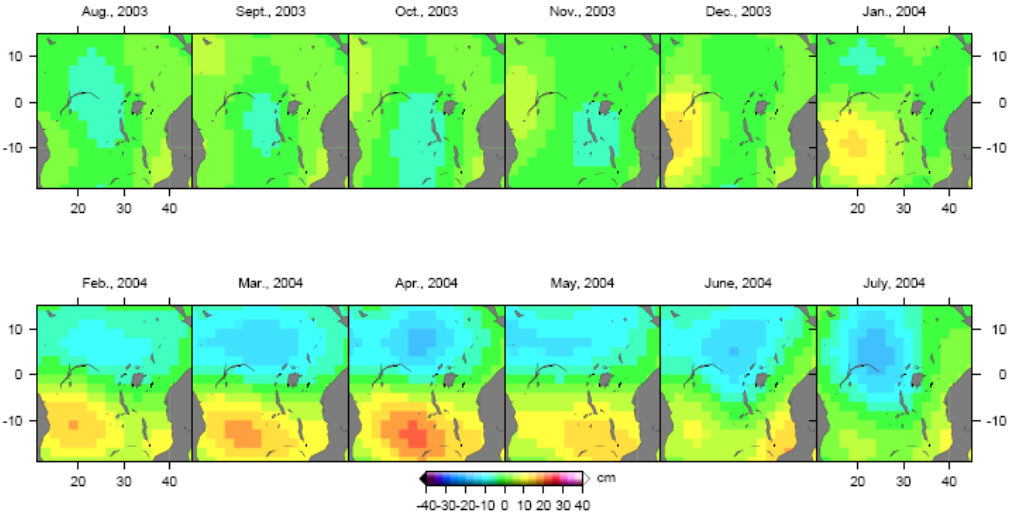

Figure 5.20: Terrestrial water storage changes using monthly GRACE L2 gravity model after Gaussian smoothing (600km smoothing radius)

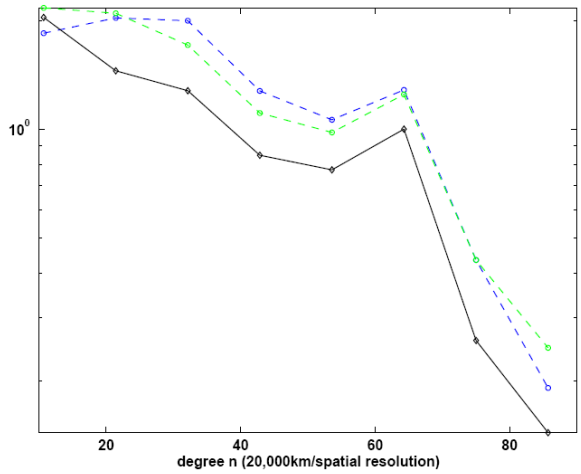

Figure 1

Figure 5.21: Square root of PSD of estimated water height changes (averaged monthly PSDs over one year). The blue line represents the square root of PSD (in the unit if equivalent water thickness, cm) of the results from using *in situ* LOS gravity differences. The green line represents the square root of PSD of the results from using *in situ* geopotential differences. The black line represents the degree variances from GRACE L2 data after Gaussian smoothing with the radius 600 km.

CHAPTER 6

CONCLUSIONS AND FUTURE WORK

For hydrologists it is critical to quantify the global water cycle, e.g., where and in what quantities the Earth stores water and how it moves with time and locations, which today is still insufficiently known due to the difficulty of direct measurements. Some space-based technologies measure various components in the global water cycle, including precipitation [Simpson et al., 1988], terrestrial surface water [Alsdorf and Lettenmaier, 2003], soil moisture [Entekhabi et al., 2004], glaciers [Schutz et al., 2005], and snow [Cline, 2005]. GRACE senses the integration of all the components since its orbit is disturbed by whatever mass anomalies on or under the surface of the Earth. In other words, GRACE measurements cannot separate one component from another one in the global water cycle. However, in some regions, it has been clarified which geophysical process contributes most to the mass changes there, such as post-glacial rebound for the Hudson bay area, and the hydrological fluxes for the Amazon basin and the Congo river area.

I have done both a closed-loop simulation study as well as real GRACE data processing to recover terrestrial water storage change globally and regionally. The LOS gravity differences as well as the geopotential differences, are the two primary observation types in this dissertation. Three different regularization approaches have been tested for both the simulation study and the real case.

In the simulation study, the global grid data of the terrestrial water storage from NCEP/NCAR (of year 2003) are first converted into global spherical harmonic coefficients, and then adopted to simulate the perturbed orbits of the two GRACE satellites. The initial Keplerian elements of the two GRACE satellites are set so that the generated orbits are as close as possible to the real GRACE situation. From the simulated orbits, we produce the two primary GRACE observations, i.e., the LOS gravity differences and geopotential differences. Each of them is used to estimate the water storage change globally, and regionally for the Amazon basin area, applying the three different regularization approaches described in Chapter 3.3. First, it is confirmed that the regional solutions from either *in situ* LOS gravity differences or *in situ* geopotential differences can achieve higher resolution than the global resolutions (after Gaussian smoothing), as shown in Figure 4.19 and 4.28. Second, as indicated in Figure 4.24, the global solutions from using LOS gravity differences obtain a better resolution than the global solutions from using geopotential differences. Third, the regularization approaches,

iterative least-squares estimation with simultaneous updating of the a-priori covariance (Chapter 3.3.3) and the use of an optimal regularization factor via formulas for the repro-BIQUUE of variance components (Chapter 3.3.2), always perform better than the third approach, namely Bayesian inference with variance components. Finally, I have analyzed the effects of the potential modeling errors of the atmosphere pressure and the ocean tides (only considering the four components, K_1, O_1 , M_2 and S_2), and it is concluded that the recovery of the continental water storage change is not affected by the modeling errors. The reason is that the perturbations produced by the modeling errors of the atmosphere pressure and the ocean tides are one order of magnitude smaller than the signals from the water storage change on the continents (except Antarctica or Greenland where were excluded in the simulation study). However, this is based upon the assumption that the modeling differences can represent the modeling errors of the atmosphere pressure and the ocean tides, which is of course not entirely true.

For the real GRACE data processing, one year of the GRACE L1B data from Aug. 2003 to July 2004 is used to recover the continental water storage changes globally and regionally. I did consider all the perturbations, such as those caused by N-body, ocean tides, solid Earth tide, atmosphere and ocean variability, as well as solid Earth pole tide. The corrections are based on the same models as in the GRACE L2 processing according to the GRACE L2 document [Bettadpur, 2006]. The non-conservative effects are corrected by the measurements of the accelerometers on board the twin GRACE satellites. After calibration of the KBR and the accelerometer measurements, we estimate precisely the *in situ* LOS gravity differences and the *in situ* geopotential differences by exploiting the high precision KBR measurements such as range rates and range accelerations. Precise orbits have been provided by S. Bettadpur [CSR, personal communication, D. Yuan, Jet Propulsion Laboratory (JPL), personal communication], and by GFZ (for July 2003), it is concluded that different approximations of the initial precise orbits only cause an average difference of $\sim 0.01 \mu gal$ in terms of the *in situ* LOS gravity differences. In the present procedure to estimate precisely the *in situ* LOS gravity differences or the *in situ* geopotential differences, I first estimate the *in situ* LOS acceleration differences ($\ddot{r}_{12}^{LOS}$) or the *in situ* potential differences (P_{12}), and then calibrate both the KBR and the accelerometer measurements to finally calculate the *in situ* LOS gravity differences and the *in situ* geopotential differences. The two-step estimation procedure has been confirmed to yield the same solution as the standard least-squares adjustment in Chapter 5.3.3. For the regional solutions using the *in situ* LOS gravity differences, the solutions applying Bayesian inference with variance components are not stable as shown in Figure 5.9, while the solutions using an optimal regularization factor via formulas for the repro-BIQUUE of variance components, appeared to be smoothed too much for some months as shown in Figure 5.10. For the regional solutions using the *in situ* geopotential differences, the solutions applying Bayesian inference with variance components are still not stable; but the solutions from applying an optimal regularization factor via formulas for the repro-BIQUUE of variance components perform better than in the case of using the *in situ* LOS gravity differences, with the exceptions of the solutions of Aug. and Sept. of 2003. It is obvious that overall the regularization approach, based on iterative least-squares estimation with simultaneous updating of a prior covariance, has always achieved

stable and reliable solutions. There are actually three variance components involved in iterative least-squares estimation with simultaneous updating of a prior covariance, namely, σ_y^2, σ_x^2 and l, from which two ratios of the variance components can be combined. With the two ratios, this approach is more flexible and more likely to approximate the reality. I have tried the same approach again, but using a different Matérn class covariance function, and the approach still works perfectly. If the observation is the *in situ* LOS gravity difference, iterative least-squares estimation with simultaneous updating of a prior covariance (using the covariance function $k(r) = \left(1 + \frac{\sqrt{3}r}{l}\right)\exp(-\frac{\sqrt{3}r}{l})$) even achieves the highest resolution as shown in Figure 5.17. If the observation is the *in situ* geopotential difference, however, the approach of an optimal regularization factor via formulas for the repro-BIQUUE of variance components achieves the highest resolution. All the regional solutions perform better than the global solutions based on the smoothed global solutions from GRACE L2 models. When we only pick up the two regional solutions from applying iterative least-squares estimation with simultaneous updating of a prior covariance, we can conclude that the solutions from using the *in situ* LOS gravity differences achieve a better resolution than the solutions from using the *in situ* geopotential differences as shown in Figure 5.8 and Figure 5.12. This has been confirmed based on Figure 5.21 when we moved to the Congo river area.

Other methods that can be used to study the temporal gravity field of the Earth include the mascon approach [Rowlands et al., 2005; Lemoine et al., 2005;Yuan & Watkins, 2006] and downward continuation based on some suitable integral equations [Mayer-Gürr et al., 2006]. It will be interesting to compare the results from this approach, the use of *in situ* LOS gravity differences, to the methods mentioned above. Also, hydrologists are achieving a fine scale (20 km full-wavelength) hydrologic model of the Amazon basin [Beighley et al., 2006], which accounts for the modeling of surface, subsurface, channel and floodplain stores and fluxes. The fine scale model will help us to validate what GRACE exactly measures, and to explain the controversy of the allegedly observed 1–2 month lags between the GRACE data and a number of global hydrologic models.

The techniques of recovery of the global gravity field of the Earth are being continuously improved, from tracking some satellites at high altitude over decades to the dedicated gravity satellite missions, from high-low SST (CHAMP) to low-low SST (GRACE) and to satellite gravity gradiometry (GOCE). In other words, we are always aiming on improving the estimates of the short-wavelength signals. A combination of GRACE Satellite-To-Satellite tracking and GOCE gradiometry could potentially improve short-wavelength accuracy of terrestrial water storage change.

BIBLIOGRAPHY

Ali, A.H., and V. Zlotnicki (2003), Quality of wind stress fields measured by the skill of a barotropic ocean model: Importance of stability of the Marine Atmospheric Boundary Layer, Geophys. Res. Lett. , 30(3), 1129, doi:10.1029/2002GL016058.

Alsdorf, D.E. and D.P. Lettenmaier (2003), Tracking fresh water from space, Science 301, 1491-1494.

Arsenin VY and Krianev AV (1992), Generalized maximum likelihood method and its application for solving ill-posed problems, In: Tikhonov A (ed) Ill-posed problems in natural sciences, TVP Scinece Publishers, Moscow, pp3-12.

Austen G., E.W. Grafarend, T. Reubelt (2002), Analysis of the Earth's Gravitational Field from Semi-Continuous Ephemeris of a Low Earth Orbiting GPS-Tracked Satellite of Type CHAMP, GRACE or GOCE, J. Adam and K.P. Schwarz (Eds): Vistas for Geodesy in the New Millenium, pp. 309-315, Springer Verlag, Berlin-Heidelberg.

Beighley R.E., K. Eggert, Y. He and V. Gummadi (2006), Integrating fine scale hydrologic processes over large spatial and temporal extents, Session H23A, AGU Fall Meeting, San Francisco, CA, Dec. 2006.

Bettadpur, S., and M. Watkins (2000), GRACE gravity science and its impact on mission design, AGU Spring Meeting, Washington DC, May 30 – June 3, 2000.

Bettadpur, S. (2003), UTCSR Level-2 Processing Standards Document For Level-2 Product Release 0001 (GRACE 327-742), Rev. 1.0, Cent. for Space Res., Univ. of Texas at Austin/TX, Dec. 2003.

Bettadpur, S. (2004), Gravity Recovery and Climate Experiment Product Specification Document (GRACE 327-720), Rev. 4.1, Cent. for Space Res., Univ. of Texas at Austin/TX, Jan. 2004.

Bettadpur, S. (2006), Level-2 gravity field product user handbook (GRACE 327-734), Rev. 2.1, Cent. for Space Res., Univ. of Texas at Austin/TX, May 2006.

Bettadpur, S., D. Chamber, F. Flechtner, R. Schmidt, S. Swenson, D. Yuan, J. Wahr, V. Zlotnicki (2005), Status report, UTCSR RL02 reprocessing, GRACE Science Team Meeting, Austin, Texas, Oct. 2005.

Biancale, R., G. Balmino, S. Bruinsma, J. Lemoine, S. Loyer, F. Perosanz (2005), GRACE data processing in CNES/GRGS; results and discussion, GRACE Science Team Meeting, Austin, Texas, Oct. 2005.

Chambers, D., J. Wahr, and R. S. Nerem (2004), Preliminary observations of global ocean mass variations with GRACE, Geophys. Res. Lett., 31, L13310, doi:10.1029/2004GL020461.

Chambers, D. (2006a), Observing seasonal steric sea level variations with GRACE and satellite altimetry, J. Geophys. Res., 111, C03010, doi:10.1029/2005JC002914.

Chambers, D. (2006b), Evaluation of new GRACE time-variable gravity data over the ocean, Geophys. Res. Letts., 33, L17603, DOI:10,1029/2006GL027296.

Chao, B. F. (2005), On inversion for mass distribution from global (time-variable) gravity field, J. Geodynamics, 39, 223-230.

Chen, J. L., C. R. Wilson, and K.W. Seo (2006a), Optimized smoothing of Gravity Recovery and Climate Experiment (GRACE) time-variable gravity observations, J. Geophys. Res., 111, B06408, doi:10.1029/2005JB004064.

Chen, J.L. C.R. Wilson, B.D. Tapley (2006b), Satellite gravity measurements confirm accelerated melting of Greenland ice Sheet, Science, in press.

Chen, J.L., C.R. Wilson, J.S. Famiglietti, M. Rodell (2006c), Attenuation effect on seasonal basin-scale water storage change from GRACE time-variable gravity J. Geodesy, in review.

Chen, J.L., B.D. Tapley, C.R. Wilson (2006d), Alaskan mountain glacial melting observed by satellite gravity, Earth and Planetary Science Letters,Vol. 248, Issues 1-2, pp 368-378, doi:10.1016/j.epsl.2006.05.039.

Chen, J.L., C.R. Wilson, D.D. Blankenship, B.D. Tapley (2006e), Antarctic mass change rates from GRACE, Geophys. Res. Lett., 33, L11502, doi:10.1029/2006GL026369.

Chen, Y.Q., S. Han, B. Schaffrin and C. Shum (2004), Calibration of CHAMP accelerometer observations for precise determination of in-situ gravity measurements, J. of Geospatial Eng., 6(1), 1–12.

Chen, Y.Q., B. Schaffrin and C.K. Shum (2006), Continental water storage changes from GRACE line-of-sight range acceleration measurements, Proc. VI Hotine-Marussi International Symposium of Theoretical and Computational Geodesy: Challenge and Role of Modern Geodesy, (Wuhan, China, May29-June 2, 2006), accepted for publication.

Ciufolini, I., and E. Pavlis (2004), A confirmation of the general relativistic prediction of the Lense-Thirring effect, Nature, 431, 958–960.

Cline, D. (2005), Cold-land Processes Pathfinder Mission (CLPP): Advanced Space-based Observation of Fresh Water Stored in Snow, Session H13J, AGU Fall Meeting, San Francisco, CA, Dec. 2005.

Davis, A., C. Dunn, R. Stanton, and J. Thomas (1999), The GRACE mission: Meeting the technical challenges, 50th International Astronautical Congress, Amsterdam, Netherlands, October 4–8, 1999.

Davis, J., P. Elo´segui, J. Mitrovica and M. Tamisiea (2004), Climate-driven deformation of the solid Earth from GRACE and GPS, Geophys. Res. Lett., 31, L24605, doi:10.1029/2004GL021435.

Davis, J., M. Tamisiea, and T. Herring (2006), Horizontal GIA velocities and reference-frame determination, http://www.unavco.org/research_science/workinggroups_projects/snarf/snarf.html, presented at the Stable North American Reference Frame (SNARF) Working Group Meetiing, 2006.

Desai, S., R. Gross, J. Wahr (2006), The impact of the ocean pole tide on various geodetic observables, Geophys. Res. Abstracts 8, 019168, SRef-ID: 1607-7962/gra/EGU06-A-09168.

Desai, S.D. and D.N. Yuan (2006), Application of the convolution formalism to the ocean tide potential: Results from the Gravity Recovery and Climate Experiment (GRACE), J. Geophys. Res., 111(C06023), doi:10.1029/2005JC003361.

Dickey, J.O., C. R. Bentley, R. Bilham, J. A. Carton, R.J.Eanes, T.A. Herring. W. M. Kaula, G.S. E. Lagerhof, S. Rojstaczer, W.H.F. Smith, H M. van den Dool, J. M. Wahr and M. Zuber (1997), Satellite Gravity and the Geosphere, National Research Council Report, 112 pp., Nat. Acad., Washington, D.C..

Ditmar, P. and R. Klees (2002), A Method to Compute the Earth's Gravity Field from SGG/SST Data to be Acquired by the GOCE satellite, Delft University Press, Delft/NL.

Ditmar, P., A. A. van Eck van der Sluijs (2004), A technique for modeling the Earth's gravity field on the basis of satellite accelerations, J. Geodesy, 78(1-2):12-33.

Dunn, C., W. Bertiger, Y. Bar-Sever, S. Desai, B. Haines, D. Kuang, G. Franklin, I. Harris, G. Kruizinga, T. Meehan, S. Nandi, D. Nguyen, T. Rogstad, J. Brooks Thomas, J. Tien, L. Romans, M. Watkins, S.-C. Wu, S. Bettadpur, J.G. Kim (2003), Instrument of GRACE: GPS augments gravity measurements, GPS World, 14(2), 16-28.

Eanes, R. and S. Bettadpur (1995), The CSR 3.0 global ocean tide model, Technical memorandum, CSR-TM-95-06, Center for Space Research, University of Texas at Austin.

Egbert, E. and R. Ray (2002), Deviation of long period tides from equilibrium: Kinematics and geostrophy, J. Physical Oceanography, Vol. 33., pp. 822-839.

Entekhabi, D., E. Njoku, P. Houser, M. Spencer, T. Doiron, S. Belair, W. Crow, T. Jackson, Y. Kerr, J. Kimball, R. Koster, K. McDonald, P. O'Neill, T. Pultz, S. Running, J.C. Shi, E. Wood, J. van Zyle (2004), The Hydrosphere Satellite (HYDROS) mission concept: An earth system pathfinder for global mapping of soil moisture and land freeze/thaw, IEEE Transactions on Geoscience and Remote Sensing, 42:2184-2195.

Flechtner, F. (2005a), Status of atmosphere and ocean dealiasing Level-1B product (AOD1B), GRACE Science Team Meeting, Austin, Texas, 13-14 October 2005.

Flechtner, F. (2005b), AOD1B Product Description Document (GRACE 327-750), GeoForschungszentrum Potsdam, Rev. 2.1, November, 2005.

Forsberg, R., M. Sideris, and C. Shum (2005), The gravity field and IGGOS, J. of Geodynamics, 40, 4-5, 387-393, doi:10.1016/j.jog.2005.06.014.

Han, S.C., C. Jekeli, C.K. Shum (2003a), Static and temporal gravity field recovery using GRACE potential difference observables, Advances in Geosciences, 1, 19-26.

Han, S.C. (2003b), Efficient Global Gravity Determination from Satellite-to-Satellite Tracking (SST), Technical Report #467, Geodetic Science and Surveying, The Ohio State University.

Han, S.C., C. Jekeli, and C.K. Shum (2004), Time-variable aliasing effects of ocean tides, atmosphere, and continental water mass on monthly mean GRACE gravity field, J. Geophys. Res. 109(B4), B04403, 10.1029/2003JB002501.

Han, S.-C., C.K. Shum, and A. Braun (2005a), High-resolution continental water storage recovery from low-low satellite-to-satellite tracking. J. Geodyn., 39(1), 11-28.

Han, S.-C., C.K. Shum, C. Jekeli, and D. Alsdorf (2005b), Improved estimation of terrestrial water storage changes from GRACE, Geophys. Res. Lett., 32, L07302, doi:10.1029/2005GL022382.

Han, S.C., C.K. Shum, K. Matsumoto (2005c), GRACE observations of M2 and S2 ocean tides below the Filchner-Rønne and Larsen Ice Shelves, Antarctica, Geophys. Res, Lett., 32, L20311, doi:10.1029/2005GL024296.

Han, S., C. Shum, P. Ditmar, P. Visser, C. van Beelen, E. Schrama (2006a), Effect of high-frequency mass variations on GOCE recovery of the Earth's gravity field, J. Geodynamics, 41, 67–76.

Han, S., C. Shum, C. Jekeli (2006b), Precise estimation of *in situ* geopotential difference from GRACE low-low satellite-to-satellite tracking and accelerometry data, J. Geophys. Res., 111, B04411, doi:10.1029/2005JB003719.

Han, S.C., C.K. Shum, M. Bevis, C. Ji, and C. Kuo (2006c), GRACE observed crustal dilatation following the 2004 Sumatra-Andaman Earthquake, Science, 313, 658–662.

Han, S.C., C.K. Shum (2006d), Coseismic gravity change following the December 2004 Sumatra-Andaman earthquake: Evidence in the GRACE global gravity fields, Geophysical Research Letters, In-review.

Ilk, K.H., J. Flury, R. Rummel, P. Schwintzer, W. Bosch, C. Haas, J. Schröter, D. Stammer, W. Zahel, H. Miller, R. Dietrich, P. Huybrechts, H. Schmeling, D. Wolf, H.J. Götz, J. Riegger, A. Bardossy, A. Güntner, TH. Gruber (2005), Mass Transport and Mass Distribution in the Earth System, GeoForschungsZentrum Potsdam, 2nd Edition, 154pp..

Ivins, E.R., and T.S. James (2005), Antarctic glacial isostatic adjustment: A new assessment, Antarctic Science, 17(4), 541-553.

Ivins, E., E. Rignot, X. Wu, T. James and T. Casassa (2005), Ice mass balance and Antarctic gravity change: Satellite and terrestrial perspectives, Earth Observation with CHAMP: Results from 3 years in Orbit, Springer: Berlin/Heidelberg, 3–12.

Jekeli, C. (1981), Alternative methods to smooth the Earth's gravity field, Tech. Rep. #327. Dept. of Geod. Sci. and Surv., Ohio State University, Columbus/OH.

Jekeli, C. (1999), The determination of gravitational potential differences from satellite-to-satellite tracking, Celes. Mech. Dyn. Astron. 75, 85-100.

Kang, E., B. Tapley, S. Bettedpur, J. Ries, P. Nagel, P. Paster (2005), Precise orbit determination for GRACE using GPS data, GRACE Science Team Meeting, Austin, Texas, Oct. 2005.

Kim, J.R. (2000), Simulation Study of A Low-Low Satellite-to-Satellite Tracking Mission, PhD Dissertation, Center for Space Research, The University of Texas at Austin, May 2000.

Kim, J.R., P. Roesset, S. Bettadpur, B. Tapley, and M. Watkins (2001), Error analysis of the Gravity Recovery and Climate Experiment (GRACE), IAG Symposium Series, Vol. 123, M. Sideris (eds), 103–108, Springer-Verlag Berlin Heidelberg.

Kim, J.R. (2005), Evaluation of the KBR simulation model with flight data, GRACE Science Team Meeting, Austin, Texas, Oct. 2005.

Koch, K.-R., and J. Kusche (2002), Regularization of geopotential determination from satellite data by variance components, J. Geodesy, 76:259-268.

Kruzinga, G., W. Bertiger, C. Finch, D. Kuang, L. Romans, M. Watkins, S. Wu, S. Bettadpur, F. Wang (2005), GRACE Level-1 Status, GRACE Science Team Meeting, Austin, Texas, Oct. 2005.

Kusche, J., E.J.O. Schrama (2005), Surface mass redistribution invsersion from global GPS deformation and Gravity Recovery and Climate Experiment (GRACE) gravity data, J. Geophys. Res., 110, B09409, doi:10.10292004B003556.

Lemoine, F., S. Luthcke, D. Rowlands, S. Klosko, D. Chinn, C. Cox (2005), Unique approaches to addressing time-variable gravity from GRACE, GRACE Science Team Meeting, Austin, Texas, Oct. 2005.

Luthcke, S. D. Rowlands, F. Lemoine, S. Klosko, R. Ray, D. Chinn, J. McCarthy, C. Cox (2005), Monthly spherical harmonic gravity solutions from GRACE KBRR data alone, GRACE Science Team Meeting, Austin, Texas, Oct. 2005.

Luthcke, S., D. Rowlands, F. Lemoine, S. Klosko, J. McCarthy, D. Chinn (2006), Greenland and Antarctica ice sheet drainage basin mass change observations from GRACE, AGU Joint Assembly, Baltimore, MD, May 23-26, 2006.

Matsumoto, K., T. Takanezawa and M. Ooe (2000), Ocean tide models developed by assimilating Topex/Poseidon altimeter data into hydronynamical model: A global model and a regional model around Japan, Journal of Oceanography, Vol. 56, pp. 567-581.

Mayer-Gürr, T., K.H. Ilk, A. Eicker, and M. Feuchtinger (2005a), ITG-CHAMP01: A CHAMP gravity field models from short kinematical arcs of a one-year observation period, J. Geodesy, 78 (7-8):462 – 480.

Mayer-Gürr, T., A. Eicker, K.H. Ilk (2005b), ITG-GRACE01s: A GRACE gravity field derived from short arcs of the satellite's orbit, GRACE Science Team Meeting, Austin/Texas, Oct. 2005.

Mayer-Gürr, T., A. Eicker, K.H. Ilk (2006), Gravity field recovery from GRACE-SST data of short arcs; in: Flury, J., et al. (ed.), Observations of the Earth System from Space, Springer/Berlin, pp. 131-148.

McCarthy, D. D., G. Petit (2004), IERS Conventions, Technical Report 32, Frankfurt am Main: Verlag des Bundesamts für Kartographie und Geodäsie, 127 pp., 2004.

O' Keefe, J. (1957), An application of Jacobi's integral to the motion of an Earth satellite, The Astronomical Journal, 62(8):266-267.

Paulson., A. (2006), Inference of the Earth's mantle viscosity from post-glacial rebound, PhD Dissertation, Dept. of Physics, University of Colorado.

Peltier, W. (2004), Global Glacial Isostasy and the Surface of the Ice-Age Earth: The ICE-5G (VM2) Model and GRACE, Invited Paper, Annual Review of Earth and Planetary Science, 32, 111-149.

Ramillien, G., A. Lombard, A. Cazenave, E. Ivins, M. Llubes, F. Remy and R. Biancale (2006), Interannual variations of the mass balance of the Antarctica and Greenland ice sheets from GRACE, Global & Planetary Change, Vol. 53(3), pp.198-208.

Rasmussen, C. E. and C. K. I. Williams (2006), Gaussian Processes for Machine Learning, The MIT Press, Cambridge/MA, USA.

Ray, R. and G. Egbert (2004), The global S1 tide, J. Physical Oceanography, Vol.34(8), pp. 1922-1935.

Ray, R., S. Luthcke, D. Rowlands (2006), Tidal analysis of GRACE intersatellite ranging data, AGU Joint Assembly, Baltimore, MD, May 23-26, 2006.

Reigber, C., Z. King, R. König, and P. Schwintzer (1996), CHAMP: A minisatellite mission for geopotential and atmospheric research, Sprint AGU Meeting, Baltimore, May 1996.

Reigber, Ch., G. Balmino, P. Schwintzer, R. Biancale, A. Bode, J.-M. Lemoine, R. König, S. Loyer, K.-H. Neumayer, J.-C. Marty, F. Barthelmes, F. Perosanz, S. Zhu, (2002), A high-quality global gravity field model from CHAMP GPS tracking data and accelerometry (EIGEN-1S). Geophys. Res. Lett. 29 (14), doi:10.1029/2002GL015064.

Reubelt, T., G. Austen, E. Grafarend (2003), Harmonic analysis of the Earth's gravitational field by means of semi-continuous ephemeris of a low Earth orbiting GPS-tracked satellite. Case study: CHAMP, J. Geodesy, 77(5-6):257-278.

Rodell, M., and J. Famiglietti (1999), Detectibility of variations in continental water storage from satellite observations of the time variable gravity field. Water Resour. Res. 35(9), 2705-2723.

Rodell, M., and J. Famiglietti (2001). An analysis of terrestrial water storage variations in Illinois with implications for the Gravity Recovery and Climate Experiment (GRACE). Water Resour. Res. 37(5), 1327-1339.

Rodell, M., J.L. Chen, H. Kato, J.S. Famiglietti, J. Nigro, C.R. Wilson (2007), Estimating ground water storage changes in the Mississippi river basin (USA) using GRACE, Hydrogeology Journal, Vol.15(1), pp.159-166.

Rowlands, D., S. B. Luthcke, S. M. Klosko, F. G. R. Lemoine, D. S. Chinn, J. J. McCarthy, C. M. Cox, and O. B. Anderson (2005), Resolving mass flux at high spatial and temporal resolution using GRACE intersatellite measurements, Geophys. Res. Lett., 32, L04310, doi:10.1029/2004GL021908.

ESA (1999), Gravity Field and Steady-State Ocean Circulation Explorer, Reports for Mission Selection, The Four Candidate Earth Explorer Core Missions, B. Battrick (editor), SP-1233 (1), 217 pp.

Schaffrin, B., E. Heidenreich, E. Grafarend (1977), A Representation of the Standard Gravity Field, Manuscripta Geodaetica, 2:135-174.

Schaffrin, B. (2007), Minimum MSE adjustment and the optimal Tykhonov-Phillips regularization parameter via reproBIQUUE, J. of Geodesy, in press.

Schmidt, M., O. Fabert, C.K. Shum (2005a), Towards the estimation of a multi-resolution representattion of the gravity field based on spherical wavelets. In: Sansò F (ed.) A Window on the Future of Geodesy. Springer, Berlin, 362–367.

Schmidt, M., J. Kusche, J. van Loon, C.K. Shum, S.C. Han, O. Fabert (2005b), Multi-resolution representation of regional gravity data. In: Jekeli C, Bastos L, Fernandes J (eds.) Gravity, Geoid and Space Missions. Springer, Berlin, 167–172.

Schmidt, M., O. Fabert, C.K. Shum (2005c), On the estimation of a multi-resolution representation of the gravity field based on spherical harmonics and wavelets. Journal of Geodynamics, 39, 512–526.

Schmidt, M., S.C. Han, J. Kusche, L. Sánchez, C.K. Shum (2006), Regional high-resolution spatiotemporal gravity modeling from GRACE data using spherical wavelets. Geophys. Res. Lett., 33, L08403, doi:10.1029/2005GL025509.

Schotman, H., L. Vermeersen (2005), Sensitivity of glacial isostatic adjustment models with shallow low-viscosity earth layers to the ice-load history in relation to the performance of GOCE and GRACE, Earth & Planetary Science Letts., 236, 828–844.

Schotman, H., P.N.A.M. Visser, and L. Vermeersen (2007), High-harmonic gravity signatures related to post-glacial rebound, Dynamic Planet: Monitoring and Understanding a Dynamic Planet with Geodetic and Oceanographic Tools, P. Tregoning and C. Rizos, eds., 103-111.

Schrama, E. (2003), Error characteristics estimated from CHAMP, GRACE and GOCE derived geoids and from satellite altimetry derived mean dynamic topography, Space Sciences Reviews, Vol. 108, 179-193, doi:10.1023/A:1026154720402.

Schrama, E.J.O. and P.N.A.M. Visser (2006), Accuracy assessment of the monthly GRACE geoids based upon a simulation, J. Geodesy, Vol. 81(1):67-80, doi:10.1007s00190-006-0085-1.
Seeber, G. (2003), Satellite Geodesy, Waltere de Gruyter: Berlin/New York, 2nd edition.

Schutz, B., J. Zwally, C. A. Shuman, D. Hancock, J.P. DiMarzio (2005), Overview of the ICESat Mission, Geophys. Res. Lett., 32, L21S01, doi:10.1029/2005GL024009.

Seo, K.W., C.R. Wilson, J. S. Famiglietti, J.L. Chen, M. Rodell (2006), Terrestrial water mass changes from GRACE, Water Resources Research, 42, W05417, doi:10.1029/2005WR004255.

Shum, C.K., S. Han, and K. Matsumoto (2005a), GRACE observed ocean tides underneath large Antarctic ice shelves, Eos Trans. AGU, 86(52), Fall Meet. Suppl., Abstract G33B-0042, San Francisco, December 5-9, 2005.

Shum, C., S. Han and A. Braun (2005b), Spaceborne gravity sensors for continental hydrology and geodynamic studies, Korean Journal of Remote Sensing, 21(1), 51–57.

Shum, C., S. Han, C. Kuo (2006a), Coseismic deformation studies using GRACE and GOCE, 3rd International GOCE Workshop, ESA ESRIN, Frascati, Italy, Nov. 2006.

Shum, C.K., S.C. Han, C.Y. Kuo, C. Jekeli and T.J. Zhang (2006b), Observing mass redistribution of the Earth using GRACE, Eos Trans, AGU 87(36), Western Pacific Geophysical Meeting (WPGM) Suppl., Abstract G32A-06, Beijing, China, July 2006.

Simpson, J., R.F. Adler, and G..R. North (1988), A proposed Tropical Rainfall Measuring Mission (TRMM) satellite, Bull. Amer. Meteor. Soc., 69, 278-295.

Song, Y. T., and V. Zlotnicki (2004), Ocean bottom pressure waves predicted in the tropical Pacific, Geophys. Res. Lett., 31, L05306, doi:10.1029/2003GL018980.

Swenson, S., and J. Wahr (2002), Methods for inferring regional surface-mass anomalies from Gravity Recovery and Climate Experiment (GRACE) measurements of time-variable gravity, J. Geophys. Res., 107(B9), 2193, doi:10.1029/2001JB000576.

Swenson, S., and J. Wahr (2006), Post-processing removal of correlated errors in GRACE data, Geophys. Res. Lett., 33, L08402, doi:10.1029/2005GL025285.

Tapley, B.D., S. Bettadpur, M. Watkins, and C. Reigber (2004a), The gravity recovery and climate experiment: Mission overview and early results, Geophys. Res. Lett., 31, L09607, doi:10.1029/2004GL019920.

Tapley, B.D., S. Bettadpur, J. Ries, P. Thompson, and M. Watkins (2004b), GRACE measurements of mass variability in the Earth system, Science, 305, 503-505.

Thompson, P.F., S.. Bettadpur, and B. Tapley (2004), Impact of short period, non-tidal, temporal mass variability on GRACE gravity estimates, Geophys. Res. Lett., 31, L06619, doi:10.1029/2003GL019285.

Velicogna I., and J. Wahr (2001), Can surface pressure be used to remove atmospheric contributions from GRACE data with sufficient accuracy to recover hydrological signals?, J. Geophysical Research, 106(B8), pp. 16,415-16,434.

Velicogna, I., and J. Wahr (2006a), Measurements of time-variable gravity show mass loss in Antarctica, Science, 311,1754-1756.

Velicogna, I., and J. Wahr (2006b), Acceleration of Greenland ice mass loss in spring 2004, Nature, 443, doi:10.1038/nature05168.

Visser, P.N.A.M., N. Sneeuw, and C. Gerlach (2003), Energy integral method for gravity field determination from satellite orbit coordinates, J. Geodesy, 77 (3-4):207-216.

Wahr, J., F. Molenaar, and F. Bryan (1998), Time variability of the Earth's gravity field: Hydrological and oceanic effects and their possible detection using GRACE, J. Geophys. Res., 103(B12), pp. 30,205-30,229.

Wahr, J., S. Swenson, V. Zlotnicki, and I. Velicogna (2004), Time variable gravity from GRACE: First results, Geophys. Res. Lett., 31, L11501, doi:10.1029/2004GL019779.

Watkins, M., S. Bettadpur, D. Chambers, F. Flechtner, R. Schmidt, S. Swenson, D. Yuan, J. Wahr, V. Zlotnicki (2005), Evaluation of GRACE mission, GRACE Science Team Meeting, Austin, Texas, Oct. 2005.

Wu, S.-C., G. Kruizinga, W. Bertiger (2004), Algorithm theoretical basis document for GRACE Level-1B data processing (GRACE 327-741), JPL, California Institute of Technology/CA, Feb. 2004.

Wu, P. (2006), Sensitivity of relative sea levels and crustal velocities in Laurentide to radial and lateral viscosity variations in the mantle, Geophys. J. Int., 165, 401-413, doi: 10.1111/j.1365-246X.2006.02960.x.

Yuan, D., D. Kuang, and M. Watkins (2004), Verification of GRACE gravity solutions, Proc. Joint CHAMP/GRACE Meeting, GFZ Potsdam, July 2004.

Yuan, D. and M. Watkins (2005), Status of JPL L2 verification solution for RL02, GRACE Science Team Meeting, Austin, Texas, Oct. 2005.

Yuan, D. and M. Watkins (2006), Recent Mascon Solutions from GRACE, presented at the VI Hotine-Marussi International Symposium, Wuhan/China, May29-June 2, 2006.

Zlotnicki V., J. Wahr, I. Fukumori and Y.T. Song (2006), Antarctic Circumpolar Current transport variability during 2003-2005 from GRACE, J. Physical Oceanog., Vol. 37(2):230-244.

APPENDIX A

RANGE, RANGE RATE AND RANGE ACCELERATION

Let $\mathbf{r}_1$ and $\mathbf{r}_2$ represent the position vectors of the two satellites, and ρ_{12} represents the range between the two satellites. We then have,

$$\rho_{12}^2 = \mathbf{r}_{12} \cdot \mathbf{r}_{12}, \tag{A.1}$$

where $\mathbf{r}_{12} = \mathbf{r}_2 - \mathbf{r}_1$.

Taking the time-derivative, we have,

$$2\rho_{12}\dot{\rho}_{12} = \dot{\mathbf{r}}_{12} \cdot \mathbf{r}_{12} + \mathbf{r}_{12} \cdot \dot{\mathbf{r}}_{12} = 2\mathbf{r}_{12} \cdot \dot{\mathbf{r}}_{12}, \tag{A.2}$$

$$\dot{\rho}_{12} = \dot{\mathbf{r}}_{12} \cdot \frac{\mathbf{r}_{12}}{\rho_{12}} = \dot{\mathbf{r}}_{12} \cdot \mathbf{e}_{12}, \tag{A.3}$$

where $\mathbf{e}_{12} = \dfrac{\mathbf{r}_{12}}{\rho_{12}}$.

Taking derivative again,

$$\ddot{\rho}_{12} = \ddot{\mathbf{r}}_{12} \cdot \mathbf{e}_{12} + \dot{\mathbf{r}}_{12} \cdot \dot{\mathbf{e}}_{12}, \tag{A.4}$$

where $\dot{\mathbf{e}}_{12} = \dfrac{d}{dt}\left(\dfrac{\mathbf{r}_{12}}{\rho_{12}}\right) = \dfrac{\dot{\mathbf{r}}_{12} - \dot{\rho}_{12}\mathbf{e}_{12}}{\rho_{12}}$.

Thus,

$$\ddot{\rho}_{12} = \ddot{\mathbf{r}}_{12} \cdot \mathbf{e}_{12} + \dot{\mathbf{r}}_{12} \cdot \frac{\dot{\mathbf{r}}_{12} - \dot{\rho}_{12}\mathbf{e}_{12}}{\rho_{12}} = \ddot{\mathbf{r}}_{12} \cdot \mathbf{e}_{12} + \frac{\left|\dot{\mathbf{r}}_{12}\right|^2 - \dot{\rho}_{12}^2}{\rho_{12}}. \tag{A.5}$$

In the inertial frame we have,

$$\ddot{\mathbf{r}}_1 = \mathbf{g}_1 + \mathbf{a}_1, \tag{A.6}$$

$$\ddot{\mathbf{r}}_2 = \mathbf{g}_2 + \mathbf{a}_2, \tag{A.7}$$

So by taking the difference, we have,

$$\ddot{\mathbf{r}}_{12} = \mathbf{g}_{12} + \mathbf{a}_{12}. \tag{A.8}$$

Finally, we have,

$$\begin{aligned} \ddot{\rho}_{12} &= (\mathbf{g}_{12} + \mathbf{a}_{12}) \cdot \mathbf{e}_{12} + \frac{\left|\dot{\mathbf{r}}_{12}\right|^2 - \dot{\rho}_{12}^2}{\rho_{12}} \\ &= (\mathbf{g}_2 - \mathbf{g}_1) \cdot \mathbf{e}_{12} + (\mathbf{a}_2 - \mathbf{a}_1) \cdot \mathbf{e}_{12} + \frac{\left|\dot{\mathbf{r}}_{12}\right|^2 - \dot{\rho}_{12}^2}{\rho_{12}} \end{aligned}. \tag{A.9}$$

APPENDIX B

FORMULA FOR USING *IN SITU* LOS GRAVITY DIFFERENCE TO ESTIMATE SPHERICAL HARMONIC COEFFICIENTS

From Appendix A, we have,

$$\ddot{\mathbf{r}}_{12} \cdot \mathbf{e}_{12} = \ddot{\rho}_{12} - \frac{\left|\dot{\mathbf{r}}_{12}\right|^2 - \dot{\rho}_{12}^2}{\rho_{12}}. \tag{B.1}$$

In the inertial frame, the following holds,

$$\ddot{\mathbf{r}}^i = \mathbf{g}^i + \mathbf{a}^i. \tag{B.2}$$

So in the inertial frame,

$$\mathbf{g}_{12}^i \cdot \mathbf{e}_{12}^i = \ddot{\mathbf{r}}_{12}^i \cdot \mathbf{e}_{12}^i - \mathbf{a}_{12}^i \cdot \mathbf{e}_{12}^i, \tag{B.3}$$

where, $\mathbf{g}_{12}^i = \mathbf{g}_2^i - \mathbf{g}_1^i$, $\mathbf{a}_{12}^i = \mathbf{a}_{12}^i - \mathbf{a}_{12}^i$ and $\mathbf{e}_{12}^i = \dfrac{\mathbf{r}_{12}^i}{\left|\mathbf{r}_{12}^i\right|}$.

Thus,

$$\mathbf{g}_{12}^i \cdot \mathbf{e}_{12}^i = \ddot{\rho}_{12} - \frac{\left|\dot{\mathbf{r}}_{12}^i\right|^2 - \dot{\rho}_{12}^2}{\rho_{12}} - \mathbf{a}_{12}^i \cdot \mathbf{e}_{12}^i. \tag{B.4}$$

A commonly used procedure to represent the Earth's gravitational potential $V(r,\theta,\lambda)$ is the expansion into a series of spherical harmonics:

$$V(r,\theta,\lambda) = \frac{GM}{R}\sum_{n=0}^{N_{\max}}\sum_{m=0}^{n}\left(\frac{R}{r}\right)^{n+1}\left(C_{nm}\cos(m\lambda) + S_{nm}\sin(m\lambda)\right)\overline{P}_{nm}(\cos\theta), \tag{B.5}$$

where, r,θ,λ are the spherical coordinates (θ is co-latitude); G is the universal gravitational constant; M is the mass of the Earth; R is the mean radius of the Earth; C_{nm}, S_{nm} are the spherical harmonic coefficients; and $\overline{P}_{nm}(\cos\theta)$ are the fully normalized Legendre functions.

Assume that we have a reference geopotential, V_0, and

$$V = V_0 + T. \tag{B.6}$$

We define the disturbing potential or the residual potential as

$$T(r,\theta,\lambda) = \frac{GM}{R}\sum_{n=0}^{N_{\max}}\sum_{m=0}^{n}\left(\frac{R}{r}\right)^{n+1}\left(\Delta C_{nm}\cos(m\lambda) + \Delta S_{nm}\sin(m\lambda)\right)\overline{P}_{nm}(\cos\theta), \tag{B.7}$$

where $\left(\Delta C_{nm} \quad \Delta S_{nm}\right)$ are what we want to estimate.

The derivatives of the residual potential with respect to spherical coordinates are:

$$\begin{cases} \dfrac{\partial T}{\partial \theta} = -\dfrac{GM}{R}\displaystyle\sum_{n=0}^{N_{\max}}\sum_{m=0}^{n}\left(\frac{R}{r}\right)^{n+1}\left(\cos(m\lambda)\Delta C_{nm} + \sin(m\lambda)\Delta S_{nm}\right)\overline{P}'_{nm}(\cos\theta)\sin\theta \\ \dfrac{\partial T}{\partial \lambda} = \dfrac{GM}{R}\displaystyle\sum_{n=0}^{N_{\max}}\sum_{m=0}^{n}\left(\frac{R}{r}\right)^{n+1} m\left(-\sin(m\lambda)\Delta C_{nm} + \cos(m\lambda)\Delta S_{nm}\right)\overline{P}_{nm}(\cos\theta) \\ \dfrac{\partial T}{\partial r} = -\dfrac{GM}{R^2}\displaystyle\sum_{n=0}^{N_{\max}}\sum_{m=0}^{n}(n+1)\left(\frac{R}{r}\right)^{n+2}\left(\cos(m\lambda)\Delta C_{nm} + \sin(m\lambda)\Delta S_{nm}\right)\overline{P}_{nm}(\cos\theta) \end{cases}. \tag{B.8}$$

If we express $\mathbf{g}$ in cartesian coordinates, i.e., $\mathbf{g} = \begin{pmatrix} g_x & g_y & g_z \end{pmatrix}^T$. And now let's use the navigation frame, namely North-East-Down (NED) frame,

$$\mathbf{g}^n = \begin{pmatrix} -\frac{1}{r}\frac{\partial T}{\partial \theta} \\ \frac{1}{r\sin\theta}\frac{\partial T}{\partial \lambda} \\ -\frac{\partial T}{\partial r} \end{pmatrix}. \tag{B.9}$$

In (B.9) $\mathbf{g}^n$ is actually the residual acceleration vector after introducing the reference geopotential, V_0, but for the purpose of simplicity it will still be denoted by $\mathbf{g}^n$.

Since we have,

$$\begin{aligned} \mathbf{g}_{12}^i &= \mathbf{g}_{12}^i - \mathbf{g}_{12}^i \\ &= \mathbf{C}_{n,2}^i \mathbf{g}_2^n - \mathbf{C}_{n,1}^i \mathbf{g}_1^n \\ &= \mathbf{C}_{n,2}^i \cdot \mathbf{g}_2^n - \mathbf{C}_{n,1}^i \cdot \mathbf{g}_1^n \end{aligned}, \tag{B.10}$$

then,

$$\begin{aligned} \mathbf{g}_{12}^i \cdot \mathbf{e}_{12}^i &= \mathbf{C}_{n,2}^i \cdot \mathbf{g}_2^n \cdot \mathbf{e}_{12}^i - \mathbf{C}_{n,1}^i \cdot \mathbf{g}_1^n \cdot \mathbf{e}_{12}^i \\ &= (\mathbf{C}_{n,2}^i)^T \cdot \mathbf{e}_{12}^i \cdot \mathbf{g}_2^n - (\mathbf{C}_{n,1}^i)^T \cdot \mathbf{e}_{12}^i \cdot \mathbf{g}_1^n \\ &= (\mathbf{C}_{i,2}^n \cdot \mathbf{e}_{12}^i) \cdot \mathbf{g}_2^n - (\mathbf{C}_{i,1}^{ni} \cdot \mathbf{e}_{12}^i) \cdot \mathbf{g}_1^n \\ &= \mathbf{b}_{i,2}^n \cdot \mathbf{g}_2^n - \mathbf{b}_{i,1}^n \cdot \mathbf{g}_1^n \end{aligned}, \tag{B.11}$$

Where $\mathbf{b}_{i,2}^n := (\mathbf{C}_{i,2}^n \cdot \mathbf{e}_{12})$ and $\mathbf{b}_{i,1}^n := (\mathbf{C}_{i,1}^n \cdot \mathbf{e}_{12})$.

Let's express the three components of $\mathbf{g}^n$ using the spherical harmonic coefficients,

$$\begin{aligned} -\frac{1}{r}\frac{\partial T}{\partial \theta} &= \frac{1}{r}\frac{GM}{R}\sum_{n=0}^{N_{\max}}\sum_{m=0}^{n}(\frac{R}{r})^{n+1}(\cos(m\lambda)\Delta C_{nm} + \sin(m\lambda)\Delta S_{nm})\overline{P}_{nm}'(\cos\theta)\sin\theta \\ &= \frac{GM}{R^2}\sum_{n=0}^{N_{\max}}\sum_{m=0}^{n}(\frac{R}{r})^{n+2}(\cos(m\lambda)\Delta C_{nm} + \sin(m\lambda)\Delta S_{nm})\overline{P}_{nm}'(\cos\theta)\sin\theta \end{aligned}, \tag{B.12}$$

$$\frac{1}{r\sin\theta}\frac{\partial T}{\partial \lambda} = \frac{GM}{R^2}\sum_{n=0}^{N_{\max}}\sum_{m=0}^{n}(\frac{R}{r})^{n+2} m(-\sin(m\lambda)\Delta C_{nm} + \cos(m\lambda)\Delta S_{nm})\overline{P}_{nm}(\cos\theta)\frac{1}{\sin\theta} \tag{B.13}$$

$$-\frac{\partial T}{\partial r} = \frac{GM}{R^2}\sum_{n=0}^{N_{\max}}\sum_{m=0}^{n}(n+1)(\frac{R}{r})^{n+2}(\cos(m\lambda)\Delta C_{nm} + \sin(m\lambda)\Delta S_{nm})\overline{P}_{nm}(\cos\theta). \tag{B.14}$$

Define

$$\mathbf{b}_{i,2}^{n} = \begin{pmatrix} b_{2,x} \\ b_{2,y} \\ b_{2,z} \end{pmatrix}, \tag{B.15}$$

$$\mathbf{b}_{i,1}^{n} = \begin{pmatrix} b_{1,x} \\ b_{1,y} \\ b_{1,z} \end{pmatrix}. \tag{B.16}$$

So,

$$\mathbf{b}_{i,2}^{n} \cdot \mathbf{g}_{2}^{n} = b_{2,x}\left(-\frac{1}{r_2}\frac{\partial T}{\partial \theta_2}\right) + b_{2,y}\left(\frac{1}{r_2 \sin\theta_2}\frac{\partial T}{\partial \lambda_2}\right) + b_{2,z}\left(-\frac{\partial T}{\partial r_2}\right), \tag{B.17}$$

$$\mathbf{b}_{i,1}^{n} \cdot \mathbf{g}_{1}^{n} = b_{1,x}\left(-\frac{1}{r_1}\frac{\partial T}{\partial \theta_1}\right) + b_{1,y}\left(\frac{1}{r_1 \sin\theta_1}\frac{\partial T}{\partial \lambda_1}\right) + b_{1,z}\left(-\frac{\partial T}{\partial r_1}\right), \tag{B.18}$$

$$\begin{aligned} \mathbf{b}_{i,2}^{n} \cdot \mathbf{g}_{2}^{n} - \mathbf{b}_{i,1}^{n} \cdot \mathbf{g}_{1}^{n} = {} & b_{2,x}\left(-\frac{1}{r_2}\frac{\partial T}{\partial \theta_2}\right) + b_{2,y}\left(\frac{1}{r_2 \sin\theta_2}\frac{\partial T}{\partial \lambda_2}\right) + b_{2,z}\left(-\frac{\partial T}{\partial r_2}\right) - \\ & - b_{1,x}\left(-\frac{1}{r_1}\frac{\partial T}{\partial \theta_1}\right) - b_{1,y}\left(\frac{1}{r_1 \sin\theta_1}\frac{\partial T}{\partial \lambda_1}\right) - b_{1,z}\left(-\frac{\partial T}{\partial r_1}\right) \end{aligned}, \tag{B.19}$$

$$\begin{aligned} \mathbf{b}_{i,2}^{n} \cdot \mathbf{g}_{2}^{n} - \mathbf{b}_{i,1}^{n} \cdot \mathbf{g}_{1}^{n} = {} & b_{2,x}\left(-\frac{1}{r_2}\frac{\partial T}{\partial \theta_2}\right) - b_{1,x}\left(-\frac{1}{r_1}\frac{\partial T}{\partial \theta_1}\right) \\ & + b_{2,y}\left(\frac{1}{r_2 \sin\theta_2}\frac{\partial T}{\partial \lambda_2}\right) - b_{1,y}\left(\frac{1}{r_1 \sin\theta_1}\frac{\partial T}{\partial \lambda_1}\right) \\ & + b_{2,z}\left(-\frac{\partial T}{\partial r_2}\right) - b_{1,z}\left(-\frac{\partial T}{\partial r_1}\right) \end{aligned}. \tag{B.20}$$

First

$$b_{2,x}\left(-\frac{1}{r_2}\frac{\partial T}{\partial \theta_2}\right) = b_{2,x}\frac{GM}{R^2}\sum_{n=0}^{N_{\max}}\sum_{m=0}^{n}\left(\frac{R}{r_2}\right)^{n+2}\left(\cos(m\lambda_2)\Delta C_{nm} + \sin(m\lambda_2)\Delta S_{nm}\right)\overline{P}'_{nm}(\cos\theta_2)\sin\theta_2, \tag{B.21}$$

$$b_{1,x}\left(-\frac{1}{r_1}\frac{\partial T}{\partial \theta_1}\right) = b_{1,x}\frac{GM}{R^2}\sum_{n=0}^{N_{\max}}\sum_{m=0}^{n}\left(\frac{R}{r_1}\right)^{n+2}\left(\cos(m\lambda_1)\Delta C_{nm} + \sin(m\lambda_1)\Delta S_{nm}\right)\overline{P}'_{nm}(\cos\theta_1)\sin\theta_1, \tag{B.22}$$

$$b_{2,x}(-\frac{1}{r_2}\frac{\partial T}{\partial \theta_2}) - b_{1,x}(-\frac{1}{r_1}\frac{\partial T}{\partial \theta_1}) =$$

$$b_{2,x}\frac{GM}{R^2}\sum_{n=0}^{N_{\max}}\sum_{m=0}^{n}(\frac{R}{r_2})^{n+2}(\cos(m\lambda_2)\Delta C_{nm} + \sin(m\lambda_2)\Delta S_{nm})\overline{P}'_{nm}(\cos\theta_2)\sin\theta_2 -$$

$$b_{1,x}\frac{GM}{R^2}\sum_{n=0}^{N_{\max}}\sum_{m=0}^{n}(\frac{R}{r_1})^{n+2}(\cos(m\lambda_1)\Delta C_{nm} + \sin(m\lambda_1)\Delta S_{nm})\overline{P}'_{nm}(\cos\theta_1)\sin\theta_1$$

=

$$\frac{GM}{R^2}\sum_{n=0}^{N_{\max}}\sum_{m=0}^{n}(b_{2,x}(\frac{R}{r_2})^{n+2}\cos(m\lambda_2)\overline{P}'_{nm}(\cos\theta_2)\sin\theta_2 -$$

$$b_{1,x}(\frac{R}{r_1})^{n+2}\cos(m\lambda_1)\overline{P}'_{nm}(\cos\theta_1)\sin\theta_1)\Delta C_{nm} +$$

$$\frac{GM}{R^2}\sum_{n=0}^{N_{\max}}\sum_{m=0}^{n}(b_{2,x}(\frac{R}{r_2})^{n+2}\sin(m\lambda_2)\overline{P}'_{nm}(\cos\theta_2)\sin\theta_2 -$$

$$b_{1,x}(\frac{R}{r_1})^{n+2}\sin(m\lambda_1)\overline{P}'_{nm}(\cos\theta_1)\sin\theta_1)\Delta S_{nm} \qquad .(B.23)$$

Second,

$$b_{2,y}\frac{1}{r_2\sin\theta_2}\frac{\partial T}{\partial \lambda_2} = b_{2,y}\frac{GM}{R^2}\sum_{n=0}^{N_{\max}}\sum_{m=0}^{n}(\frac{R}{r_2})^{n+2}m(-\sin(m\lambda_2)\Delta C_{nm} + \cos(m\lambda_2)\Delta S_{nm})\overline{P}_{nm}(\cos\theta_2)\frac{1}{\sin\theta_2}, \quad (B.24)$$

$$b_{1,y}\frac{1}{r_1\sin\theta_1}\frac{\partial T}{\partial \lambda_1} = b_{1,y}\frac{GM}{R^2}\sum_{n=0}^{N_{\max}}\sum_{m=0}^{n}(\frac{R}{r_1})^{n+2}m(-\sin(m\lambda_1)\Delta C_{nm} + \cos(m\lambda_1)\Delta S_{nm})\overline{P}_{nm}(\cos\theta_1)\frac{1}{\sin\theta_1}, \quad (B.25)$$

$$b_{2,y}\left(\frac{1}{r_2 \sin\theta_2}\frac{\partial T}{\partial \lambda_2}\right) - b_{1,y}\left(\frac{1}{r_1 \sin\theta_1}\frac{\partial T}{\partial \lambda_1}\right) =$$

$$b_{2,y}\frac{GM}{R^2}\sum_{n=0}^{N_{\max}}\sum_{m=0}^{n}\left(\frac{R}{r_2}\right)^{n+2} m\left(-\sin(m\lambda_2)\Delta C_{nm} + \cos(m\lambda_2)\Delta S_{nm}\right)\overline{P}_{nm}(\cos\theta_2)\frac{1}{\sin\theta_2} -$$

$$b_{1,y}\frac{GM}{R^2}\sum_{n=0}^{N_{\max}}\sum_{m=0}^{n}\left(\frac{R}{r_1}\right)^{n+2} m\left(-\sin(m\lambda_1)\Delta C_{nm} + \cos(m\lambda_1)\Delta S_{nm}\right)\overline{P}_{nm}(\cos\theta_1)\frac{1}{\sin\theta_1}$$

$$=$$

$$\frac{GM}{R^2}\sum_{n=0}^{N_{\max}}\sum_{m=0}^{n}\left(-mb_{2,y}\left(\frac{R}{r_2}\right)^{n+2}\sin(m\lambda_2)\overline{P}_{nm}(\cos\theta_2)\frac{1}{\sin\theta_2} + mb_{1,y}\left(\frac{R}{r_1}\right)^{n+2}\sin(m\lambda_1)\overline{P}_{nm}(\cos\theta_1)\frac{1}{\sin\theta_1}\right)\Delta C_{nm} +$$

$$\frac{GM}{R^2}\sum_{n=0}^{N_{\max}}\sum_{m=0}^{n}\left(mb_{2,y}\left(\frac{R}{r_2}\right)^{n+2}\cos(m\lambda_2)\overline{P}_{nm}(\cos\theta_2)\frac{1}{\sin\theta_2} - mb_{1,y}\left(\frac{R}{r_1}\right)^{n+2}\cos(m\lambda_1)\overline{P}_{nm}(\cos\theta_1)\frac{1}{\sin\theta_1}\right)\Delta S_{nm} \qquad \text{(B.26)}$$

Third,

$$b_{2,z}\left(-\frac{\partial T}{\partial r_2}\right) = b_{2,z}\frac{GM}{R^2}\sum_{n=0}^{N_{\max}}\sum_{m=0}^{n}(n+1)\left(\frac{R}{r_2}\right)^{n+2}\left(\cos(m\lambda_2)\Delta C_{nm} + \sin(m\lambda_2)\Delta S_{nm}\right)\overline{P}_{nm}(\cos\theta_2), \qquad \text{(B.27)}$$

$$b_{1,z}\left(-\frac{\partial T}{\partial r_1}\right) = b_{1,z}\frac{GM}{R^2}\sum_{n=0}^{N_{\max}}\sum_{m=0}^{n}(n+1)\left(\frac{R}{r_1}\right)^{n+2}\left(\cos(m\lambda_1)\Delta C_{nm} + \sin(m\lambda_1)\Delta S_{nm}\right)\overline{P}_{nm}(\cos\theta_1), \qquad \text{(B.28)}$$

$$b_{2,z}(-\frac{\partial T}{\partial r_2}) - b_{1,z}(-\frac{\partial T}{\partial r_1}) =$$

$$b_{2,z}\frac{GM}{R^2}\sum_{n=0}^{N_{\max}}\sum_{m=0}^{n}(n+1)(\frac{R}{r_2})^{n+2}(\cos(m\lambda_2)\Delta C_{nm} + \sin(m\lambda_2)\Delta S_{nm})\overline{P}_{nm}(\cos\theta_2) -$$

$$b_{1,z}\frac{GM}{R^2}\sum_{n=0}^{N_{\max}}\sum_{m=0}^{n}(n+1)(\frac{R}{r_1})^{n+2}(\cos(m\lambda_1)\Delta C_{nm} + \sin(m\lambda_1)\Delta S_{nm})\overline{P}_{nm}(\cos\theta_1)$$

$$=$$

$$\frac{GM}{R^2}\sum_{n=0}^{N_{\max}}\sum_{m=0}^{n}(b_{2,z}(n+1)(\frac{R}{r_2})^{n+2}\cos(m\lambda_2)\overline{P}_{nm}(\cos\theta_2) -$$

$$b_{1,z}(n+1)(\frac{R}{r_1})^{n+2}\cos(m\lambda_1)\overline{P}_{nm}(\cos\theta_1))\Delta C_{nm} +$$

$$\frac{GM}{R^2}\sum_{n=0}^{N_{\max}}\sum_{m=0}^{n}(b_{2,z}(n+1)(\frac{R}{r_2})^{n+2}\sin(m\lambda_2)\overline{P}_{nm}(\cos\theta_2) -$$

$$b_{1,z}(n+1)(\frac{R}{r_1})^{n+2}\sin(m\lambda_1)\overline{P}_{nm}(\cos\theta_1))\Delta S_{nm} \qquad \text{(B.29)}$$

Then we put (B.23), (B.26) and (B.29) them together,

$$
\begin{aligned}
&\mathbf{b}_{i,2}^{n}\cdot\mathbf{g}_{2}^{n}-\mathbf{b}_{i,1}^{n}\cdot\mathbf{g}_{1}^{n}= \\
&\frac{GM}{R^{2}}\sum_{n=0}^{N_{\max}}\sum_{m=0}^{n}(b_{2,x}(\frac{R}{r_{2}})^{n+2}\cos(m\lambda_{2})\overline{P}_{nm}^{'}(\cos\theta_{2})\sin\theta_{2}- \\
&\qquad b_{1,x}(\frac{R}{r_{1}})^{n+2}\cos(m\lambda_{1})\overline{P}_{nm}^{'}(\cos\theta_{1})\sin\theta_{1})\Delta C_{nm} \\
&+\frac{GM}{R^{2}}\sum_{n=0}^{N_{\max}}\sum_{m=0}^{n}(b_{2,x}(\frac{R}{r_{2}})^{n+2}\sin(m\lambda_{2})\overline{P}_{nm}^{'}(\cos\theta_{2})\sin\theta_{2}- \\
&\qquad b_{1,x}(\frac{R}{r_{1}})^{n+2}\sin(m\lambda_{1})\overline{P}_{nm}^{'}(\cos\theta_{1})\sin\theta_{1})\Delta S_{nm} \\
&+\frac{GM}{R^{2}}\sum_{n=0}^{N_{\max}}\sum_{m=0}^{n}(-mb_{2,y}(\frac{R}{r_{2}})^{n+2}\sin(m\lambda_{2})\overline{P}_{nm}(\cos\theta_{2})\frac{1}{\sin\theta_{2}}+ \\
&\qquad mb_{1,y}(\frac{R}{r_{1}})^{n+2}\sin(m\lambda_{1})\overline{P}_{nm}(\cos\theta_{1})\frac{1}{\sin\theta_{1}})\Delta C_{nm} \\
&+\frac{GM}{R^{2}}\sum_{n=0}^{N_{\max}}\sum_{m=0}^{n}(mb_{2,y}(\frac{R}{r_{2}})^{n+2}\cos(m\lambda_{2})\overline{P}_{nm}(\cos\theta_{2})\frac{1}{\sin\theta_{2}}- \\
&\qquad mb_{1,y}(\frac{R}{r_{1}})^{n+2}\cos(m\lambda_{1})\overline{P}_{nm}(\cos\theta_{1})\frac{1}{\sin\theta_{1}})\Delta S \\
&+\frac{GM}{R^{2}}\sum_{n=0}^{N_{\max}}\sum_{m=0}^{n}(b_{2,z}(n+1)(\frac{R}{r_{2}})^{n+2}\cos(m\lambda_{2})\overline{P}_{nm}(\cos\theta_{2})- \\
&\qquad b_{1,z}(n+1)(\frac{R}{r_{1}})^{n+2}\cos(m\lambda_{1})\overline{P}_{nm}(\cos\theta_{1}))\Delta C_{nm} \\
&+\frac{GM}{R^{2}}\sum_{n=0}^{N_{\max}}\sum_{m=0}^{n}(b_{2,z}(n+1)(\frac{R}{r_{2}})^{n+2}\sin(m\lambda_{2})\overline{P}_{nm}(\cos\theta_{2})- \\
&\qquad b_{1,z}(n+1)(\frac{R}{r_{1}})^{n+2}\sin(m\lambda_{1})\overline{P}_{nm}(\cos\theta_{1}))\Delta S_{nm}
\end{aligned}
\tag{B.30}
$$

$$\mathbf{g}_{12}^{i} \cdot \mathbf{e}_{12}^{i} =$$
$$\mathbf{b}_{i,2}^{n} \cdot \mathbf{g}_{2}^{n} - \mathbf{b}_{i,1}^{n} \cdot \mathbf{g}_{1}^{n}$$
$$=$$
$$\frac{GM}{R^2} \sum_{n=0}^{N_{\max}} \sum_{m=0}^{n} ((b_{2,x} (\frac{R}{r_2})^{n+2} \cos(m\lambda_2) \overline{P}_{nm}^{'} (\cos\theta_2) \sin\theta_2 -$$
$$b_{1,x} (\frac{R}{r_1})^{n+2} \cos(m\lambda_1) \overline{P}_{nm}^{'} (\cos\theta_1) \sin\theta_1) +$$
$$(-mb_{2,y} (\frac{R}{r_2})^{n+2} \sin(m\lambda_2) \overline{P}_{nm} (\cos\theta_2) \frac{1}{\sin\theta_2} + mb_{1,y} (\frac{R}{r_1})^{n+2} \sin(m\lambda_1) \overline{P}_{nm} (\cos\theta_1) \frac{1}{\sin\theta_1}) +$$
$$(b_{2,z} (n+1) (\frac{R}{r_2})^{n+2} \cos(m\lambda_2) \overline{P}_{nm} (\cos\theta_2) - b_{1,z} (n+1) (\frac{R}{r_1})^{n+2} \cos(m\lambda_1) \overline{P}_{nm} (\cos\theta_1))) \Delta C_{nm} +$$
$$(b_{2,x} (\frac{R}{r_2})^{n+2} \sin(m\lambda_2) \overline{P}_{nm}^{'} (\cos\theta_2) \sin\theta_2 - b_{1,x} (\frac{R}{r_1})^{n+2} \sin(m\lambda_1) \overline{P}_{nm}^{'} (\cos\theta_1) \sin\theta_1) +$$
$$(mb_{2,y} (\frac{R}{r_2})^{n+2} \cos(m\lambda_2) \overline{P}_{nm} (\cos\theta_2) \frac{1}{\sin\theta_2} - mb_{1,y} (\frac{R}{r_1})^{n+2} \cos(m\lambda_1) \overline{P}_{nm} (\cos\theta_1) \frac{1}{\sin\theta_1}) +$$
$$(b_{2,z} (n+1) (\frac{R}{r_2})^{n+2} \sin(m\lambda_2) \overline{P}_{nm} (\cos\theta_2) - b_{1,z} (n+1) (\frac{R}{r_1})^{n+2} \sin(m\lambda_1) \overline{P}_{nm} (\cos\theta_1))) \Delta S_{nm} \tag{B.31}$$

Equation (B.31) connects the observable $\mathbf{g}_{12}^{i} \cdot \mathbf{e}_{12}^{i}$ to the coefficients, ΔC_{nm} and ΔS_{nm}.

$$\mathbf{b}_{i,2}^{n} \cdot \mathbf{g}_{2}^{n} - \mathbf{b}_{i,1}^{n} \cdot \mathbf{g}_{1}^{n} =$$

$$\frac{GM}{R^2} \sum_{n=0}^{N_{\max}} \sum_{m=0}^{n} (b_{2,x} (\frac{R}{r_2})^{n+2} \cos(m\lambda_2) \overline{P}_{nm}^{'} (\cos\theta_2) \sin\theta_2 -$$

$$b_{1,x} (\frac{R}{r_1})^{n+2} \cos(m\lambda_1) \overline{P}_{nm}^{'} (\cos\theta_1) \sin\theta_1) \Delta C_{nm}$$

$$+ \frac{GM}{R^2} \sum_{n=0}^{N_{\max}} \sum_{m=0}^{n} (-m b_{2,y} (\frac{R}{r_2})^{n+2} \sin(m\lambda_2) \overline{P}_{nm} (\cos\theta_2) \frac{1}{\sin\theta_2} +$$

$$m b_{1,y} (\frac{R}{r_1})^{n+2} \sin(m\lambda_1) \overline{P}_{nm} (\cos\theta_1) \frac{1}{\sin\theta_1}) \Delta C_{nm}$$

$$+ \frac{GM}{R^2} \sum_{n=0}^{N_{\max}} \sum_{m=0}^{n} (b_{2,z} (n+1) (\frac{R}{r_2})^{n+2} \cos(m\lambda_2) \overline{P}_{nm} (\cos\theta_2) -$$

$$b_{1,z} (n+1) (\frac{R}{r_1})^{n+2} \cos(m\lambda_1) \overline{P}_{nm} (\cos\theta_1)) \Delta C_{nm}$$

$$+ \frac{GM}{R^2} \sum_{n=0}^{N_{\max}} \sum_{m=0}^{n} (b_{2,x} (\frac{R}{r_2})^{n+2} \sin(m\lambda_2) \overline{P}_{nm}^{'} (\cos\theta_2) \sin\theta_2 -$$

$$b_{1,x} (\frac{R}{r_1})^{n+2} \sin(m\lambda_1) \overline{P}_{nm}^{'} (\cos\theta_1) \sin\theta_1) \Delta S_{nm}$$

$$+ \frac{GM}{R^2} \sum_{n=0}^{N_{\max}} \sum_{m=0}^{n} (m b_{2,y} (\frac{R}{r_2})^{n+2} \cos(m\lambda_2) \overline{P}_{nm} (\cos\theta_2) \frac{1}{\sin\theta_2} -$$

$$m b_{1,y} (\frac{R}{r_1})^{n+2} \cos(m\lambda_1) \overline{P}_{nm} (\cos\theta_1) \frac{1}{\sin\theta_1}) \Delta S$$

$$+ \frac{GM}{R^2} \sum_{n=0}^{N_{\max}} \sum_{m=0}^{n} (b_{2,z} (n+1) (\frac{R}{r_2})^{n+2} \sin(m\lambda_2) \overline{P}_{nm} (\cos\theta_2) -$$

$$b_{1,z} (n+1) (\frac{R}{r_1})^{n+2} \sin(m\lambda_1) \overline{P}_{nm} (\cos\theta_1)) \Delta S_{nm}$$

.(B.32)

$$\mathbf{b}_{i,2}^{n}\cdot\mathbf{g}_{2}^{n}-\mathbf{b}_{i,1}^{n}\cdot\mathbf{g}_{1}^{n}=\frac{GM}{R^{2}}\times$$

$$\sum_{n=0}^{N_{\max}}\sum_{m=0}^{n}\left\{\begin{array}{l}(\frac{R}{r_2})^{n+2}\left[\begin{array}{l}b_{2,x}\cos(m\lambda_2)\overline{P}_{nm}^{'}(\cos\theta_2)\sin\theta_2-\\ mb_{2,y}\sin(m\lambda_2)\overline{P}_{nm}(\cos\theta_2)\frac{1}{\sin\theta_2}+\\ b_{2,z}(n+1)\cos(m\lambda_2)\overline{P}_{nm}(\cos\theta_2)\end{array}\right]-\\ (\frac{R}{r_1})^{n+2}\left[\begin{array}{l}b_{1,x}\cos(m\lambda_1)\overline{P}_{nm}^{'}(\cos\theta_1)\sin\theta_1-\\ mb_{1,y}\sin(m\lambda_1)\overline{P}_{nm}(\cos\theta_1)\frac{1}{\sin\theta_1}+\\ b_{1,z}(n+1)\cos(m\lambda_1)\overline{P}_{nm}(\cos\theta_1)\end{array}\right]\end{array}\right\}\Delta C_{nm}+$$

$$+\left\{\begin{array}{l}(\frac{R}{r_2})^{n+2}\left[\begin{array}{l}b_{2,x}\sin(m\lambda_2)\overline{P}_{nm}^{'}(\cos\theta_2)\sin\theta_2+\\ mb_{2,y}\cos(m\lambda_2)\overline{P}_{nm}(\cos\theta_2)\frac{1}{\sin\theta_2}+\\ b_{2,z}(n+1)\sin(m\lambda_2)\overline{P}_{nm}(\cos\theta_2)\end{array}\right]-\\ (\frac{R}{r_1})^{n+2}\left[\begin{array}{l}b_{1,x}\sin(m\lambda_1)\overline{P}_{nm}^{'}(\cos\theta_1)\sin\theta_1+\\ mb_{1,y}\cos(m\lambda_1)\overline{P}_{nm}(\cos\theta_1)\frac{1}{\sin\theta_1}+\\ b_{1,z}(n+1)\sin(m\lambda_1)\overline{P}_{nm}(\cos\theta_1)\end{array}\right]\end{array}\right\}\Delta S_{nm} \quad . \qquad \text{(B.33)}$$

If we let $g(\theta)=\overline{P}_{nm}(\cos\theta)$, then, $g^{'}(\theta)=-\overline{P}_{nm}^{'}(\cos\theta)\sin\theta$, so,

$$\mathbf{b}_{i,2}^{n}\cdot\mathbf{g}_{2}^{n}-\mathbf{b}_{i,1}^{n}\cdot\mathbf{g}_{1}^{n}=\frac{GM}{R^{2}}\times$$

$$\sum_{n=0}^{N_{\max}}\sum_{m=0}^{n}\left\{\begin{array}{l}(\frac{R}{r_2})^{n+2}\left[\begin{array}{l}-b_{2,x}\cos(m\lambda_2)g^{'}(\theta_2)-\\ mb_{2,y}\sin(m\lambda_2)g(\theta_2)\frac{1}{\sin\theta_2}+\\ b_{2,z}(n+1)\cos(m\lambda_2)g(\theta_2)\end{array}\right]-\\ (\frac{R}{r_1})^{n+2}\left[\begin{array}{l}-b_{1,x}\cos(m\lambda_1)g^{'}(\theta_1)-\\ mb_{1,y}\sin(m\lambda_1)g(\theta_1)\frac{1}{\sin\theta_1}+\\ b_{1,z}(n+1)\cos(m\lambda_1)g(\theta_1)\end{array}\right]\end{array}\right\}\Delta C_{nm}+$$

$$+\left\{\begin{array}{l}(\frac{R}{r_2})^{n+2}\left[\begin{array}{l}-b_{2,x}\sin(m\lambda_2)g^{'}(\theta_2)+\\ mb_{2,y}\cos(m\lambda_2)g(\theta_2)\frac{1}{\sin\theta_2}+\\ b_{2,z}(n+1)\sin(m\lambda_2)g(\theta_2)\end{array}\right]-\\ (\frac{R}{r_1})^{n+2}\left[\begin{array}{l}-b_{1,x}\sin(m\lambda_1)g^{'}(\theta_1)+\\ mb_{1,y}\cos(m\lambda_1)g(\theta_1)\frac{1}{\sin\theta_1}+\\ b_{1,z}(n+1)\sin(m\lambda_1)g(\theta_1)\end{array}\right]\end{array}\right\}\Delta S_{nm}\quad .\qquad \text{(B.34)}$$